USING TERRESTRIAL LASER SCANNING TO CHARACTERIZE PEATLAND MICROTOPOGRAPHY AND ASSESS TREE GROWTH RESPONSES TO ELEVATED TEMPERATURE AND CO_2

by

Jake D. Graham

A dissertation

submitted in partial fulfillment

of the requirements for the degree of

Doctor of Philosophy in Geosciences

Boise State University

August 2020

BOISE STATE UNIVERSITY GRADUATE COLLEGE

DEFENSE COMMITTEE AND FINAL READING APPROVALS

of the dissertation submitted by

Jake D. Graham

Dissertation Title: Using Terrestrial Laser Scanning to Characterize Peatland Microtopography and Assess Tree Growth Responses to Elevated Temperature and Co_2

Date of Final Oral Examination: 10 June 2020

The following individuals read and discussed the dissertation submitted by Jake D. Graham, and they evaluated their presentation and response to questions during the final oral examination. They found that the student passed the final oral examination.

Nancy F. Glenn, Ph.D.	Chair, Supervisory Committee
Marie-Anne de Graaff, Ph.D.	Member, Supervisory Committee
Paul J. Hanson, Ph.D.	Member, Supervisory Committee
Cathie Olschanowsky, Ph.D.	Member, Supervisory Committee

The final reading approval of the dissertation was granted by Nancy F. Glenn, Ph.D., Chair of the Supervisory Committee. The dissertation was approved by the Graduate College.

DEDICATION

To my loving and supportive mother and grandparents.

ACKNOWLEDGMENTS

I would like to express my utmost respect and gratitude for my advisor Dr. Nancy F. Glenn. Throughout my time in the PhD program, Nancy has exemplified what a mentor should be, by providing leadership, encouragement, compassion, and honest feedback. All of which she does with unparalleled grace. Thank you Nancy, for everything you have taught and done for me, and for having the patience to help guide me over the last four years. Your support has enabled personal and professional growth that would not have been possible without it.

I would like to thank my other committee members Dr. Marie-Anne de Graaff, Dr. Paul J. Hanson, and Dr. Cathie Olschanowsky for their time, effort, and support throughout my PhD program. I would also like to thank personnel from Oak Ridge National Lab for assisting in data collection and analyses, and for providing feedback and guidance on my research.

I would like to thank the U.S. Department of Energy, Office of Science, Office of Biological and Environmental Research and Oak Ridge National Laboratory for providing funding (#4000145196). I would also like to thank the Boise State University Department of Geosciences for providing additional funding that made this research possible.

I would like to thank the BCAL group for their friendship, support, and kindness. I would like to thank the support staff at Boise State University, and the Department of Geosciences in particular, for their time, effort, and patience that made the completion of my PhD program possible.

Finally, I thank my friends and family for their love and support.

ABSTRACT

Northern peatlands are a major terrestrial carbon (C) store, with an annual sink of 0.1 Pg C yr^{-1} and a total storage estimate of 547 Pg C. Northern peatlands are also major contributors of atmospheric methane, a potent greenhouse gas. The microtopography of peatlands helps modulate peatland carbon fluxes; however, there is a lack of quantitative characterizations of microtopography in the literature. The lack of formalized schemes to characterize microtopography makes comparisons between studies difficult. Further, many land surface models do not accurately simulate peatland C emissions, in part because they do not adequately represent peatland microtopography and hydrology. The C balance of peatlands is determined by differences in C influxes and effluxes, with the largest being net primary production and heterotrophic respiration, respectively. Tree net primary production at a treed bog in northern Minnesota represented about 13% of C inputs to the peatland, and marks tree aboveground net primary production (ANPP) as an important pathway for C to enter peatlands. Tree species *Picea mariana* (Black spruce) and *Larix Laricina* (Tamarack) are typically found in wooded peatlands in North America, and are widely distributed in the North American boreal zone. Therefore, understanding how these species will respond to environmental change is needed to make predictions of peatland C budgets in the future. As the climate warms, peatlands are expected to increase C release to the atmosphere, resulting in a positive feedback loop. Further, climate warming is expected to occur faster in northern latitudes compared to the

rest of the globe. The Spruce and Peatland Responses Under Changing Environments (SPRUCE; https://mnspruce.ornl.gov/) manipulates temperature and CO_2 concentrations to evaluate the *in-situ* response of a peatland to environmental change and is located in Minnesota, USA. In this dissertation, I documented surface roughness metrics for peatland microtopography in SPRUCE plots and developed three explicit methods for classifying frequently used microtopographic classes (microforms) for different scientific applications. Subsequently I used one of these characterizations to perform a sensitivity analysis and improve the parameterization of microtopography in a land surface model that was calibrated at the SPRUCE site. The modeled outputs of C from the analyses ranged from 0.8-34.8% when microtopographical parameters were allowed to vary within observed ranges. Further, C related outputs when using our data-driven parameterization differed from outputs when using the default parameterization by -7.9 - 12.2%. Finally, I utilized TLS point clouds to assess the effect elevated temperature and CO_2 concentrations had on *P. mariana* and *L. laricina* after the first four years of SPRUCE treatments. I observed that *P. mariana* growth (aboveground net primary production) had a negative response to temperature initially, but the relationship became less pronounced through time. Conversely, *L. laricina* had no growth response to temperature initially, but developed a positive relationship through time. The divergent growth responses of *P. mariana* and *L. laricina* resulted in no detectable change in aboveground net primary production at the community level. Results from this dissertation help improve how peatland microtopography is represented, and improves understanding of how peatland tree growth will respond to environmental change in the future.

TABLE OF CONTENTS

LIST OF TABLES

Chapter 2:

Chapter 3:

Chapter 4:

LIST OF FIGURES

Chapter 2:

Chapter 4:

CHAPTER ONE: INTRODUCTION

Peatlands are wetland ecosystems that are characterized by large quantities of accumulated organic material called peat which are the remains of plants and animals that have not fully decomposed. Peatlands can broadly be defined as peat-covered terrain, but many definitions incur a minimum peat depth (e.g., 0.3-0.4m) to be classified as a peatland (National Wetlands Working Group, 1997; Joosten and Clarke, 2002; Rydin and Jeglum, 2013). The highest concentration of peatlands is in the northern latitudes covering 4 million km^2, with tropical (368,500 km^2) and southern peatlands (45,000 km^2) being less common (Yu et al., 2010). Peatlands take on various forms depending on their morphology and hydrology. Two main types of peatlands are bogs and fens, which differ depending on whether they receive the majority of water and nutrients from precipitation (ombrotrophic bogs) or whether they receive water and nutrients from surface and/or groundwater (minerotrophic fen).

Incomplete decomposition of peat is a result of saturated or partially saturated soils driven by water tables near the peat surface that lead to anoxic conditions and reduce the rate of decomposition. Additionally, many plants frequently found in peatlands have tissue that is resistant to decomposition. *Sphagnum* mosses are one such plant, and are an essential component of the plant community in most peatlands. *Sphagnum* mosses are able to tolerate the moist, cool, and low nutrient conditions common in peatlands. *Sphagnum* is not only able to thrive in acidic conditions characteristic of peatlands, they also contain chemical compounds that make them

resistant to decay and promote acidic, wet, and anoxic conditions (Rydin and Jeglum, 2013). Due to the unique role *Sphagnum* plays in peatland development and their ability to maintain conditions which facilitate peat production, *Sphagnum* are often described as 'builders', 'engineers', and 'a keystone' of peatland ecosystems (Rydin and Jeglum, 2013; Rochefort, 2000; Norby et al., 2019). *Sphagnum* is also a major contributor of peat, accounting for about half of carbon (C) inputs into peatlands (Szumigalski and Bayley, 1996; Rydin and Jeglum, 2013; Griffiths et al., 2017; Hanson et al. 2020).

Like all bryophytes, *Sphagnum* mosses are non-vascular and must grow in wet or moist conditions. As a result, *Sphagnum* photosynthesis is related to water content (Rydin, 1985), and *Sphagnum* water content is related to peatland water table depth (Schipperges and Rydin, 1998). Tuitilla et al. (2004) performed a 4-year field study in which they measured *Sphagnum* gross primary production (GPP) in relation to water table depth and found that GPP increased by over 100% when the water table position moved up from -0.3m to -0.2m, and that the optimum water table depth for *Sphagnum* GPP was -0.12m. Small variations in elevation of the peatland surface modulate the depth to the water table, and therefore modulate *Sphagnum* GPP. This spatial variation in the elevation of the peatland surface is termed microtopography.

In addition to *Sphagnum* GPP, peatland microtopography plays a major role in many other biogeochemical processes, and is a key driver of: decomposition rates (Johnson and Damman, 1991), plant species distributions (Andrus et al., 1983), plant productivity (Moore, 1989), and nutrient availability (Damman, 1978; Chapin et al., 1979). The microtopography of peatlands is typically an undulating surface with depression-like areas that are at or near the water table and mound-like areas (~10's of

cm tall) that have a greater depth to the water table. These depression and mound-like areas are often generalized into topographic classes referred to as microforms, where the depression-like areas are hollows and the mound-like areas are hummocks. Due to their morphological differences, hummocks and hollows exhibit differences in carbon flux, with hummocks typically exhibiting higher carbon dioxide (CO_2) flux, while hollows comparatively exhibit higher methane (CH_4) emissions (Kim and Verma, 1993; Bubier et al., 1993; Waddington and Roulet, 1996). Higher CO_2 emissions in hummocks are largely a result of hummocks having higher temperatures and more aerobic conditions than hollows (Bubier et al., 1993). Water table position is highly correlated with CH_4 flux (Bubier et al., 1993) and higher methane (CH_4) emission in hollows is a product of higher moisture content (often inundation), which leads to anaerobic decomposition of organic material (Moore and Knowles, 1989; Bubier et al., 1993).

Understanding the influence of environmental change on C storage in peatlands is necessary to make informed predictions and simulations of the future dynamics of the global C cycle. Due to slow decomposition in peatlands, the rate at which (C) enters peatlands through GPP is faster than the rate C leaves the system, primarily through respiration. This imbalance of incoming and outgoing C fluxes in peatlands causes peat (and C) to accumulate in peatlands, and is the reason peatlands are C sinks and represent a large C pool. Peatlands accumulate peat at typical rates of 20-30 g C m^{-2} yr^{-1} (Yu et al., 2010), which translates to a total annual sink of 0.1 Pg C yr^{-1} for northern peatlands (Waddington and Roulet, 1996). This slow accumulation of C has been occurring for the last ~ 7,000-14,000 years (Yu, 2011; Morris et al., 2018) resulting in estimates of total northern peatland C storage of 547 (473 - 621) Pg C (Yu et al., 2010). The immense

amount of C currently stored in peatlands and their capability to continue to store C demonstrates their importance to the global C cycle. Additionally, anaerobic conditions in northern peatlands result in major emissions of CH_4 to the atmosphere (Bubier et al., 1993). This is important in the context of environmental change, as CH_4 is the second most important greenhouse gas, and has a global warming potential 25-28 times stronger than CO_2 at the 100-year time horizon (Boucher et al., 2009). It is estimated that 30 - 35 Tg CH_4 yr^{-1} are emitted from northern peatlands (Post et al., 1982; Gorham, 1991).

While peatlands have been C sinks previously, the fate of the large quantities of C stored in peatlands is unclear as the climate warms. Recent warming studies have demonstrated that peatlands could switch from C sinks to C sources with warming (Hanson et al., 2020), and that warming resulted in a significant increase in CH_4 emissions (Wilson et al., 2016; Hopple et al., 2020). The influence of climate warming on northern peatlands is exacerbated by warming occurring faster in northern latitudes (3-8 °C by 2100; Northeast Climate Impacts Assessment, 2006), which is the region of the globe with the highest density of peatlands.

The Spruce and Peatland Under Changing Environments (SPRUCE; https://mnspruce.ornl.gov/) experiment measures how a northern peatland responds to environmental change via *in-situ* treatments of whole-ecosystem-warming and elevated CO_2 concentrations. The SPRUCE experimental site is located in the Marcell Experimental Forest in Northern Minnesota, USA, within the S1 bog (47◦30.476 N; 93◦27.162 W; 418 m above mean sea level), which is an 8.1 ha acidic (pore water pH ≈ 3-4) ombrotrophic peat bog with average peat depths of 2.27m and the basal age of the deepest centimeter of peat ranging from 5,100 - 11,100 cal BP (Sebestyen et al., 2011;

Slater et al., 2012; Griffiths and Sebestyen, 2016; McFarlane et al., 2018). The study comprises 10 open-top octagonal enclosed plots (height = 7m; diameter = 12.8m; area = 114.8 m^2). The temperature treatments include deep-peat heating that uses heating elements extending ~3m into the peat (Hanson et al., 2017) combined with air warming achieved by blowing heated air 1m above the peat surface to achieve heating throughout the enclosed air space (Hanson et al., 2017). The target differential temperature treatments at SPRUCE are +0, +2.25, +4.5, +6.75, and +9 °C with two plots at each temperature treatment. One plot for each temperature treatment receives elevated CO_2 (eCO_2) by injecting pure CO_2 to a target concentration of +500 ppm above ambient (Hanson et al., 2017).

The SPRUCE experiment uses a model-experimental coupling (MODEX) framework to incorporate understanding gained from experimental data into computational models. One such model is the land surface component (ELM) of the Energy Exascale Earth System Model (E3SM). A modified version of ELM, named ELM_SPRUCE, was developed and calibrated at the SPRUCE site to improve the ELM representation of peatlands. Most land surface models lack the representation of vegetated wetlands and peatlands, which is a major source of uncertainty for global estimates of terrestrial C (Tian et al., 2015). ELM_SPRUCE addressed this deficiency by representing the microtopography and hydrology of a perched peat bog, which resulted in a major improvement in the simulation of water table position (Shi et al., 2015). Further, Shi et al. (*in review*) developed a plant functional type (PFT) to represent the non-vascular *Sphagnum* moss in ELM_SPRUCE. These modifications mark major advances towards more accurate simulations of peatland C dynamics in land surface models.

Initial data from the SPRUCE experiment suggests that the S1 bog is a C sink, but with the SPRUCE warming treatments the system switches to a C source (Hanson et al., 2020). Hanson et al. (2020) quantified the pretreatment C budget at the SPRUCE site based on a recalculation of the estimate in Griffiths et al. (2017) and found that the net ecosystem exchange (NEE) was 81(±101) gC m^{-2} $year^{-1}$. One of the fluxes that marks C entry into the system is tree aboveground net primary production (ANPP), which was estimated for *Larix laricina* (Du Roi) K. Koch (American larch) and *Picea mariana* (Mill.) B.S.P. (black spruce) by Hanson et al., (2020) at 51 (± 37) gC m^{-2} $year^{-1}$. In addition to being an important component of the peatland C budget, these species are widely distributed across the boreal zone of North America, with their biomass constituting a large pool of C and their ANPP representing an important pathway that C enters boreal ecosystems in North America. Therefore, understanding how these tree species will respond to environmental change simulated by SPRUCE treatments is needed to make informed predictions of future peatland C budgets, and can provide insights into how these species will respond to environmental change throughout their geographic range.

When terrestrial laser scanning (TLS) is used to scan trees, point clouds provide detailed digital representations of the tree canopy from which tree height and canopy volume can be calculated. Data collected through TLS utilizes light detection and ranging (lidar) to measure the flight time of laser pulses emitted from the scanner. TLS uses the laser pulse flight time, the speed of light, and the refractive index of the atmosphere to measure the distance from the scanner to the object which reflected the pulse with extreme accuracy (generally > 1cm). The vector along which the laser pulse traveled is

also recorded. The combination of the distance and this vector enable the precise location of the object which reflected the laser pulse to be calculated. Most laser scanners are capable of emitting hundreds of thousands of laser pulses per second, and thus build extremely dense datasets called point clouds. Point clouds are 3D representations of objects in the scanned location storing cartesian coordinates (e.g., x, y, z or latitude longitude and elevation) in addition to other attributes like the quantity of light returning to the scanner (intensity).

The TLS point clouds have great potential to address the lack of quantitative methods for characterizing peatland microtopography. Methods that provide robust datasets for characterization of peatland microtopography are lacking, primarily because traditional approaches have a major tradeoff between sampling density and sampled area. Previous studies have largely measured peatland microtopography with transects (Almendiger et al., 1986; Ehrenfeld 1995; Pouliot et al., 2011), which are time and labor intensive and have sampling intervals as high as 1.0 m (Pouliot et al., 2011). Laser scanners have also been used to measure microtopography outside of peatlands (Huang et al., 1988; Huang and Bradford, 1990; Darboux and Huang, 2003). Scanners that use lasers and cameras to triangulate surfaces are limited by the distance they can sample, which is typically much lower than time-of-flight laser scanners (Boehler et al., 2002). Studies using triangulating laser scanners have only sampled a few meters from the sensor (e.g., Flanagan et al., 1995; Darboux and Huang, 2003). As a result, literature descriptions and definitions of hummocks and hollows are qualitative (e.g., Bubier et al., 1993; Nungesser, 2003; Benscoter et al., 2005), likely resulting in discrepancies in how each microform is classified between studies. Such discrepancies have major implications

when measurements are taken in each microform (e.g., Damman, 1978; Johnson and Damman, 1991; Kim and Verma, 1993) and scaled to larger extents using the proportional areal coverage of each microform (e.g., Kim and Verma, 1993). Proportional areal coverage of microforms is also a parameter used in computational models simulating peatland C dynamics like ELM_SPRUCE and the Peatland Carbon Simulator (PCARS) (Frolking et al., 2002), which further demonstrates the need for methods that explicitly classify and characterize peatland microforms.

The limited horizontal diameter of the SPRUCE experimental plots (~12 m wall to wall) makes the use of traditional tree height observations using clinometers or height poles difficult, because of the limited sight lines and a reduced range of acute angles to be interpreted, as well as uncertainty in location of the soil surface. This can make measuring tree growth response to SPRUCE treatments difficult. TLS provides a viable remote sensing alternative for traditional tree height measurements that does not suffer from the same limitations. Additionally, previous studies have demonstrated the ability of TLS data to predict both aboveground biomass (AGB) and leaf area index (LAI) (Greaves et al., 2015; Li et al., 2015; Olsoy et al., 2014a; Olsoy et al., 2014b), making TLS a method well suited for measuring tree growth responses at the SPRUCE experiment.

Thesis Organization

TLS point clouds act as the nexus of this dissertation. TLS is used to establish digital elevation models (DEM) for the characterization of microtopography, and the measurement of tree growth responses to SPRUCE treatments. Subsequent chapters of this dissertation provide data and its interpretation suited to answer the following

questions: 1) How can I best utilize TLS point clouds to improve how peatland microtopography is quantified and how microforms are classified? 2) How does microtopography influence C cycling in ELM_SPRUCE, and which microtopographical parameter is the C cycle most sensitive to? and 3) How will *Picea mariana* and *Larix laricina* growth respond to warmer temperatures and higher concentrations of atmospheric CO_2 in the future?

Following this introduction, the second chapter of this dissertation creates DEMs of the bog surface within SPRUCE plots, which are subsequently used to characterize peatland microtopography using geostatistics and metrics of surface roughness (Graham et al., 2020). Further, DEMs are used to develop three methods to classify hummock and hollow microforms, with each method targeted at a different scientific application. In chapter three, I utilize one of these classifications to calculate microtopographical parameters for ELM_SPRUCE, and compare the observed parameter values to the 'default' parameter values that were determined heuristically. I also compared quantities of interest (QOI) related to the C cycle output by ELM_SPRUCE when using the 'default' parameterization and the observed mean parameter values. Further, I perform an ensemble of 3,000 ELM_SPRUCE simulations in which parameters were allowed to randomly vary to perform a sensitivity analysis and evaluate the effect of each parameter on C pools and fluxes. The fourth chapter of this dissertation utilizes a combination of traditional measures of basal area and TLS measurements of tree height and canopy volume to evaluate the effect elevated temperature and CO_2 concentrations have on tree growth after the first four years of SPRUCE treatments. Finally, chapter five summarizes

findings in chapters 2-4 and discusses how these results can be used to improve understanding of peatland C dynamics, and future work building off this dissertation.

References

Almendinger, J. C., J. E. Almendinger, P. H. Glaser. 1986. Topographic fluctuations across a spring fen and raised bog in the Lost River peatland, Northern Minnesota. Journal of Ecology 74:393-401.

Andrus, R., D. J. Wagner, and J. E. Titus. 1983. Vertical distribution of *Sphagnum* mosses along hummock-hollow gradients. Canadian Journal of Botany 61:3128-3139.

Benscoter, B. W., K. R. Wieder, and D. H. Vitt. 2005. Linking microtopography with post-fire succession in bogs. Journal of Vegetation Science 16:453-460.

Boehler, W., G. Heinz, and A. Marbs. 2002. The potential of non-contact close range laser scanners for cultural heritage recording. International archives of the photogrammetry, remote sensing and spatial information sciences 43:430-438.

Boucher, O., P. Friedlingstein, B. Collins, and K. P. Shine. 2009. The indirect global warming potential and global temperature change potential due to methane oxidation. Environmental Research Letters 4:044007.

Bubier, J., A. Cotello, T. R. Moore, N. T. Roulet, and K. Savage. 1993. Microtopography and methane flux in boreal peatlands, northern Ontario Canada. Canadian Journal of Botany 71:1056-1063.

Chapin, F. S., K. Van Cleve, and M. C. Chapin. 1979. Soil temperature and nutrient cycling in the tussock growth form of *Eriophorum vaginatum*. Journal of Ecology 76:169-189.

Damman, A. W. H. 1978. Distribution and movement of elements in ombrotrophic peat bogs. Oikos 30:480-495

Darboux, F., and C. Huang. 2003. An instantaneous-profile laser scanner to measure soil surface microtopography. Soil Science Society of America Journal 67:92-99.

Ehrenfeld, J. G. 1995. Microtopography and vegetation in Atlantic white cedar swamps: the effects of natural disturbances. Canadian Journal of Botany 73:474–484.

Flanagan, D. C., C. Huang, L. D. Norton, and S. C. Parker. 1995. Laser scanner for erosion plot measurements. Transactions of the American Society of Agricultural and Biological Engineers 38:703-710.

Frolking, S., N. T. Roulet, T. R. Moore, P. M. Lafleur, J. L. Bubier, and P. M. Crill. 2002. Modeling seasonal to annual carbon balance of Mer Bleue Bog, Ontario, Canada. Global Biogeochemical Cycles 16:1–21, doi:10.1029/2001GB001457

Gorham, E. 1991. Northern Peatlands: Role in the carbon cycle and probable responses to climatic warming. Ecological Applications 1:182-195.

Graham, J. D., N. F. Glenn, L. P. Spaete, and P. J. Hanson. 2020. Characterizing Peatland Microtopography Using Gradient and Microform-Based Approaches. Ecosystems, 1-17.

Greaves, H. E., L. A. Vierling, J. U. H. Eitel, N. T. Boelman, T. S. Magney, C. M. Prager, and K. L. Griffin. 2015. Estimating aboveground biomass and leaf area of low-stature Arctic shrubs with terrestrial LiDAR. Remote Sensing of Environment 164:26-35.

Griffiths, N. A., P. J. Hanson, D. M. Ricciuto, C. M. Iverson, A. M. Jensen, A. Malhotra, K. J. McFarlane, R. J. Norby, K. Sargsyan, S. D. Sebestyen, X. Shi, A. P. Walker, E. J. Ward, J. M. Warren, and D. J. Weston. 2017. Temporal and spatial variation in peatland carbon cycling and implications for interpreting response of an ecosystem-scale warming experiment. Soil Science Society of America Journal 81:1668-1688.

Griffiths, N. A., and S. D. Sebestyen. 2016. Dynamic vertical profiles of peat porewater chemistry in a Northern peatland. Wetlands 36:1119-1130.

Hanson, P. J., N. A. Griffiths, C. M. Iversen, R. J. Norby, S. D. Sebestyen, J. R. Phillips, J. P. Chanton, R. K. Kolka, A. Malhotra, K. C. Oleheiser, J. M. Warren, X. Shi, X. Yang, J. Mao, D. M. Ricciuto. 2020. Rapid net carbon loss from a whole-ecosystem warmed peatland. AGU Advances, doi: 10.1029/2020AV000163

Hanson, P. J., J. S. Riggs, W. R. Nettles, J. R. Phillips, M. B. Krassovski, L. A. Hook, L. Gu, A. D. Richardson, D. M. Aubrecht, D. M. Ricciuto, J. M. Warren, and C.

Barbier. 2017. Attaining whole-ecosystem warming using air and deep soil heating methods with an elevated CO_2 atmosphere. Biogeosciences 14:861–883, doi: 10.5194/bg-14-861-2017

Hopple, A. M., R. M. Wilson, M. Kolton, C. A. Zalman, J. P. Chanton, J. Kostka, P. J. Hanson, J. K. Keller, and S. D. Bridgham. 2020. Massive peatland carbon banks vulnerable to rising temperatures. Nature Communication 11:2373 doi: 10.1038/s41467-020-16311-8

Huang, C., and J. M. Bradford. 1990. Portable laser scanner for measuring soil surface roughness. Soil Science Society of America Journal 54:1402-1406.

Huang, C., I. White, E. Thwaite, and A. Bendeli. 1988. A noncontact laser system for measuring soil surface topography. Soil Science Society of America Journal 52:350-355.

Johnson, L. C., and A. W. H. Damman. 1991. Species-controlled *Sphagnum* decay on a Swedish raised bog. Oikos 61:234-242.

Joosten, H. and D. Clarke. 2002. Wise use of mires and peatlands. International Mire Conservation Group and International Peat Society 304 pp.

Kim, J., and S. B. Verma. 1992. Soil Surface CO_2 flux in a Minnesota peatland. Biogeochemistry 18:32-51.

Li, A., N. F. Glenn, P. J. Olsoy, J. J. Mitchell, and R. Shrestha. 2015. Aboveground biomass estimates of sagebrush using terrestrial and airborne LiDAR data in a dryland ecosystem. Agricultural and Forest Meteorology 213:138-147.

McFarlane, K. J., P. J. Hanson, C. M. Iversen, J. R. Phillips, and D. J. Brice. 2018. Local spatial heterogeneity of Holocene carbon accumulation throughout the peat profile of an ombrotrophic Northern Minnesota bog. Radiocarbon 60:941-962.

Moore, T. R. 1989. Growth and net production of *Sphagnum* at five fen sites, subarctic eastern Canada. Canadian Journal of Botany 67:1203-1207.

Moore, T. R., and R. Knowles. 1989. The influence of water table levels on methane and carbon dioxide emissions from peatland soils. Canadian Journal of Soil Science 69:33-38.

Morris, P. J., G. T. Swindles, P. J. Valdes, R. F. Ivanovic, L. J. Gregoire, M. W. Smith, L. Tarasov, A. M. Haywood, and K. L. Bacon. 2018. Global peatland initiation driven by regionally asynchronous warming. PNAS 115:4851-4856.

National Wetlands Working Group. 1997. The Canadian wetland classification system, 2nd edn., University of Waterloo, Canada.

Norby, R. J., J. Childs, P. J. Hanson, and J. M. Warren. 2019. Rapid loss of an ecosystem engineer: Sphagnum decline in an experimentally warmed bog. Ecology and Evolution 9:12571-12585.

Northeast Climate Impact Assessment (NECIA), 2006: Climate Change in the U.S. Northeast: A Report of the Northeast Climate Impacts Assessment. Union of Concerned Scientists, Cambridge, MA, 35 pp.

Nungesser, M. K. 2003. Modelling microtopography in boreal peatlands: hummocks and hollows. Ecological modelling 165:175-207.

Olsoy, P. J., N. F. Glenn, and P. E. Clark. 2014a. Estimating sagebrush biomass using terrestrial laser scanning. Rangeland Ecology and Management 67:224-228.

Olsoy, P. J., N. F. Glenn, P. E. Clark, and D. R. Derryberry. 2014b. Aboveground total and green biomass of dryland shrub derived from terrestrial laser scanning. ISPRS Journal of Photogrammetry and Remote Sensing 88:166-173.

Post, R. M., W. R. Emanuel, P. J. Zinke, and A. G. Stangenberger. 1982. Soil carbon pools and world life zones. Nature 298:156-159.

Pouliot, R., L. Rochefort, and E. Karofeld. 2011. Initiation of microtopography in revegetated cutover peatlands. Applied Vegetation Science 14:158-171.

Rochefort, L. 2000. Sphagnum: a keystone genus in habitat restoration. The Bryologist 103:503-508.

Rydin, H. 1985. Effect of water level on desiccation of Sphagnum in relation to surrounding Sphagna. Oikos 45:374-379.

Rydin, H., and J. K. Jeglum. 2013. The Biology of Peatlands, the Biology of Habitats Series, 2nd edn., Oxford Univ. Press, Oxford.

Schipperges, B., and H. Rydin. 1998. Response of photosynthesis of Sphagnum species from contrasting microhabitats to tissue water content and repeated desiccation. New Phytologist 140:677-684.

Sebestyen, S. D., C. Dorrance, D. M. Olson, E. S. Verry, R. K. Kolka, A. E. Elling, and R. Kyllander. 2011. Longterm monitoring sites and trends at the Marcell Experimental Forest. In: R. K. Kolka, S. D. Sebestyen, E. S. Verry, and K. N. Brooks, editors. Peatland Biogeochemistry and Watershed Hydrology at the Marcell Experimental Forest. Boca Raton Florida: CRC Press, p15-72.

Shi, X., D. M. Ricciuto, P. E. Thornton, X. Xu, F. Yuan, R. J. Norby, A. P. Walker, J. Warren, J. Mao, P. J. Hanson, L. Meng, D. Weston, and N. A. Griffiths. *In Review*. Modeling the hydrology and physiology of *Sphagnum* moss in a northern temperate bog.

Shi, X., P. E. Thornton, D. M. Ricciuto, P. J. Hanson, J. Mao, S. D. Sebestyen, N. A. Griffiths, G. Bisht. 2015. Representing northern peatland microtopography and hydrology within the Community Land Model. Biogeosciences 12:6463–6477.

Slater, L., P. J. Hanson, and L. A. Hook. 2012. SPRUCE S1 Bog Peat Depth Determined by Push Probe and GPR: 2009-2010. Oak Ridge National Laboratory, TES SFA, U.S. Department of Energy, Oak Ridge, Tennessee, U.S.A.https://doi.org/10.3334/CDIAC/spruce.002

Szumigalski, A. R., and S. E. Bayley. 1996. Net above-ground net primary production along a bog-rich fen gradient in central Alberta, Canada. Wetlands 16:467-476.

Tian, H., C. Lu, J. Yang, K. Banger, D. N. Huntzinger, C. R. Schwalm, A. M. Michalak, R. Cook, P. Ciais, D. Hayes, M. Huang, A. Ito, A. K. Jain, H. Lei, J. Mao, S. Pan, W. M. Post, S. Peng, B. Poulter, W. Ren, D. Ricciuto, K. Schaefer, X. Shi, B. Tao, W. Wang, Y. Wei, Q. Yang. B. Zhang, and N. Zeng. 2015. Global patterns

and controls of soil organic carbon dynamics as simulated by multiple terrestrial biosphere models: Current status and future directions. Global Biogeochemical Cycles 29:775-792. doi:10.1002/2014GB005021.

Tuittila, E. S., H. Vasander, and J. Laine. 2004. Sensitivity of C sequestration in reintroduced *Sphagnum* to water-level variation in a cutaway peatland. Restoration Ecology 12:483-493.

Waddington, J. M., and N. T. Roulet. 1996. Atmosphere-wetland carbon exchanges: Scale dependency of CO_2 and CH_4 exchange on the developmental topography of a peatland. Global Biogeochemical Cycles 10:233-245.

Wilson, R. M., et al. 2016. Stability of Peatland Carbon to Rising Temperatures. Nature Communications 7:13723.

Yu, Z. 2011. Holocene carbon flux histories of the world's peatlands: global carbon-cycle implications. The Holocene 21:761-774.

Yu, Z. 2012. Northern peatland carbon stocks and dynamics: a review. Biogeosciences 9:4071-4085.

Yu, Z, D. W. Beilman, S. Frolking, G. M. MacDonald, N. T. Roulet, P. Camill, D. J. Charman. 2011. Peatlands and their role in the global carbon cycle. EOS 92:97-108.

Yu, Z.C., J. Loisel, D. P. Brosseau, D. W. Beilman, and S. J. Hunt. 2010. Global peatland dynamics since the Last Glacial Maximum. Geophysical Research Letters 37.

CHAPTER TWO: CHARACTERIZING PEATLAND MICROTOPOGRAPHY USING GRADIENT AND MICROFORM-BASED APPROACHES

This chapter has been published as:

Graham, J. D., N. F. Glenn, L. P. Spaete, and P. J. Hanson. 2020. Characterizing peatland microtopography using gradient and microform-based approaches. Ecosystems pp. 1-17.

Abstract

Peatlands represent an important component of the global carbon cycle, storing 180-621 Gt of carbon (C). Small scale spatial variations in elevation, frequently referred to as microtopography, influence ecological processes associated with the peatland C cycle, including *Sphagnum* photosynthesis and methane flux. Microtopography can be characterized with measures of topographic variability and by using conceptual classes (microforms) linked to function: most commonly hummocks and hollows. However, the criteria used to define these conceptual classes are often poorly described, if at all, and vary between studies. Such inconsistencies compel development of explicit quantitative methods to classify microforms. Furthermore, gradient-based characterizations that describe spatial variability without the use of microforms are lacking in the literature. Therefore, the objectives of this study were to 1) calculate peatland microtopographical elevation gradients and measures of spatial variability, 2) develop three microform classification methods intended for specific purposes, and 3) evaluate and contrast classification methods. Our results suggest that at spatial scales much larger than

microforms, elevation distributions are unimodal, and are well approximated with parametric probability density functions. Results from classifications were variable between methods and years, and exhibited significant differences in mean hollow areal coverages of a raised ombrotrophic bog. Our results suggest that the conceptualization and classification of microforms can significantly influence microtopographic structural metrics. The three explicit methods for microform classification described here may be used and built upon for future applications.

Introduction

Northern peatlands are an important component of the global carbon (C) cycle (Yu et al., 2010; Yu et al., 2011), typically storing C at rates in the range of 20-30 g C m^{-2} yr^{-1} (Yu et al., 2011). Northern peatlands have been storing C for ~ 7,000 - 14,000 years (Yu, 2011; Morris et al., 2018), resulting in total storage estimates ranging from 180-621 Gt C (Gorham, 1990; Yu et al., 2010; Yu, 2012). The most recent estimate of 547 (473-621) Gt C from Yu et al. (2010) represents over one-third of global terrestrial C, when using soil organic carbon estimates of ~1,400 Gt C (Cao and Woodward, 1998; Scharlemann et al., 2014). Northern peatlands are also major contributors of atmospheric methane (CH_4) (Fung et al., 1991). Methane emissions from Northern peatlands to the atmosphere (30 - 35 Tg CH_4 yr^{-1}; Post et al., 1982; Fung et al., 1991; Gorham, 1991) represent a significant source of atmospheric CH_4, with these emissions estimated to account for up to ~7% of global CH_4 emissions (Fung et al., 1991).

The hummock-hollow complex dominates the microtopography of many peatlands and plays a major role in several ecological, hydrologic, and biogeochemical processes including C dynamics. Specifically, these include: an influence on greenhouse

gas emissions (Bubier et al., 2003; Hirano et al., 2009; Moore et al., 2011), rates of decomposition (Johnson and Damman, 1991), peat accumulation (Chaudhary et al., 2018), plant community (Andrus et al., 1983; Chaudhary et al., 2018; Harris and Baird, 2018; Arsenault et al., 2019; Malhotra et al., 2016), plant productivity (Moore, 1989), water chemistry (Arsenault et al., 2019), and nutrient availability (Chapin et al., 1979; Damman, 1978). The primary biophysical driver of these differences is changes in peat water and oxygen content, which are associated with water table depth.

Water table depth is closely linked to multiple ecological processes associated with microtopography and biogeochemical cycling. The position of the water table controls where aerobic or anaerobic decomposition occurs in the peat column, which in turn influences carbon dioxide (CO_2) and CH_4 emissions (Moore and Dalva, 1993). Anaerobic conditions beneath the water table drive CH_4 flux (Moore and Knowles, 1989; Bubier et al., 1993; Freeman et al., 1993; Moore and Dalva, 1993; Hirano et al., 2009; Moore et al., 2011; Munir and Strack, 2014), and the water table has been described as an 'on-off switch' for CH_4 emissions by Christensen et al. (2003). Furthermore, water content in non-vascular *Sphagnum* is linked to water table proximity (Rydin 1985), which modulates photosynthetic rates (Schipperges and Rydin, 1998). Walker et al. (2017) found water table depth to be a strong predictor of *Sphagnum* gross primary production (GPP) variability at the SPRUCE site (see below), due to the influence of water table depth on the vertical soil moisture gradient.

The predominantly saturated conditions in hollows promote anaerobic decomposition of organic material, which drives higher CH_4 emissions compared to hummocks (Moore and Knowles, 1989; Bubier et al., 1993). In contrast, hummocks

exhibit higher CO_2 fluxes than hollows because they occupy a larger fraction of the peat column in aerobic conditions, and can experience warmer temperatures seasonally, influencing rates of CO_2 emission (Moore and Knowles, 1989; Bubier et al., 1993). While the ratio of emitted CO_2:CH_4 differs between microforms, CO_2 flux is higher than CH_4 flux in both microforms (Kim and Verma, 1992; Bubier et al., 1993; Waddington and Roulet, 1996).

Methods that provide robust datasets for characterizing peatland microtopography and classifying microforms were lacking until recently, resulting in descriptions ranging from qualitative (e.g., Bubier et al., 1993; Nungesser, 2003; Benscoter et al., 2005) to quasi-quantitative (e.g., Johnson et al., 1990; Weltzin et al., 2001; Pouliot et al., 2011). Examples of qualitative descriptors for hollows include elevation (low areas), slope (flat areas), and concavity (depressions). Ambiguous descriptions can confound classifications of microforms between studies. Moreover, explicit quantitative definitions provide clarity and allow for improved scaling and syntheses between studies.

One reason for the lack of detailed quantitative characterizations of peatland microtopography was the previous inability to provide dense and highly accurate elevation data to measure microtopography over large areas (e.g., Almendiger et al., 1986; Huang et al., 1988; Huang and Bradford, 1990; Ehrenfeld, 1995; Flanagan et al., 1995; Darboux and Huang, 2003; Pouliot et al., 2011). Recently, however, remote sensing technologies including unmanned aerial systems (UAS) based structure from motion (SfM) (Lucieer et al., 2014; Mercer and Westbrook, 2016; Smith et al., 2016; Nouwakpo et al., 2014; Smith and Warburton, 2018; Moore et al., 2019) and terrestrial laser scanning (TLS) (Barneveld et al., 2013; Brubaker et al., 2013; Nouwakpo et al.,

2016) have been used to measure microtopography. Terrestrial laser scanning is a remote sensing technology that provides accurate and dense point clouds, providing a promising technique for characterizing peatland microtopography at fine scales over relatively large areas (e.g., 0.01 – 0.10 m resolution over 10s – 100s of meters). Stovall et al. (2019) used TLS to generate high-resolution digital elevation models (DEM) of wetland microtopography with high accuracy (root mean squared error; RMSE = 0.04 cm), and used a topographic segmentation algorithm to define hummock microforms. Additionally, Moore et al. (2019) used SfM to derive digital models of peatland microtopography and used Gaussian mixed models to characterize elevation distributions of microtopography.

Considering the influence of microtopography on hydrologic and biogeochemical processes, proper representation of microtopography in land surface models is needed for accurate simulations of biogeochemical cycles (see Moore et al., 2019). Most land surface models do not accurately characterize C emissions from peatlands, partially because they don't represent peatland microtopography or hydrology. However, several models have been made, or modified, to incorporate peatland microtopography (Frolking et al., 2002; Baird et al., 2011; Morris et al., 2011; Shi et al., 2015). Some models utilize simplistic approaches that represent discrete hummock and hollow microforms (Frolking et al., 2002; Shi et al., 2015), while DigiBog (Baird et al., 2011) provides a more sophisticated approach that is able to incorporate elevation gradients representative of peatland microtopography.

The incorporation of microtopography in both field and modeling studies that investigate the hydrology, ecology, and biogeochemistry of peatlands compels the need

for accurate characterization of microtopography. Characterization of microtopography should include methods that retain high structural fidelity and resolution, in addition to quantitative microform classifications intended for implementation into applications using the hummock-hollow dichotomy. Therefore, the objectives of this study were to (1) calculate and analyze measures of microtopography with high structural fidelity (i.e., elevation distributions, surface roughness, and spatial variation), (2) develop and assess three application-specific microform classification methodologies, and (3) compare classification results using the three methods and discuss their utility for both modeling and field studies. To accomplish these objectives, I utilized TLS measured point clouds to derive high-resolution DEMs of the bog. I then calculated measures of surface roughness and model semivariograms, and finally performed quantitative microform classifications on the generated DEM to produce spatially explicit maps of microforms for comparison.

Methods

Study site

The Spruce and Peatland Response Under Changing Environments project (SPRUCE; Hanson et al., 2017b) experiment is located at the S1 bog in the Marcell Experimental Forest, Northern Minnesota, USA. The S1 bog is an 8.1 ha ombrotrophic peat bog with a perched water table and little regional groundwater influence (Sebestyen et al., 2011). Mean annual air temperature at S1 was 3.4° C and mean annual precipitation was 780 mm between 1969 and 2009 (Sebestyen et al., 2011). S1 is acidic (near surface pore water pH ≈ 3-4) with an average peat depth of 2.27 m and basal age of the deepest centimeter of peat profiles ranging from 5,100 cal BP - 11,100 cal BP (Slater

et al., 2012; Griffiths and Sebestyen, 2016; McFarlane et al., 2018). Additional details about the study site can be found in Sebestyen et al. (2011).

The undulating hummock hollow surface of the S1 bog was the basis for the analyses in this paper. Access to experimental plots (nominally 12 m diameter) throughout the S1 bog was provided by a network of boardwalks installed for the SPRUCE experiment (Hanson et al., 2017b). Twelve plots were selected for scanning using TLS. Ten of the SPRUCE plots were enclosed for warming treatments, and two were open ambient plots. Each plot was surrounded by an octagonal boardwalk that formed the stable base from which TLS scans were obtained.

TLS Scans

All scans were collected using a Riegl VZ-1000 terrestrial laser scanner, which utilizes a 1550 nm laser to produce a 3-dimensional representation of the surrounding area (point cloud; Figure 2.1A). Four TLS scans were taken per SPRUCE plot and subsequently registered together in RiSCAN PRO to produce a single point cloud for each SPRUCE plot (Graham et al., 2019a). The SPRUCE plots were scanned in April-May of 2016, 2017, and 2018, with an angular resolution of 0.04 degrees. Scanning was performed early in the year following snowmelt so that the bog surface wasn't obscured by later development of shrub-layer canopies of plant foliage.

Surface Reconstruction

Point clouds were processed to retain points within the boardwalk (~ 9 m edge-to-edge) of each SPRUCE plot. Small areas within the scanned plot were occupied by large flux collars (Hanson et al., 2017a) that inhibited laser pulses from assessing the bog surface and were excluded from the analysis. To reconstruct the bog surface, the data

were filtered to extract the lowest return in a 2D grid, with grid cells measuring 0.1 x 0.1 m. A surface mesh was created using the Poisson surface reconstruction (Figure 2.1B) (Kazhdan et al., 2006) plugin for CloudCompare v2.8 (CloudCompare, 2017), which is capable of reconstructing surfaces from noisy data. This mesh was sampled to discretize the surface and generate a DEM with 0.01 m grid cells (Graham et al., 2019b). DEMs in this study primarily represent the top of *Sphagnum* capitula. In locations where there was no *Sphagnum* coverage, DEMs represent the top of other low stature vegetation (e.g., feather mosses) or bare earth.

Surface Roughness and Elevation Variability

Quantitative characterizations of peatland microtopography in the literature are sparse, although model representations that can utilize detailed topographic data including elevation distributions, such as DigiBog, are currently in use (Baird et al., 2011). Further, elevation distributions can be used in conjunction with measures of biogeochemical processes made along an elevation, or the associated water table depth, gradient (e.g., Moore and Knowles, 1989; Bubier et al., 1993; Bubier et al., 2003; Moore et al., 2011) to make spatial extrapolations of quantities of interest. Therefore, providing characterizations of microtopography that are related to elevation gradients and spatial variability will help improve model simulations of peatland dynamics and facilitate more accurate estimates of biogeochemical fluxes. In this study I provide four measures of microtopography in SPRUCE plots (for the 2017 dataset) that are based on elevation distributions, spatial variability, and surface roughness of peatland microtopography.

Elevation Distributions

Elevation distributions were unimodal and fairly well approximated by normal distributions, however elevation distributions were typically skewed left and had positive kurtosis (Figure 2.2). Therefore, I utilized Pearsons Distributions (Pearson, 1895; Pearson, 1901; Pearson, 1916; Johnson, 1949) to represent elevation distributions to deal with skewness and kurtosis. The Pearson Distributions are a family of probability distributions which use 2-4 parameters to generate continuous probability density functions. The type of Pearson's Distributions and the Parameters were calculated using the "pearsonFitML" function in the Program R (R Core Team, 2017) package "PearsonDS". Distributions were fit to the twelve SPRUCE plots individually and combined.

Random Roughness

Random roughness (RR) and its variants are among the simplest and most commonly used surface roughness metric which refer to measures of variation in elevation without consideration for the spatial arrangement of roughness elements. Previous studies have used both standard error (Allmaras et al., 1966; Currence and Lovely, 1970) and standard deviation (σ) (Kamphorst et al., 2000; Moreno et al., 2008; Vermang et al., 2013) as measures of variability. Here, I calculate RR as σ of elevation from the DEM cells for the twelve individual SPRUCE plots and plots combined.

DEM Roughness Length

Roughness length (z_0) is a measure of surface roughness, which is used to characterize microtopography (Campbell et al., 2002; Brubaker et al., 2013), that is a representation of roughness elements and corresponds to the point at which the wind

speed is zero in the log wind profile. Therefore, z_0 can be used to represent the influence of microtopography on turbulence and the resulting effect on surface mass and energy fluxes (Choudhury et al., 1979; Campbell et al., 2002). Studies using z_0 have calculated the parameter in many ways, from calculating using RR and simple transect based approaches (Kuipers, 1957; Lettau, 1969), to more sophisticated DEM and point cloud approaches (Smith et al., 2016; Miles et al., 2017). Here I calculate z_0 using the DEM method described in Smith et al. (2016) for each of the twelve SPRUCE plots.

Model Semivariograms

Semivariograms describe the spatial correlation of random data fields, and when applied to elevation can be used to describe topographic morphology and surface roughness (Darboux et al., 2002; Smith and Warburton, 2018). Empirical semivariograms plot the semivariance against the lag distance separating points (Figure 2.3), and the model semivariogram can be fit to the empirical semivariogram using three parameters: range (*r*), sill (*s*), and nugget (*n*). In this study, I fit exponential model variograms to empirical semivariograms consisting of 10,000 random samples from each SPRUCE plot. Our sampling intervals were sufficiently small and *n* appeared to be absent or extremely small in empirical semivariograms, therefore I set *n* in all model variograms to zero. Parameters *s* and *r* were calculated for each SPRUCE plot and combined.

Microform Classification Methods

Hollows can qualitatively be defined as low areas, or depressions within the peatland that are often in close proximity to the water table relative to the surrounding area. Hummocks are defined as higher mounds rising above the hollows, which results in perched peat/root complexes that are further from the water table. For applications that

utilize stratified sampling of each microform (e.g., Kim and Verma, 1992; Waddington and Roulet, 1996; Sullivan et al., 2008), such definitions may be sufficient because investigators can select areas to sample that most embody these qualitative definitions. However, subjective selection of sampling points in the most representative areas (i.e., extremes of both microforms, top of hummocks and bottom of hollows) is inadequate to quantitatively scale small-footprint measured data across the complete landform (see Moore et al. 2019). Further, these qualitative descriptions lack sufficient detail to classify microforms from a DEM.

Modeling studies utilizing simplified two column approaches to microtopography, for example Shi et al. (2015) and Frolking et al. (2002), represent microforms as soil columns which are differentiated by elevation. In contrast, field investigators placing instrumentation may consider qualitative metrics in addition to elevation (e.g., mounds, depression-like, transitional slopes and flat or planar areas). This demonstrates that the conceptualization of microforms is application specific, and therefore, so should classification schemes.

Microform classification schemes should target specific objectives and be explicitly defined, as to not confound analyses spanning multiple studies. Stovall et al. (2019) marks a major advance towards more useful methods to quantify wetland microforms, however the study used subjective manual delineations of hummocks as validation data. To address the need for explicit microform classification schemes, I developed quantitative methods to classify microforms for three purposes that differ in their conceptualize of microforms a) the Functional_Classification classifies microforms based on how the structure of microtopography interacts with ecological drivers to

determine ecological function; b) the ELM_Classification is designed to generate microtopographic parameters that are most consistent with the conceptualization of microtopography in a land surface model, ELM_SPRUCE (see below); and c) the Scaling_Classification is constructed to classify microforms in a manner consistent with the subjective placement of instrumentation in the field, and meant to be used to make spatial extrapolations. To accommodate each of these applications, classification methodologies were customized to be best suited for each individual application. For Functional_Classification, I incorporated water table depth data so that classifications using this method would be representative of ecological function, rather than simply reflect structure. To provide the best estimates of microtopographic model parameters, ELM_Classification only considers relative elevation, which is consistent with the representation of microtopography in the model. Scaling_Classification is intended to be used for scaling point, or small footprint, measurements to larger spatial extents. Therefore, it attempts to classify peatland microtopography in a manner most consistent with the placement of instrumentation by researchers in the field.

Method 1: Functional_Classification

I used depth to water table as a link to ecological function and as a classification metric because it is related to multiple ecological processes including *Sphagnum* photosynthesis and CH_4 flux. Water table is measured at each SPRUCE plot. Thus, I used the plot-specific daily-mean warm-season median water table (WSMWT hereafter) and a tolerance for a classification threshold for microforms (Figure 2.4). The warm, or ice-free, season was defined as the period when air temperatures remained above 0°C. This classification method differs from the two others because microform coverage can

change annually even if there is no change to the structure of the microtopography. This enables us to classify microforms to represent changes in ecosystem function incurred by changes in water table depth. For instance, increased evapotranspiration in the warmest SPRUCE plots (+9° C) may cause areas that would typically function in a hollow-like manner to function more like hummocks because of lower water tables due to drying.

Microform class was determined by whether the elevation was above or below the WSMWT plus the tolerance, as shown in equation 1:

$$\text{Eqn 1. } C_F(x,y) = \begin{cases} Hu, if \;\; z_{xy} \geq (zwt_{p50} + Tol) \\ Ho, if \;\; z_{xy} < (zwt_{p50} + Tol) \end{cases}$$

where *x* and *y* are geospatial coordinates (i.e., northing and easting), $C_F(x,y)$ is the Functional_Classification at location *xy*, Hu and Ho are hummock and hollow classifications respectively, z_{xy} is the elevation at location *xy*, zwt_{p50} is the plot-specific WSMWT, and *Tol* is a tolerance in meters.

The tolerance for elevations above WSMWT (0.10 m) was chosen based on desiccation levels of hollow-associated *Sphagnum* species relative to water table, and productivity relative to water content reported in Rydin (1985) and Schipperges and Rydin (1998), respectively. Rydin (1985) reports species of *Sphagnum* associated with hollows reach a water content of ≈ 750% (percent of dry weight) at a distance of ~ 0.10m from the water table, and this level of water content is associated with a sharp drop in *Sphagnum* photosynthesis (Schipperges and Rydin, 1998). This (0.1 m) is also the depth at which Christensen et al. (2003) suggested CH_4 emission is "turned on" or off, based on data from Greenland, Iceland, Scandinavia and Siberia. While this "on-off switch" for CH_4 emissions may not be representative of all peatlands, the 0.10 m from Christensen et al. (2003) is derived from five sites on multiple continents, and thus is likely

representative of northern peatlands over a broad geographic region. Therefore, a 0.10 m tolerance above the WSMWT represents an elevation threshold at which areas below should function ecologically like a hollow for at least half of the warm-season, and is used to classify microforms.

Method 2: ELM_Classification

Shi et al. (2015) have recently created a modified version of the Energy Exascale Earth System Model (E3SM) land model (ELM) that represent the hydrology and microtopography of peatlands. This modified version of ELM (referred to as ELM_SPRUCE) was created based on experiments at the SPRUCE site. ELM_SPRUCE uses a two-column approach to peatland microtopography, where one column is representative of hummocks and the other of hollows (similar to the representation in Frolking et al., 2002). These columns have identical soil and PFT properties, and only vary in elevation and water table depth. Modifications made by Shi et al. (2015) included the representation of near surface flow from hummock to hollow, lateral drainage to the lagg, and the glacial till acting as a barrier to vertical and lateral drainage. Shi et al. (2015) reported improved simulations of water table position but did not simulate biogeochemistry in ELM_SPRUCE. However, they state that peatland hydrology influences peatland C dynamics, and therefore these modifications to the hydrologic cycle will affect C cycling.

The ELM_SPRUCE approach to microtopography uses three uncertain parameters in the representation of microtopography: hummock-hollow height differential (0.3 m), hummock-hollow horizontal separation (1.0 m), and proportional cover of each microform (25% hollow; Shi et al., 2015). The current default values for

these parameters were obtained heuristically, and therefore the accuracy and uncertainty of the values are largely unknown. In this paper I developed methods that facilitate quantitative evaluation of such representations of microtopography, and their parameters.

A method using only information from the plot elevation distribution was used for a classification scheme to represent microtopography in a manner most consistent with how microtopography is represented in ELM_SPRUCE. Hummocks and hollows are represented in the model as soil columns that, other than elevation, have identical properties. Therefore, it is most consistent to classify microforms based on structure alone (elevation), and not include the water table position because it is simulated explicitly in ELM_SPRUCE. While similar techniques could be used for other models, I chose to focus on ELM_SPRUCE because it is configured based on the SPRUCE site and because it is able to couple to the Earth system model E3SM.

An elevation threshold was used for classification as a vertical tolerance from the plot elevation 5th percentile, where any points below the elevation threshold were classified as hollow and points above were classified as hummock (Figure 2.4). Explicitly:

$$\text{Eqn 2. } C_{ELM}(x,y) = \begin{cases} Hu, if \;\; z_{xy} \geq (z_{p5} + Tol) \\ Ho, if \;\; z_{xy} < (z_{p5} + Tol) \end{cases}$$

where $C_{ELM}(x,y)$ is the ELM_Classification at location xy, z_{p5} is the plot-specific elevation 5th percentile, and Tol is a tolerance in meters. The 5th percentile is intended to represent the elevation at the bottom of a 'typical' hollow, and was used instead of the plot minimum to mitigate any effect of extremely or erroneously low points. The tolerance used for the final classification was 0.10 m.

Method 3: Scaling_Classification

I created an index to classify microforms (Hollow Index) based on elevation, concavity, and slope. Considering researchers in the field often do not have access to metrics like the MWSWT or the elevation 5th percentile, these metrics are meant to be the quantitative counterparts to qualitative descriptors used by field researchers to identify microforms. This method, therefore, is aimed to provide classifications consistent with researchers identifying microforms in the field and best suited for scaling stratified measurements. For example, if I took stratified measurements of CH_4 flux in both hummocks and hollows, and wanted to make a bog-scale estimate of CH_4 flux, I would need to know the areal coverage of each microform. The Scaling_Classification method is aimed to provide microform areal coverages best suited for spatial extrapolations of similar stratified field measurements.

The Hollow Index is a product of the three metrics, after being passed through sigmoidal weighting functions (Figure 2.5). Sigmoid weighting functions are parameterized to accentuate "hollow-like" characteristics (i.e., low elevation, positive concavity, and relatively flat). The output of the Hollow Index is a continuous variable (Figure 2.6A&B), in which higher positive values correspond to the most hollow-like areas. Therefore, a threshold was applied to the Hollow Index to produce microform classification maps (Graham et al., 2019b). Thresholding for classifications can be application/user specific. Based on iterative thresholding I used 2.2 as our threshold (Figure 2.6C&D). Additional information and methods related to the parameterization of sigmoid weighting functions in the Hollow Index and Scaling_Classification can be found in the Supplemental Material.

Statistics

To evaluate the variability in hollow percent cover for a given plot across the three years (e.g. inter-annual (intra-plot) variability), I calculated the σ of percent cover for hollows for the three years of the study in each plot. A Kruskal-Wallis test was used to determine if there were differences in inter-annual variability between methods. Non-parametric tests were used because distributions were non-normal or heteroscedastic. Intra-annual (inter-plot) variability was defined as the variation in hollow percent cover of all plots within a given year, for each classification method, and was evaluated for each year of the study. Differences in intra-annual variability between methods was tested using Bartlett's tests. All statistical tests were conducted using Program R (R Core Team 2017) at $\alpha = 0.05$.

Results

Surface Reconstruction

The use of four scanning locations per plot reduced the effect of laser occlusion by vegetation, and yielded point densities sufficient (mean > 10 points cm^{-1}) for high quality surface reconstructions. The Poisson surface reconstruction (Kazhdan et al., 2006) performed well on the bog surface, and enabled accurate reconstructions and subsequent microform classifications, even when significant noise was present. The mean absolute error of reconstructed surfaces from 357 validation points was 0.057 m (for further details on DEM accuracy see the Supplemental Material).

Elevation Variation and Surface Roughness

Microtopography in all SPRUCE plots occurred on the scale of ~0.5 - 0.6 m, with the lowest elevation from all plots being -0.48 m and the highest being +0.31 m, relative to the plot means (Figure 2.2). Standard deviations in DEMs elevations (i.e., RR) in SPRUCE plots ranged from 0.06 - 0.08 m, with a mean = 0.07 m. Elevation distributions were typically skewed left and had positive kurtosis, with the majority of SPRUCE plots having the best fit Pearson's distribution be of type IV. Although type V and VI were also best fits for individual plots. Elevation distribution from all plots combined was best fit by a Pearson's distribution IV. Pearson's distribution type and associated parameters can be found in Table 2.1. The range parameter for plot semivariograms ranged from 0.92 - 1.89 m (mean = 1.30 m; σ = 0.30 m) and sills ranged from 0.003 - 0.006 m (mean = 0.004 m; σ = 0.001 m). DEM roughness length (Z_0) ranged from 0.004 - 0.005 m (mean = 0.004 m; σ = 0.0005 m). Semivariogram parameters and Z_0 estimates can be found in Table 2.2.

Microform Classifications

The three classification methods in this study had significantly different hollow coverages for all years combined ($\chi^2 = 47.55$, $df = 2$, $p < 0.001$). The three year mean areal coverage of hollows from Functional_Classification was intermediate (15.8%), but hollow coverages were markedly more variable than the two other methods (Figure 2.7). ELM_Classification produced the highest three year mean hollow coverage (33.8%). Hollow coverages from Scaling_Classification were the lowest and least variable (Figure 2.7) of the three methods, with a three year mean of 14.4%. Hollow coverages between methods were significantly different in all years and cases ($p < 0.05$), other than between

Scaling_Classification and Functional_Classification in 2017 ($W = 68$, $df = 1$, $p = 0.84$), Functional_Classification and ELM_Classification in 2018 ($W = 41$, $df = 1$, $p = 0.08$), and Functional_Classification and Scaling_Classification in 2018 ($W = 96$, $df = 1$, $p = 0.18$).

In general, the variability (inter and intra-annually) in hollow coverage between methods followed the pattern Functional_Classification >> ELM_Classification > Scaling_Classification (Table 2.3). Intra-annual variability was significantly different ($p < 0.05$) in all cases and years except ELM_Classification and Functional_Classification in 2016 ($\chi^2 = 0.57$, $df = 1$, $p = 0.45$). There was a significant difference in plot-specific inter-annual variability of hollow percent cover (Figure 2.8) between classification methods ($\chi^2 = 17.21$, $df = 2$, $p < 0.001$). Non-plot-specific hollow coverage between years was only significantly different for the Functional_Classification ($\chi^2 = 10.35$, $df = 2$, $p = 0.006$), further demonstrating its higher inter-annual variability.

The higher variability in the Functional_Classification was driven primarily by differences in MWSWT between plots and years (Figure 2.4A,E,I), rather than structural changes in the bog surface (Figure 2.4B,F,J), as was the case for ELM_Classification and Scaling_Classification. This is demonstrated by the lower variability in the plot elevation distributions 5^{th} percentiles (used in the ELM_Classification) between years (Figure 2.4B,F,J) compared to the relatively higher variability in MWSWT (Figure 2.4A,E,I). The Scaling_Classification and ELM_Classification both used only topographic data, however Scaling_Classification was less variable than the ELM_Classification because it incorporated multiple topographic metrics that are weighted based on plot distributions, and is therefore less affected by noise from surface reconstructions and plot minimum elevations. This may make Scaling_Classification a preferable choice for multi-year studies which desire interannual consistency in microform classifications. In this study,

the small changes in areal coverage of hollows between years using Scaling_Classification indicates small structural changes to the surface of the bog.

Discussion

To our knowledge, the only published studies that quantitatively classified peatland microforms with a DEM are Lovitt et al. (2018) and Stovall et al. (2019). Lovitt et al. (2018) used a moving window average as an elevation threshold to classify microforms (hummocks and hollows). However, our data demonstrate that elevation distributions are unimodal and not highly skewed (Figure 2.2). This indicates that the mean and median are similar, and therefore it is implicit that the proportion of hummocks and hollows will approximate 1:1 when using the local mean as a classification threshold. This is supported by the results in Lovitt et al. (2018) who report 51.8% percent cover for hollows (48.2% hummock) in undisturbed locations. Two of our classification methods (Functional_Classification and ELM_Classification) used elevation thresholds, similar to Lovitt et al. (2018). However, the elevation thresholds in this study were independent of plot elevation distributions and/or used a tolerance, which made classifications less prone to a bias towards a predetermined ratio of hummock:hollow.

The unimodal nature of elevation distributions in this study does not support the notion of microforms based on topography alone (at scales larger than a few meters). These results differ from those in Moore et al. (2019), which reports plots exhibiting both multimodal and unimodal elevation distributions. However, the plot size in Moore et al. (2019) was much smaller (3.8 - 10.6 m^2) than plots in this study (65.25 - 66.58 m^2), and some plots were specifically selected to have a distinct hummock and a distinct hollow. The discrepancy in modalities between our study and Moore et al. (2019) suggest that elevation distributions may be multi-modal at small scales that approximate the size of a

combination of hummock and hollow, but that the elevation distribution at scales much larger than microforms is unimodal and resembles a normal distribution. This is likely a result of microtopography having variable morphology (e.g., hummock-hollow height difference and microform length/width) at the peatland level; in which elevation distributions are multi-modal at smaller scales, but when aggregated at larger scales approximate a normal distribution. This scale dependency of distribution modality is an important distinction to make for modeling applications, and highlights the need to characterize microtopography at multiple scales. Future studies that sample microtopography at multiple scales in different peatland types would help elucidate inter-peatland variation and the scale-dependencies of elevation distributions.

While our data do not support the conceptualization of microforms based on form alone (i.e., topography), non-linear responses of biogeochemical processes to water table depth (e.g., Rydin, 1985; Moore and Knowles, 1989; Schipperges and Rydin, 1998; Christensen et al., 2003) paired with variability in water table depth incurred by microtopography, may result in microforms that are differentiable by ecological function. Our Functional_Classification differentiated microforms by ecological function through the incorporation of water table in a manner that is representative of two nonlinear responses to water table depth. However, it should be noted that this classification likely is not representative of all relationships between biogeochemical processes and water table depth (see difference between CH_4 and CO_2 flux response to water table in Moore and Knowles, 1989), but could be modified to address specific processes.

On annual timescales, classification results based purely on microform structure diverged from the Functional_Classification. This is demonstrated in Figure 2.4, where a

relatively low warm-season water table (2016; Figure 2.4A) resulted in low areal coverage of hollows from the Functional_Classification (Figure 2.4C), and a relatively high warm-season water table (2017; Figure 2.4E) resulted in much higher areal coverage of hollows (Figure 2.4G). During this year, elevation distributions and results from the ELM_Classification were largely unchanged. This constitutes a 3x increase in the areal coverage of hollows from the Functional_Classification in the same year that coverage from the ELM_Classification, based purely on structure, increased by only $1/10^{th}$. Large changes to areal coverage from Functional_Classification in the three years of this study and in the absence of major structural changes, can be used to explain interannual variability in peatland C fluxes driven by differences in water table depth. For instance, differences in Functional_Classification areal coverage between years could be used to contextualize higher temperature response Q10 values for large-collar CH_4 flux measurements in 2017 and 2018 compared to 2016 from Hanson et al. (2017a).

While I focused on demonstrating how areal coverage of hollows varied between classifications, other parameters (e.g., hummock height, hummock-hollow spacing, locations of hollows, etc.) also varied. This highlights the importance of parameterizing microtopography in models from data generated by classification schemes that are in accordance with the conceptualization of microforms in the model. The ELM_Classification method in this study provides a classification scheme that facilitates data-driven parameterization of the three microtopographic parameters used in ELM_SPRUCE and models using similar representations, like the Peatland Carbon Simulator (PCARS; Frolking et al., 2002). For models which do not use a microform based approach (e.g., DigiBog in Baird et al., 2011), the elevation distributions and

DEMs provided in this study can be utilized to optimize elevation frequencies used to represent microtopography. Further, DEMs and measures of surface roughness reported here can be used to improve model representation of the microtopographic influence on the hydrologic cycle (e.g., Jan et al., 2018) and wind profiles.

This study provides data that facilitates spatial extrapolations for both measurements taken using the hummock-hollow dichotomy and along an elevation (or water table) gradient. Elevation distributions reported here, combined with relationships relating biogeochemical processes to elevation or water table depth can be combined to make estimates of fluxes that will be more accurate than those made using the much more generalized microform dichotomy. However, such relationships are not always available or feasible to build. Therefore, studies using the hummock-hollow dichotomy can use our Scaling_Classification to calculate, and threshold, the continuous Hollow Index to classify microforms consistent with their placement of instrumentation in the field. Modifying the parameters and classification threshold of the Hollow Index would enable investigators to account for application-specific sampling locations, or the inherent subjectivity of investigators placing field instrumentation prior to classification. Such actions would facilitate proper scaling of measurements, by using areal coverages representative of their sampling locations.

Ideally, TLS sampling and microform mapping would occur before field measurements are taken to ensure that appropriate locations/microforms are sampled sufficiently. SfM using handheld cameras or UAS has been proven effective for producing point clouds and DEMs of peatland microtopography (Mercer and Westbrook, 2016; Lovitt et al., 2018; Moore et al., 2019), and could be used as a lower-cost

alternative to TLS. Although, SfM is not without its own challenges, and UAS SfM would likely be best suited for peatlands that are treeless or have relatively low tree cover.

The differences in hollow areal coverage and the variability between classification methods clearly demonstrates how an intended purpose or application drives the conceptualization of microforms, the resulting classification, and ultimately the areal coverage (and other metrics) of microforms. Considering the marked differences in hollow areal coverage, and variability between microform classifications in this study, it is evident how conclusions drawn from research utilizing microform classifications could vary widely. Using an appropriate classification is essential for producing accurate results and conclusions.

I recognize that a single method for classifying microforms is likely not sufficient to accommodate all applications. Therefore, this study provides three quantitative and explicit microform classification schemes intended to be used for different applications. The applications discussed in this study primarily focus on the microtopography-water table depth relationship and associated processes affected by the resulting soil moisture gradient. These processes occur across environmental gradients (e.g., moisture, temperature, etc.) rather than in conceptual bins (hummocks and hollows), and when possible, should be represented as such. This study provides several measures of microtopography corresponding to elevation frequency distributions and spatial variability to be utilized by studies that treat microtopography as a gradient. However, quantifying these processes across gradients is not always possible, and thus requires investigators to bin or stratify their sampling. In such cases, clearly defined microforms

are a necessity for inter-study comparisons and proper scaling of stratified measurements. Therefore, it is imperative to clearly define what, exactly, defines each bin.

Acknowledgements

This material is based upon work supported by the U.S. Department of Energy, Office of Science, Office of Biological and Environmental Research. Jake Graham was supported under a contract between Oak Ridge National Laboratory and Boise State University (#4000145196) with funding for the SPRUCE project from the U.S. Department of Energy (DOE), Office of Science, Office of Biological and Environmental Research. Oak Ridge National Laboratory is managed by UT-Battelle, LLC, for DOE under contract DE-AC05-00OR22725. Additional funding was provided by the Department of Geosciences, Boise State University.

Table 2.1. Parameters for Pearson's Distributions fit to SPRUCE plot elevation frequency distributions. When type = 4, Par3 = m and Par4 = nu; when type = 5, Par3 = Shape (no fourth parameter), when type = 6, Par3 = a and Par4 = b.

Plot	Type	Location	Scale	Par3	Par4
4	4	0.24	0.21	9.64	19.80
6	6	0.40	-2.44	32.20	198.28
7	5	-0.94	148.56	159.44	NA
8	4	0.11	0.25	9.02	6.93
10	4	0.11	0.23	7.66	6.64
11	4	0.09	0.21	7.29	5.26
13	4	0.12	0.31	12.12	9.01
16	4	0.22	0.33	18.47	23.86
17	4	0.12	0.31	10.72	7.44
19	4	0.06	0.30	14.39	5.12
20	4	0.03	0.36	16.81	2.76
21	4	1.38	4.07	2602.59	1758.63
Combined	4	0.07	0.24	7.90	3.95

Table 2.2. Summaries of roughness metrics from SPRUCE plots. RR = random roughness, SV_Sill = semivariogram sill, SV_Range = semivariogram range, Z0 = aerodynamic roughness length, Min_Elev = minimum plot elevation relative to the mean, Max_Elev = maximum plot elevation relative to the mean.

Plot	RR	SV_Sill	SV_Range	Z0	Min_Elev	Max_Elev
	Meters					
4	0.078	1.34	0.0057	0.0042	-0.48	0.23
6	0.076	1.22	0.0056	0.0045	-0.42	0.22
7	0.075	0.97	0.0059	0.0049	-0.24	0.30
8	0.069	1.44	0.0038	0.0035	-0.37	0.23
10	0.072	1.36	0.0046	0.0038	-0.40	0.23
11	0.066	1.25	0.0040	0.0036	-0.40	0.24
13	0.072	1.78	0.0039	0.0043	-0.35	0.24
16	0.068	1.52	0.0039	0.0033	-0.39	0.20
17	0.076	1.59	0.0047	0.0038	-0.41	0.23
19	0.061	0.95	0.0037	0.0033	-0.29	0.20
20	0.066	1.04	0.0042	0.0037	-0.32	0.31
21	0.060	1.13	0.0028	0.0034	-0.34	0.21
Combined	0.070	1.30	0.0044	0.0039	-0.48	0.31

Table 2.3. Summary statistics for areal coverage of hollows in SPRUCE plots by year, and the duration of the study, for the all three classification methods.

Year	Statistic	Classification Method (%)		
		Functional	ELM	Scaling
2016	Mean	4.1	33.2	14.6
	Range	0.1 - 18.4	23.72 - 42.3	13.1 - 16.1
	Standard Deviation	5.2	6.7	1.1
2017	Mean	18.0	34.1	14.5
	Range	0.7 - 43.0	25.42 - 45	12.5 - 16.5
	Standard Deviation	15.9	5.9	1.3
2018	Mean	23.4	34.0	14.1
	Range	0.0 - 43.6	23.3 - 43.7	11.3 - 15.5
	Standard Deviation	14.7	5.7	1.3
Years Combined	Mean	15.8	33.7	14.4
	Range	0.0 - 43.6	23.3 - 45.0	11.3 - 16.5
	Standard Deviation	15.1	6.0	1.2

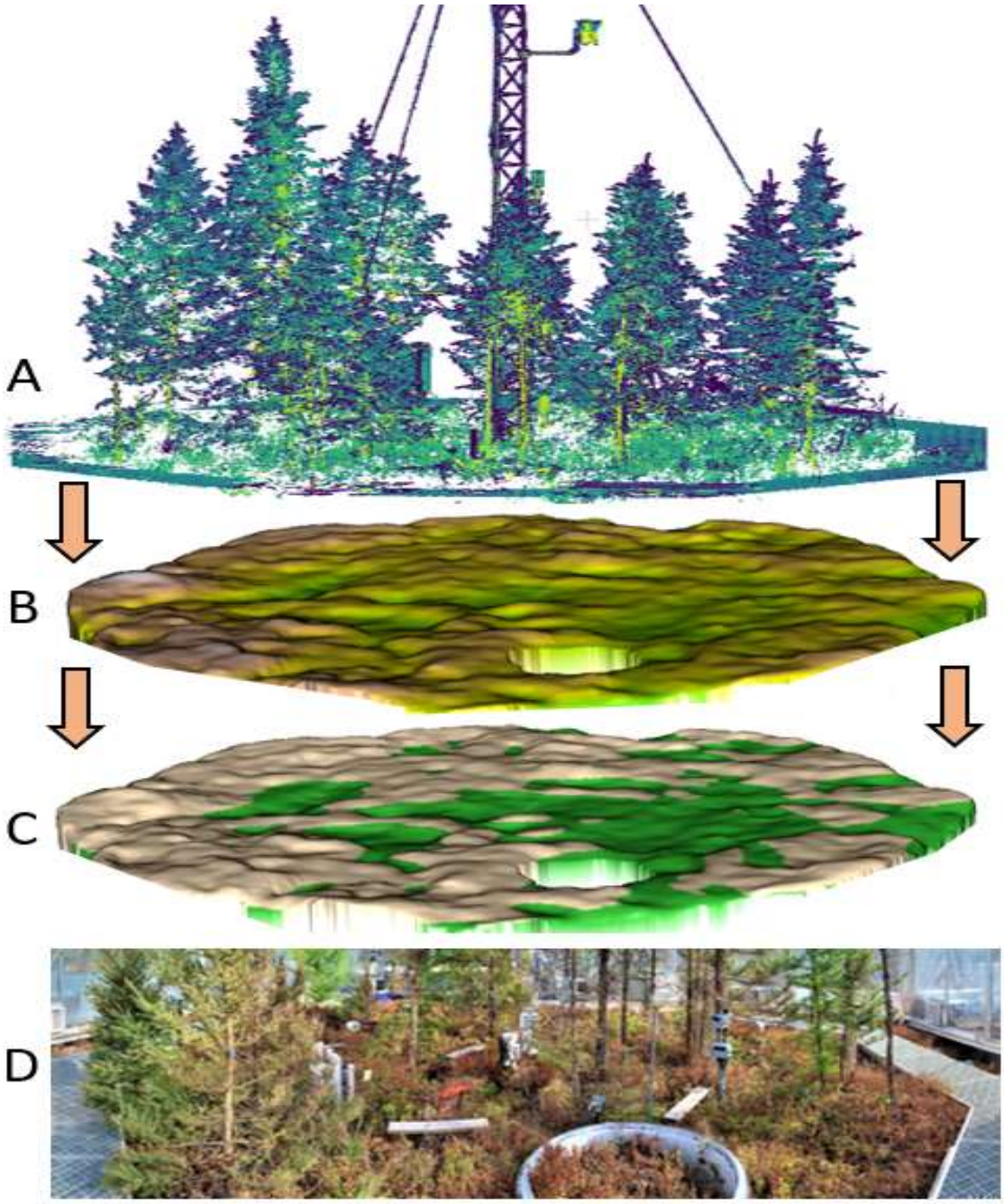

Figure 2.1. Workflow used to generate microform classification maps, starting with the terrestrial laser scanning point cloud (A; colored by intensity) used to generate the digital surface model (B; colored by elevation), and finally the microform classification map (C; colored by microform). SPRUCE plot 10 is used as an example. Additionally, an image of the mapped domain (D) showing one of the large flux collars that occluded laser scanner pulses and caused the "holes" in maps. Spatial scales between panes (A,B,C) are not exact; however, horizontal and vertical scales are 1:1 in individual panes.

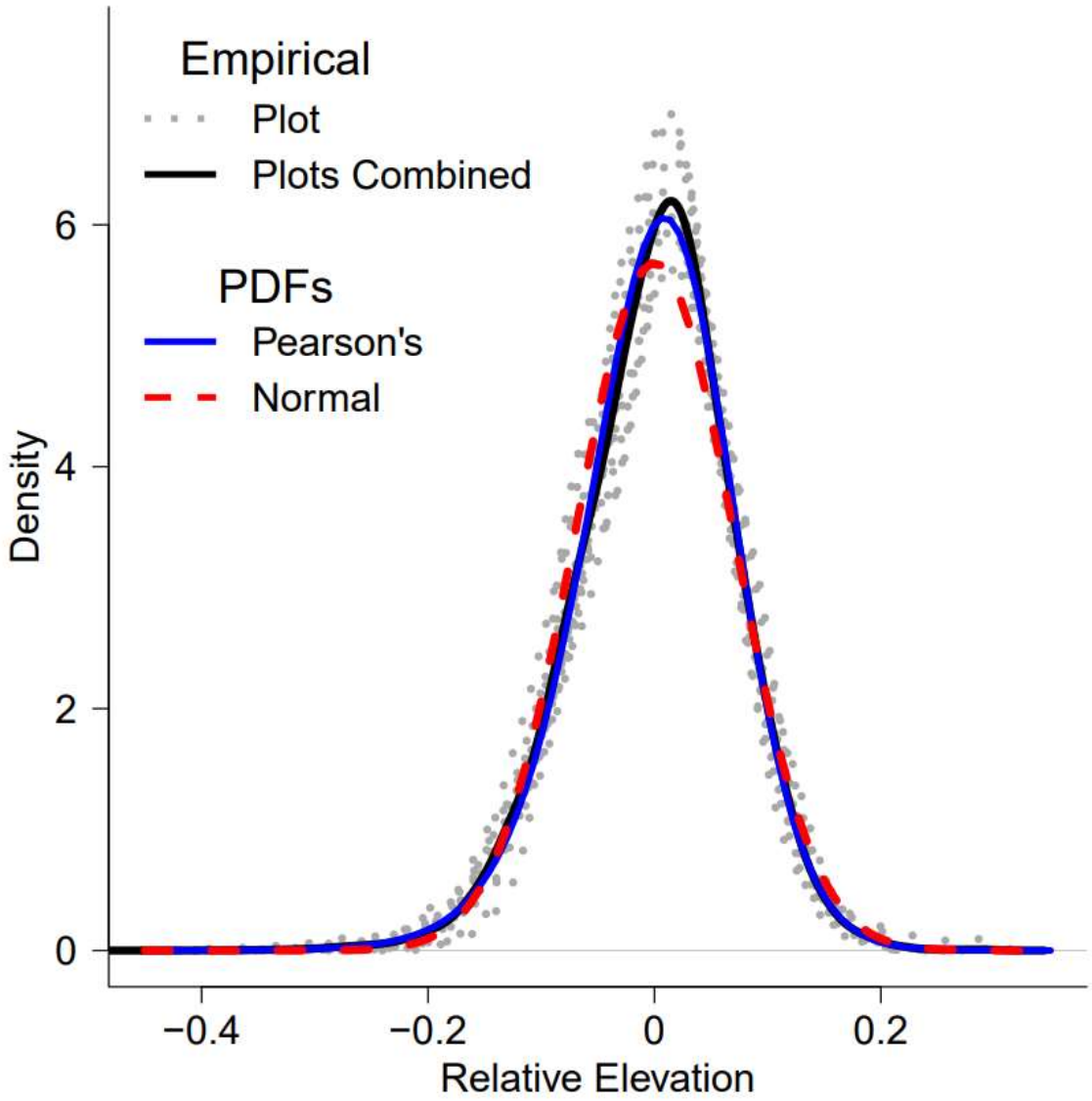

Figure 2.2. Elevation distributions for individual SPRUCE plots; also displaying the distribution for all SPRUCE plots combined with fit normal and Pearson's distributions.

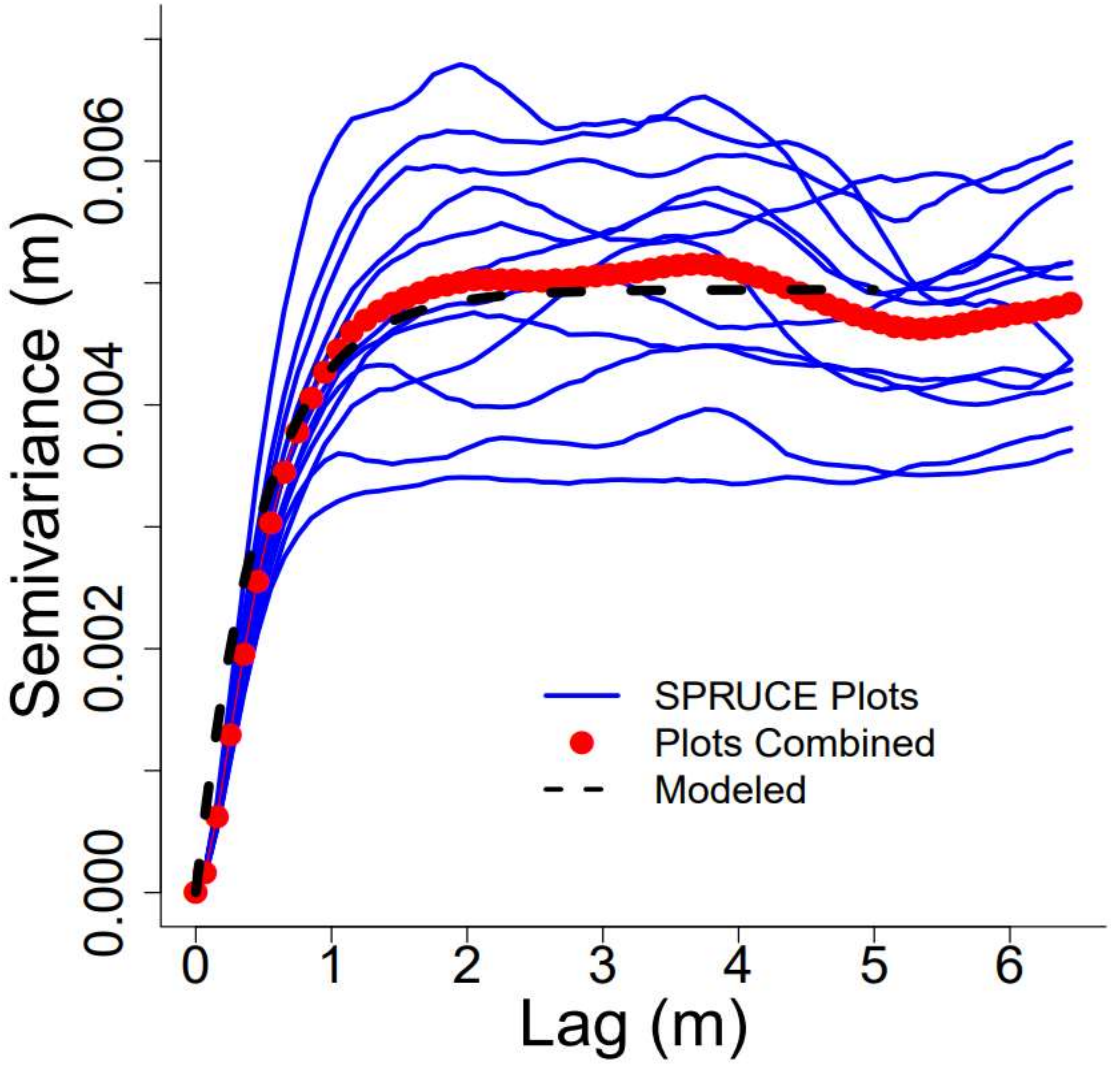

Figure 2.3. Empirical semivariograms for individual SPRUCE plots, also displaying the empirical and associated model semivariogram.

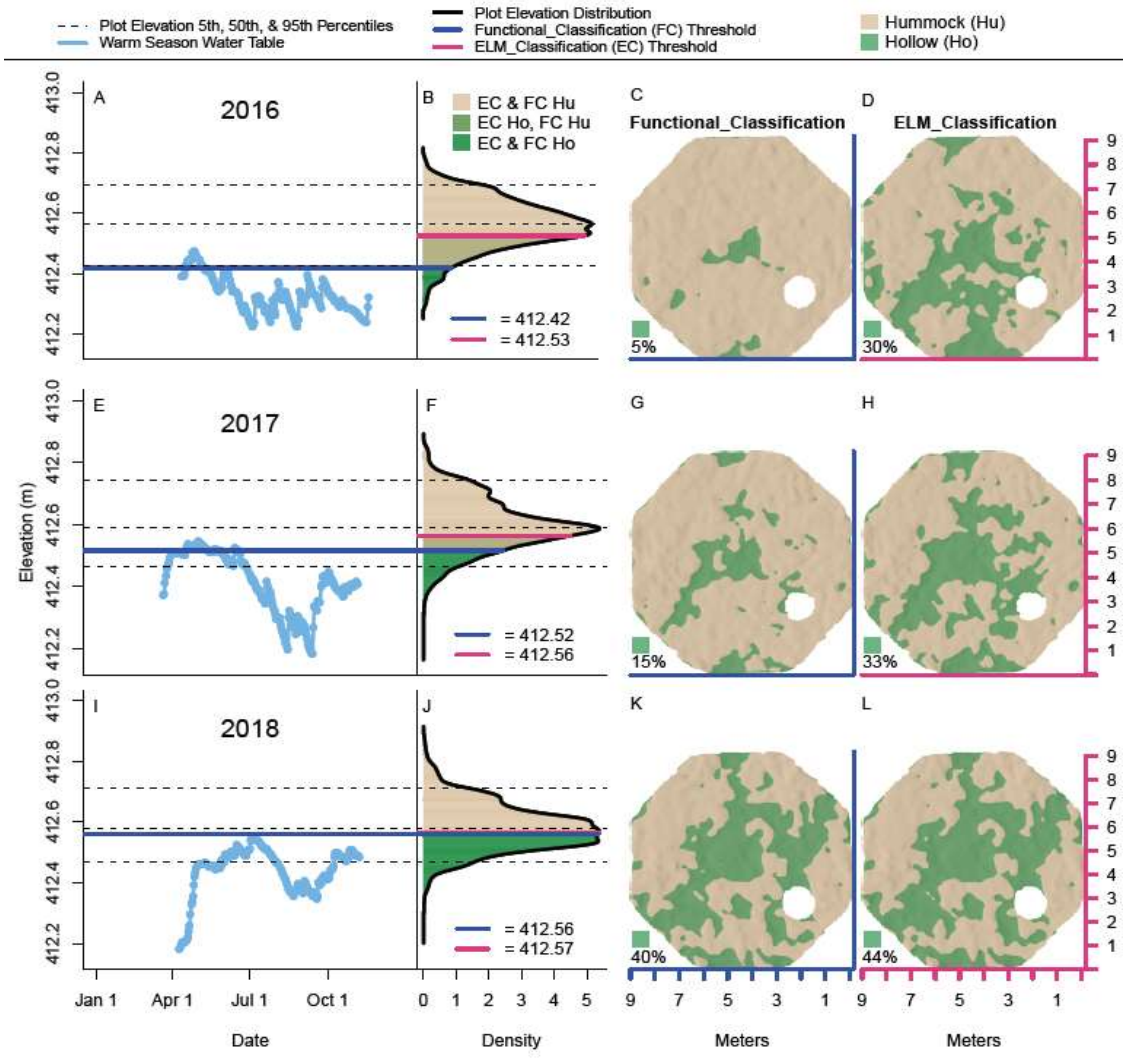

Figure 2.4. Warm-season water table (A), plot of digital surface model elevation distribution (B), and maps of classified microforms resulting from the thresholds displayed in B for the Functional_Classification and ELM_Classification (C,D, respectively) for SPRUCE plot 8 in 2016. The same is displayed for 2017 (E-H) and 2018 (I-L). To facilitate comparisons, plot elevation distributions (B,F,J) are displayed with elevation on the y-axes consistent with axes on warm-season water tables plots (A,E,I).

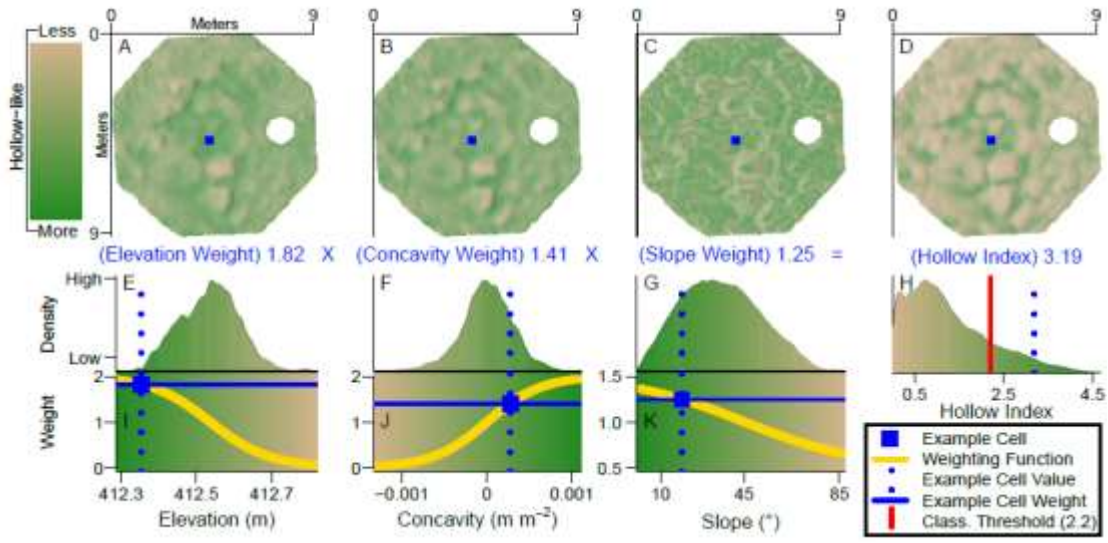

Figure 2.5. The upper panels (A-D) shows maps of SPRUCE plot 7 (2017) displaying Elevation, Concavity, Slope, and Hollow Index, respectively. The lower panel shows distributions of each variable (E-H) with the same X-axes as graphs of sigmoid weighting functions of each variable below (I,J,K), which are displayed on a background corresponding with map colorbars. An example grid cell is displayed on maps and on sigmoid weighting function plots, showing how variable values (elevation, concavity, slope) are used in weighting functions, and how the resulting weights are multiplied to calculate the Hollow Index. 04

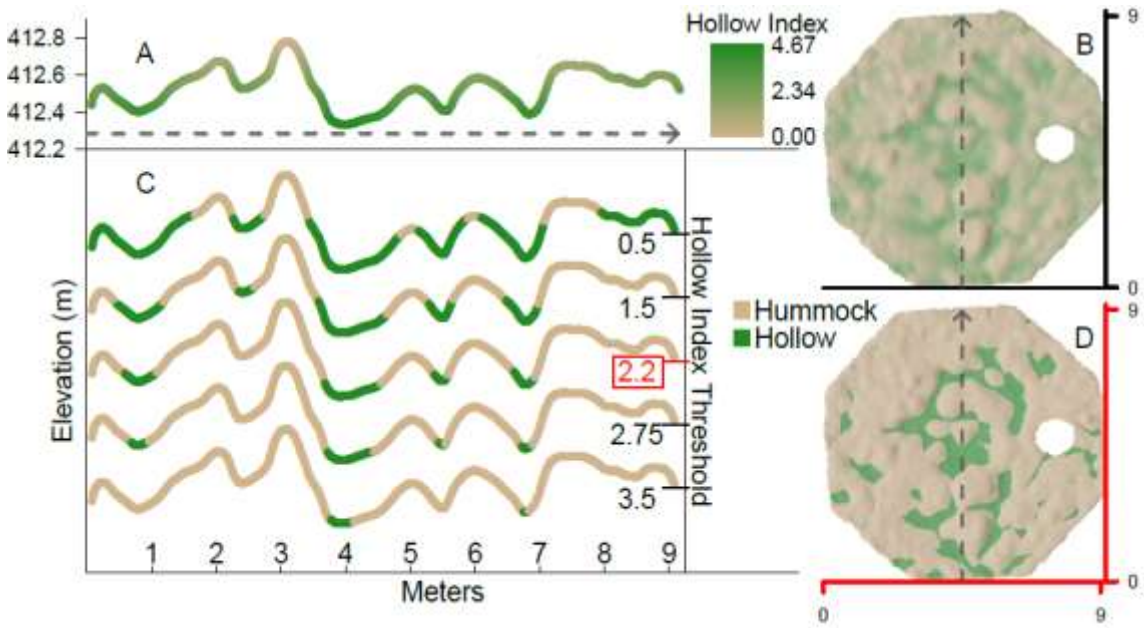

Figure 2.6. A profile of a transect (A) and a map (B) from SPRUCE plot 7 (2017) colored by the Hollow Index. The same transect classified into microforms using various Hollow Index thresholds (C), with a red box around the 2.2 threshold used for Scaling_Classification in this study, and the resulting microform classification map (D). Arrows show the location and orientation of the transect (A,C) on maps (B,D). Note that horizontal and vertical scales are not 1:1 in both A and C (i.e., the lengths that represent 1m along the x and y axes are not equal in both panes).

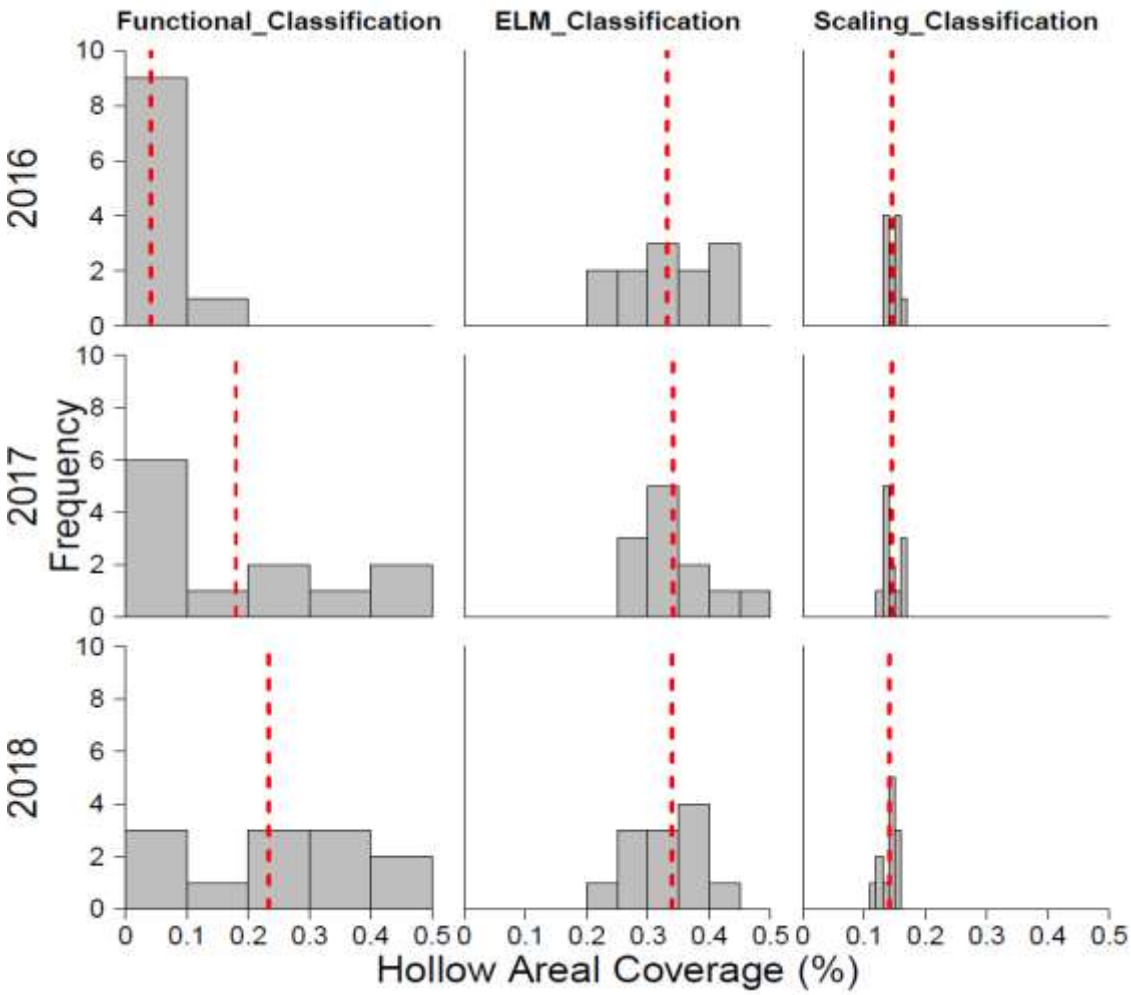

Figure 2.7. Histograms displaying the areal coverage of hollows from each classification, in all plots, in all years. Vertical red lines display means.

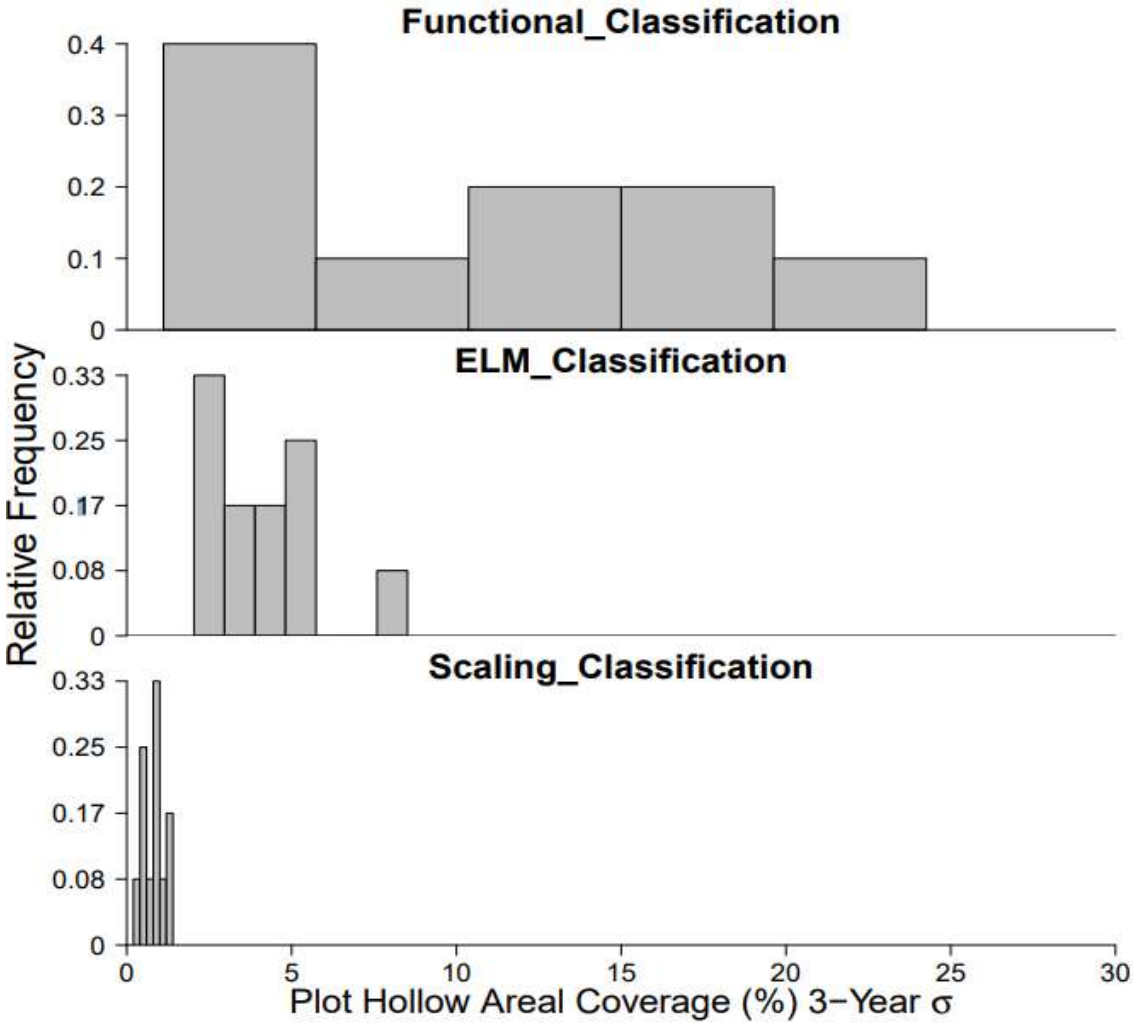

Figure 2.8. Histograms of plot-specific inter-annual variability for classification methods in all plots, calculated as the standard deviation (σ) of areal coverage of hollows for a given plot during the three years of the study.

References

Allmaras, R. R., R. E. Burwell, W. E. Larson, and F. E. Holt. 1966. Total porosity and random roughness of the interrow zone as influenced by tillage. Conservation Research Report 7. Washington, D.C. USDA.

Almendinger, J. C., J. E. Almendinger, and P. H Glaser. 1986. Topographic fluctuations across a spring fen and raised bog in the Lost River peatland, Northern Minnesota. Journal of Ecology 74:393-401.

Andrus, R., D. J. Wagner, and J. E. Titus. 1983. Vertical distribution of *Sphagnum* mosses along hummock-hollow gradients. Canadian Journal of Botany 61:3128-3139.

Arsenault, J., J. Talbot, T. R. Moore, M. P. Beauvais, J. Franssen, and N. T. Roulet. 2019. The spatial heterogeneity of vegetation, hydrology and water chemistry in a peatland with open-water pool. Ecosystems https://doi.org/10.1007/s10021-019-00342-4.

Baird, A. J., P. J. Morris, and L. R. Belyea. 2011. The DigiBog peatland development model 1: rationale, conceptual model, and hydrological basis. Ecohydrology 5:242-255.

Benscoter, B. W., K. R. Wieder, and D. H. Vitt. 2005. Linking microtopography with post-fire succession in bogs. Journal of Vegetation Science 16:453-460.

Brubaker, K. M., W. L. Myers, P. J. Drohan, D. A. Miller, and E. W. Boyer. 2013. The use of LiDAR terrain data in characterizing surface roughness and microtopography. Applied and Environmental Soil Science: Article ID 891534.

Bubier, J. L., D. Bhatia, T. R. Moore, N. T. Roulet, and P. M. Lafleur. 2003. Spatial and temporal spatial variability in growing-season net ecosystem carbon dioxide exchange at a large peatland in Ontario, Canada. Ecosystems 6:353-367.

Bubier, J., A. Cotello, T. R. Moore, N. T. Roulet, and K. Savage.1993. Microtopography and methane flux in boreal peatlands, northern Ontario Canada. Canadian Journal of Botany 71:1056-1063.

Campbell, D. R., C. Lavoie, and L. Rochefort. 2002. Wind erosion and surface stability in abandoned milled peatlands. Canadian Journal of Soil Science 82:85-95.

Cao, M., and F. I. Woodward. 1998. Net primary and ecosystem production and carbon stocks of terrestrial ecosystems and their responses to climate change. Global Change Biology 4:185-198.

Chapin, F. S., K. Van Cleve, and M. C. Chapin. 1979. Soil temperature and nutrient cycling in the tussock growth form of *Eriophorum vaginatum*. Journal of Ecology 76:169-189.

Chaudhary, N., P. A. Miller, and B. Smith. 2018. Biotic and abiotic drivers of peatland growth and microtopography: a model demonstration. Ecosystems 21:1196-1214.

Choudhury, B. J., T. J. Schmugge, A. Chang, and R. W. Newton. 1979. Effect of surface roughness on the microwave emission from soils. Journal of Geophysical Research 84:5699-5706.

Christensen, T. R., A. Ekberg, L. Strom, M. Mastepanov, N. Panikov, M. Oquist, B. H. Svensson, H. Nykanen, P. J. Martikainen, and H. Oskarsson. 2003. Factors controlling large scale variations in methane emissions from wetlands. Geophysical Research Letters 30:1414-1417.

CloudCompare (version 2.8) [GPL software]. 2017. Retrieved from http://www.cloudcompare.org/

Currence, H. D., and W. G. Lovely. 1970. The analysis of soil surface roughness. Transactions of American Society of Agricultural Engineers 13:710-714.

Damman, A. W. H. 1978. Distribution and movement of elements in ombrotrophic peat bogs. Oikos 30:480-495.

Darboux, F., P. Davy, C. Gascuel-Odoux, and C. Huang. 2002. Evolution of soil surface roughness and flowpath connectivity in overland flow experiments. Catena 46:125–39.

Darboux, F., and C. Huang. 2003. An instantaneous-profile laser scanner to measure soil surface microtopography. Soil Science Society of America Journal 67:92-99.

Ehrenfeld, J. G. 1995. Microtopography and vegetation in Atlantic white cedar swamps: the effects of natural disturbances. Canadian Journal of Botany 73:474–484.

Flanagan, D. C., C. Huang, L. D. Norton, and S. C. Parker. 1995. Laser scanner for erosion plot measurements. Transactions of the American Society of Agricultural and Biological Engineers 38:703-710.

Freeman, C., M. A. Lock, and B. Reynolds. 1993. Fluxes of CO_2, CH_4, and N_2O form a Welsh peatland following simulation of water table draw-down: potential feedback to climatic change. Biogeochemistry 19:51-60.

Frolking, S., N. T. Roulet, T. R. Moore, P. M. Lafleur, J. L. Bubier, and P. M. Crill. 2002. Modeling seasonal to annual carbon balance of Mer Bleue Bog, Ontario, Canada. Global Biogeochemical Cycles 15, 1030.

Fung, I., J. John, J. Lerner, E. Matthews, M. Prather, L. P. Steele, and P. J. Fraser. 1991. Three-dimensional model synthesis of the global methane cycle. Journal of Geophysical Research 96-13033-13065

Gorham, E. 1990. Biotic impoverishment in northern peatlands. Woodwell, G. M., editor. The earth in transition: patterns and processes of biotic impoverishment. New York: Cambridge University Press New York. p65-98.

Gorham, E. 1991. Northern Peatlands: Role in the carbon cycle and probable responses to climatic warming. Ecological Applications 1:182-195.

Graham, J. D., N. F. Glenn, and L. P. Spaete. 2019a. SPRUCE terrestrial laser scanning of experimental plots beginning in 2015. Oak Ridge National Laboratory, TES SFA, U.S. Department of Energy, Oak Ridge, Tennessee, U.S.A. https://doi.org/10.25581/spruce.067/1515552

Graham, J. D., N. F. Glenn, and L. P. Spaete. 2019b. SPRUCE microtopography of experimental plots derived from terrestrial laser scans beginning in 2016. Oak Ridge National Laboratory, TES SFA, U.S. Department of Energy, Oak Ridge, Tennessee, U.S.A. https://doi.org/10.25581/spruce.068/1515553

Griffiths, N. A., and S. D. Sebestyen. 2016. Dynamic vertical profiles of peat porewater chemistry in a Northern peatland. Wetlands 36:1119-1130.

Gunn, S. R. 1999. On the discrete representation of the Laplacian of Gaussian. Pattern Recognition 32:1463-1472.

Hanson, P. J., J. R. Phillips, J. S. Riggs, and W. R. Nettles. 2017a. SPRUCE Large-Collar in situ CO2 and CH4 flux data for the SPRUCE experimental plots. Whole-ecosystem-warming. Oak Ridge National Laboratory, TES SFA, U.S. Department of Energy, Oak Ridge, Tennessee, U.S.A. https://doi.org/10.3334/CDIAC/spruce.034

Hanson, P. J., J. S. Riggs, W. R. Nettles, J. R. Phillips, M. B. Krassovski, L. A. Hook, L. Gu, A. D. Richardson, D. M. Aubrecht, D. M. Ricciuto, J. M. Warren, and C. Barbier. 2017b. Attaining whole-ecosystem warming using air and deep soil heating methods with an elevated CO_2 atmosphere. Biogeosciences 14:861–883, doi: 10.5194/bg-14-861-2017

Harris, A., and A. J. Baird. 2018. Microtopographic drivers of vegetation patterning in blanket peatlands recovering from erosion. Ecosystems https://doi.org/10.1007/s10021-018-0321-6.

Hirano, T., J. Jauhiainen, T. Inoue, and H. Takahashi. 2009. Controls on the carbon balance of tropical peatlands. Ecosystems 6:873-887.

Huang, C., and J. M. Bradford. 1990. Portable laser scanner for measuring soil surface roughness. Soil Science Society of America Journal 54:1402-1406.

Huang, C., I. White, E. Thwaite, and A. Bendeli. 1988. A noncontact laser system for measuring soil surface topography. Soil Science Society of America Journal 52:350-355.

Jan, A., E. T. Coon, J. D. Graham, and S. L. Painter. 2018. A subgrid approach to modeling microtopography effects on overland flow. Water Resources Research 54:6153-6167.

Johnson, N. L. 1949. Systems of frequency curves generated by methods of translation. Biometrika 36:149-176.

Johnson, L. C., and A. W. H. Damman. 1991. Species-controlled *Sphagnum* decay on a Swedish raised bog. Oikos 61:234-242.

Johnson, L. C., A. W. H. Damman, and N. Malmer. 1990. Sphagnum macrostructure as an indicator of decay and compaction in peat cores from an ombrotrophic south Swedish peat-bog. Journal of Ecology 78:633-647.

Kamphorst, E. C., V. Jetten, J. Guerif, J. Pitkanen, B. V. Iversen, J. T. Douglas, and A. Paz. 2000. Predicting depressional storage from soil surface roughness. Soil Science Society of America Journal 64:1749-1758.

Kazhdan, M., M. Bolitho, and H. Hoppe. 2006. Poisson surface reconstruction. Symposium on Geometry Processing 61–70.

Kim, J., and S. B. Verma. 1992. Soil Surface CO_2 flux in a Minnesota peatland. Biogeochemistry 18:32-51.

Kuipers, H. 1957. A reliefmeter for soil cultivation studies. Netherlands Journal of Agricultural Science 5:255-267.

Lettau, H. 1969. Note on aerodynamic roughness-parameter estimation on the basis of roughness-element description. Journal of Applied Meteorology 8:828-832.

Lovitt, J., M. M. Rahman, S. Saraswati, G. J. McDermid, M. Strack, and B. Xu. 2018. UAV remote sensing can reveal the effect of low-impact seismic lines on surface morphology, hydrology, and methane (CH_4) release in a boreal treed bog. Biogeosciences 123:1117-1129.

Lucieer, A., D. Turner, D. H. King, and S. A. Robinson. 2014. Using an Unmanned Aerial Vehicle (UAV) to capture micro-topography of Antarctic moss beds. International Journal of Applied Earth Observation and Geoinformation, 27, 53-62.

Malhotra, A., N. T. Roulet, P. Wilson, X. Giroux-Bougard, and L. I. Harris. 2016. Ecohydrological feedbacks in peatlands: an empirical test of the relationship among vegetation, microtopography and water table. Ecohydrology 9:1346-1357.

McFarlane, K. J., P. J. Hanson, C. M. Iversen, J. R. Phillips, and D. J. Brice. 2018. Local spatial heterogeneity of Holocene carbon accumulation throughout the peat profile of an ombrotrophic Northern Minnesota bog. Radiocarbon 60:941-962.

Mercer, J. J., and C. J. Westbrook. 2016. Utrahigh-resolution mapping of peatland microform using ground-based structure from motion with multiview stereo. Journal of Geophysical Research: Biogeosciences 121:2901-2916.

Miles, E. S., J. F. Steiner, and F. Brun. 2017. Highly variable aerodynamic roughness length (z_0) for a hummocky debris-covered glacier. Journal of Geophysical Research: Atmospheres 122:8447-8466.

Moreno, R. G., M. C. Diaz Alvarez, A. Saa Requejo, and A. M. Tarquis. 2008. Multifractal analysis of soil surface roughness. Vadose Zone Journal 7:512-520.

Moore, T. R. 1989. Growth and net production of *Sphagnum* at five fen sites, subarctic eastern Canada. Canadian Journal of Botany 67:1203-1207.

Moore, T. R., and M. Dalva. 1993. The influence of temperature and water table position on carbon dioxide and methane emissions from laboratory columns of peatland soils. Journal of Soil Science 44:651-664.

Moore, T. R., A. De Young, J. L. Bubier, E. R. Humphreys, P. M. Lafleur, and N. T. Roulet. 2011. A multi-year record of methane flux at the Mer Bleue Bog, Southern Canada. Ecosystems 14:646-657.

Moore, T. R., and R. Knowles. 1989. The influence of water table levels on methane and carbon dioxide emissions from peatland soils. Canadian Journal of Soil Science 69:33-38.

Moore, P. A., M. C. Lukenbach, D. K. Thompson, N. Kettridge, G. Granath, and J. M. Waddington. 2019. Assessing the peatland hummock-hollow classification framework using high resolution elevation models: implications for appropriate complexity ecosystem modeling. Biogeosciences 16:3491-3506.

Morris, P. J., G. T. Swindles, P. J. Valdes, R. F. Ivanovic, L. J. Gregoire, M. W. Smith, L. Tarasov, A. M. Haywood, and K. L. Bacon. 2018. Global peatland initiation driven by regionally asynchronous warming. PNAS 115:4851-4856.

Morris, P. J., J. M. Waddington, B. W. Benscoter, and M. R. Turetsky. 2011. Conceptual frameworks in peatland ecohydrology: looking beyond the two-layered (acrotelm-catotelm) model. Ecohydrology 4:1-11.

Munir, T. M., and M. Strack. 2014. Methane flux influenced by experimental water table drawdown and soil warming in a dry boreal continental bog. Ecosystems 7:1271-1285.

Nouwakpo, S. K., M. R. James, M. A. Weltz, C. H. Huang, I. Chagas, and L. Lima. 2014. Evaluation of structure from motion for soil microtopography measurement. The Photogrammetric Record 29:297-316.

Nouwakpo, S. K., W. A. Weltz, and K. McGwire. 2016. Assessing the performance of structure- from- motion photogrammetry and terrestrial LiDAR for reconstructing soil surface microtopography of naturally vegetated plots. Earth Surface Processes and Landforms 41:308-322.

Nungesser, M. K. 2003. Modelling microtopography in boreal peatlands: hummocks and hollows. Ecological Modelling 165:175-207.

Pearson, K. 1895. Contributions to the mathematical theory of evolution, II: skew variation in homogeneous material. Philosophical Transactions of the Royal Society 186:343-414.

Pearson, K. 1901. Mathematical contributions to the theory of evolution, X: supplement to a memoir on skew variation. Philosophical Transactions of the Royal Society 197:287-299.

Pearson, K. 1916. Mathematical contributions to the theory of evolution, XIX: second supplement to a memoir on skew variation. Philosophical Transactions of the Royal Society 216:538-548.

Post, R. M., W. R. Emanuel, P. J. Zinke, and A. G. Stangenberger. 1982. Soil carbon pools and world life zones. Nature 298:156-159.

Pouliot, R., L. Rochefort, and E. Karofeld. 2011. Initiation of microtopography in revegetated cutover peatlands. Applied Vegetation Science 14:158-171.

R Core Team. 2017. R: A language and environment for statistical computing. R Foundation for Statistical Computing, Vienna, Austria. URL https://www.R-project.org/

Rydin, H. 1985. Effect of water level on desiccation of Sphagnum in relation to surrounding Sphagna. Oikos 45:374-379.

Scharlemann, P. W., E. V. J. Tanner, R. Hiederer, and V. Kapos. 2014. Global soil carbon: understanding and managing the largest terrestrial carbon pool. Carbon Management 5:81-91. https://doi.org/10.4155/cmt.13.77

Schipperges, B., and H. Rydin. 1998. Response of photosynthesis of Sphagnum species from contrasting microhabitats to tissue water content and repeated desiccation. New Phytologist 140:677-684.

Sebestyen, S. D., C. Dorrance, D. M. Olson, E. S. Verry, R. K. Kolka, A. E. Elling, and R. Kyllander. 2011. Longterm monitoring sites and trends at the Marcell Experimental Forest. In: Kolka, R. K., S. D. Sebestyen, E. S. Verry, and K. N. Brooks, editors. Peatland Biogeochemistry and Watershed Hydrology at the Marcell Experimental Forest. Boca Raton Florida: CRC Press, p15-72.

Shi, X., P. E. Thornton, D. M. Ricciuto, P. J. Hanson, J. Mao, S. D. Sebestyen, N. A. Griffiths, and G. Bisht. 2015. Representing northern peatland microtopography and hydrology within the Community Land Model. Biogeosciences 12:6463-6477.

Slater, L., P. J. Hanson, L. A. Hook. 2012. SPRUCE S1 Bog Peat Depth Determined by Push Probe and GPR: 2009-2010. Oak Ridge National Laboratory, TES SFA, U.S. Department of Energy, Oak Ridge, Tennessee, U.S.A.https://doi.org/10.3334/CDIAC/spruce.002

Smith, M. W., D. J. Quincey, T. Dixon, R. G. Bingham, J. L. Carrivick, T. D. L. Irvine-Fynn, and D. M. Rippin. 2016. Aerodynamic roughness of glacial ice surfaces from high-resolution topographic data. Journal of Geophysical Research: Earth Surface 121:748-766.

Smith, M. V., and J. Warburton. 2018. Microtopography of bare peat: a conceptual model and objective classification from high-resolution topographic survey data. Earth Surface Processes and Landforms 43:1557-1574.

Stovall, A. E. L., J. S. Diamond, R. A. Slesak, D. L. McLaughlin, and H. Shugart. 2019. Quantifying wetland microtopography with terrestrial laser scanning. Remote Sensing of Environment 232, 111271.

Sullivan, P. F., S. J. T. Arens, R. A. Chimner, and J. M. Welker. 2008. Temperature and microtopography interact to control carbon cycling in a high Arctic fen. Ecosystems 11:61-76.

Vermang, J., L. D. Norton, J. M. Baetens, C. Huang, W. M. Cornelis, and D. Gabriels. 2013. Quantification of soil surface roughness evolution under simulated rainfall. Transaction of the American Society of Agricultural and Biological Engineers 56:505-514.

Waddington, J. M., and N. T. Roulet. 1996. Atmosphere-wetland carbon exchanges: Scale dependency of CO_2 and CH_4 exchange on the developmental topography of a peatland. Global Biogeochemical Cycles 10:233-245.

Walker, A. J., K. R. Carter, L. Gu, P. J. Hanson, A. Malhotra, R. J. Norby, S. D. Sebestyen, S. D. Wullschleger, and D. J. Weston. 2017. Biophysical drivers of seasonal variability in Sphagnum gross primary production in a northern temperate bog. Journal of Geophysical Research: Biogeosciences 122:1078-1097.

Weltzin, J. F., C. Harth, and S. D. Bridgham. 2001. Production and microtopography of bog bryophytes: response to warming and water-table manipulations. Oecologia 128:557:656.

Yu, Z. 2011. Holocene carbon flux histories of the world's peatlands: global carbon-cycle implications. The Holocene 21:761-774.

Yu, Z. 2012. Northern peatland carbon stocks and dynamics: a review. Biogeosciences 9:4071-4085.

Yu, Z., D. W. Beilman, S. Frolking, G. M. MacDonald, N. T. Roulet, P. Camill, and D. J. Charman. 2011. Peatlands and their role in the global carbon cycle. EOS 92:97-108.

Yu, Z. C., J. Loisel, D. P. Brosseau, D. W. Beilman, and S. J. Hunt. 2010. Global peatland dynamics since the Last Glacial Maximum. Geophysical Research Letters 37.

CHAPTER THREE: IMPROVING THE PARAMETERIZATION OF MICROTOPOGRAPHY AND QUANTIFYING THE RESULTING EFFECT ON THE CARBON CYCLE

Abstract

Northern peatlands are a major terrestrial carbon store, with an annual sink of 0.1 Pg C yr^{-1} and a total storage estimate of 547 Pg C. Northern peatlands are also major contributors of atmospheric methane. As the climate warms, peatlands are predicted to increase carbon release to the atmosphere, resulting in a positive feedback loop. Most land surface models do not accurately represent peatland carbon emissions, likely because they do not represent the hydrologic cycle and/or microtopography adequately. Interactions between water table depth and microtopography in peatlands influence decomposition and modulate CO_2 and CH_4 fluxes. A modified version of ELM, the land surface component of Energy Exascale Earth System Model (E3SM), has been created to represent the microtopography and hydrology of a raised dome bog (ELM_SPRUCE). Three microtopographic parameters are used in ELM_SPRUCE: hummock height, hummock-hollow spacing, and percent hollow. Here we test the sensitivity of a suite of quantities of interest (QOI) associated with the carbon cycle to these microtopographic parameters. Our results suggest that carbon related QOI were typically the most sensitive to hummock height, and that QOI were sensitive to interactions between parameters.

Furthermore, net ecosystem exchange was the QOI most relatively influenced by microtopographic parameters in ELM_SPRUCE, varying by 26.9%. We found that increasing hummock height resulted in more C being stored in plant tissue and less in soil organic matter, which coincided with decreases in *Sphagnum* net primary production (NPP) and increases in *Picea* and shrub NPP.

Introduction

Northern Peatlands are an important component of the global carbon (C) cycle due to their ability to slowly accumulate C into substantial storage reservoirs. The ability of northern peatlands to store C is due to the unique environmental conditions that are characteristic of these ecosystems, which include shallow water tables, moist acidic soils, low nutrient content, and cool temperatures. These conditions, especially moist soils, slow microbial decomposition and reduce the rate at which C is released to the atmosphere through heterotrophic respiration (H_R). The slow rate of microbial decomposition in peatlands leads to an imbalance in C inputs and outputs to the system, with C inputs slightly higher than C outputs resulting in a net C sink. While the rate of C storage is relatively small (20-30 g C m^{-2} yr^{-1}; Yu et al., 2011), this storage has been occurring for the last ~ 7,000-14,000 years (Yu, 2011; Morris et al., 2018), which results in substantial quantities of C stored in peatlands globally. Estimates of global peatland C storage are as high as one third of global terrestrial C (Gorham, 1990; Cao and Woodward, 1998; Yu et al., 2010; Yu, 2012; Scharlemann et al., 2014) with estimates ranging from 180-621 Gt C (Gorham, 1990; Yu et al., 2010; Yu, 2012).

The large quantity of C stored in peatlands, and the ability of peatlands to sequester more carbon, are at risk to environmental change. It is expected that peatlands

will have a positive feedback loop with environmental change, where warmer temperatures induce increased microbial decomposition and C release, with the potential to switch peatlands from C sinks to C sources (Hanson et al., 2020). Therefore, our ability to understand and simulate carbon dynamics in peatlands has implications for the global C cycle and predictions of future climatic conditions. Land surface models that represent peatland ecosystems and their C dynamics allow us to evaluate how changes in the peatland C cycle will influence atmospheric C concentrations in the future, however most global land surface C models don't represent peatlands (Tian et al., 2015). Improving the representation of peatlands in land surface models relies on data from experiments measuring components of the C cycle and environmental factors that influence C fluxes. The spruce and peatland responses under changing environments (SPRUCE, https://mnspruce.ornl.gov/) is one such experiment in northern Minnesota, USA, aimed at improving the representation of peatlands in the Energy Exascale Earth System Model (E3SM) land surface model (ELM).

The SPRUCE experiment uses whole-ecosystem warming and elevated CO_2 concentrations in ten open top enclosures to assess how peatlands will respond to environmental change (Hanson et al., 2017). In addition to advancing our understanding of peatland C dynamics, results from SPRUCE help to improve the simulation of the C cycle in ELM through data-driven calibrations and comparisons between observed and simulated C fluxes. A modified version of ELM was created in conjunction with SPRUCE (termed ELM_SPRUCE) to incorporate the hydrology and microtopography characteristic of bogs with perched water tables (Shi et al., 2015) and recently Shi et al. (*in review*) have developed a plant functional type (PFT) to represent the unique

physiology and hydrology of *Sphagnum* mosses. Simulations of the water table in ELM_SPRUCE compared well with observations (Shi et al., 2015), representing the first time, to our knowledge, a land surface model has included a fully prognostic calculation of water table level for a vegetated peatland that is independent of prescribed regional water tables. Further, Shi et al. (2015) represented the microtopography, or sub-grid topographic heterogeneity, characteristic of peatlands, which is known to influence peatland C cycling.

The influence of microtopography on peatland C fluxes is well documented in the literature (Moore and Knowles, 1989; Waddington and Roulet, 1996; Sullivan et al., 2008; Moore et al., 2011) and is largely driven by environmental gradients (e.g., soil moisture) that differ in their location in the peat column as a result of variation in depth to the water table. Peatland microtopography is often characterized by microforms: mound-like areas referred to as hummocks and depression-like areas referred to as hollows. Hummocks exhibit a larger distance from their surface to the water table compared to adjacent hollows, and CO_2 efflux linearly increases as the depth to water table increases in peatlands (Moore and Knowles, 1989). This generally translates to differences in respiration and net ecosystem exchange (NEE) between microforms (Waddington and Roulet, 1996; Sullivan et al., 2008). Due to the effect of soil moisture on microbial decomposition, CH_4 fluxes in hollows can be over 45 times higher than hummocks (Waddington and Roulet, 1996; Moore et al., 2011). Additionally, microtopography influences *Sphagnum* net primary production (NPP) which can constitute half of peatland C inputs (Szumigalski and Bayley, 1996; Rydin and Jeglum, 2013; Griffiths et al., 2017; Hanson et al., 2020). *Sphagnum* photosynthesis is affected by microtopography due to its

lack of vascular tissue, and thus depth to the water table modulates *Sphagnum* water content and photosynthesis (Rydin, 1985; Schipperges and Rydin, 1998; Walker et al., 2017). Because microtopography influences component C fluxes, microtopography plays a role in determining the NEE in peatlands.

The magnitude of NEE in peatlands is small compared to the component fluxes, with NEE two orders of magnitude smaller than H_R and NPP from the C budget estimate in Griffiths et al. (2017). The small magnitude of NEE compared to component fluxes (e.g., H_R & NPP) and their variability causes challenges for quantifying C budgets in peatlands (see Griffiths et al., 2017). This demonstrates that relatively small changes in measured or simulated component fluxes can have a relatively large effect on NEE, and highlights the need to accurately represent peatland microtopography in land surface models like ELM_SPRUCE.

ELM_SPRUCE uses a two column approach to represent microtopography, where one soil column represents hummocks and the other represents hollows. Lateral flow between the columns maintains the water table at similar absolute elevations. Other than their elevation and hydrology, the hummock and hollow soil columns are identical. ELM_SPRUCE uses three uncertain parameters to represent microtopography, which are hummock-hollow height differential (Δ_Z), hummock-hollow horizontal separation (H_S), and percent coverage of hollows ($Ho_{\%}$). This is similar to the approach used in the peatland carbon simulator (PCARS; Frolking et al., 2002), indicating that estimates of these parameters would be useful to multiple modeling efforts. Initially, ELM_SPRUCE parameters were determined heuristically using cursory survey data and expert opinion, and were set at: Δ_Z = 0.3m, H_s = 1.0m, and $Ho_{\%}$ = 25%. However, it is unknown how

well this parameterization matches field observations and how the uncertainty in these parameters influences the C cycle in ELM_SPRUCE. The initial heuristic parameterization of microtopography in ELM_SPRUCE is an indication of the lack of quantitative characterizations of microtopography in the literature, and highlights the need for methodologies that quantify microtopography and explicitly define microforms, which have only recently been developed (e.g., Lovitt et al., 2018; Stovall et al., 2019; Graham et al., 2020).

Sensitivity analyses (SA) are statistical approaches that quantify how uncertainty in the parameters of mathematical models propagate to uncertainty in model outputs, and thus helps determine which parameters are most influential for each model quantity of interest (QOI) representing a specific output. Polynomial chaos (PC) expansion is a popular technique used in global SA and uncertainty quantifications of computationally intensive models (Crestaux et al., 2009; Ricciuto et al., 2018). PC utilizes orthogonal polynomials to construct a surrogate model for each desired QOI in the computational model. Surrogate models emulate the behavior of QOIs within the range of parameter distributions, and Sobol sensitivity indices can be calculated from PC surrogate models. One of the major benefits of PC expansion is the ability to greatly reduce the number of model runs needed to calculate Sobol indices. The Sobol method (Sobol, 1993) is a variance-based decomposition approach to global SA that calculates indices related to first order, second order (interactions), and total sensitivity to uncertain parameters. Sobol indices represent the proportion of variation in the QOI that is incurred by variability in each parameter. Therefore, Sobol indices indicate how influential each parameter is in determining QOI variability.

In this study, we investigate how microtopography influences C cycling in ELM_SPRUCE, and which microtopographical parameters ($parameters_{Micro}$) the C cycle is most sensitive to. To accomplish this, we used high-resolution digital elevation models (DEMs) in SPRUCE plots to classify the surface into hummock and hollow microforms. Microform maps were then used to estimate $parameters_{Micro}$ in SPRUCE plots. Finally, these parameter estimates are used in a sensitivity analysis which evaluated how uncertainty in $parameters_{Micro}$ translated to uncertainty in simulated C fluxes in ELM_SPRUCE. The objectives of this study were to 1) quantify empirical estimates of ELM_SPRUCE $parameters_{Micro}$, 2) compare 'default' parameter values and the resulting model outputs (QOI_{Def}) to observed distributions and model outputs using observed means (QOI_{Rec}), 3) quantify the sensitivities of C fluxes and pools to $parameters_{Micro}$, and 4) quantify the variability in C flux QOIs resulting from allowing parameters to vary within observed ranges.

Methods

Study Site

ELM_SPRUCE parameter distributions were derived from DEMs representing the bog surface in 12 SPRUCE plots. The SPRUCE experiment is located at the S1-Bog in the Marcel Experimental Forest. This is a 890 ha experimental forest with a robust historical dataset comprising soil, hydrologic, nutrient, and climatic data, with hydrologic and climatic monitoring dating back to 1960. The S1-Bog is an 8.1ha ombrotrophic peat bog with a perched water table, with peat depths averaging 2.27m and peat as old as 11,100 cal BP (Slater et al., 2012; McFarlane et al., 2018). The S1-Bog exhibits hummock-hollow microtopography with elevation in SPRUCE plots ranging from -

0.48m - 0.31m relative to the plot mean elevation (Graham et al., 2020). Additional information on the Marcel Experimental Forest and S1-Bog can be found in Sebestyen et al. (2011).

Terrestrial Laser Scanning and Microform Classification

Terrestrial laser scanning (TLS) is a remote sensing technique that utilizes light detection and ranging (lidar) to measure the area surrounding the scanner, and represent it with a point cloud (Figure 1A). Point clouds are a digital representation of the scanned area, storing Cartesian coordinates (x,y,z) of scanned objects. Previous studies have demonstrated that TLS point clouds are able to generate accurate high-resolution DEMs of microtopography, and are thus well suited for classifying peatland microforms (Graham et al., 2019b, Graham et al. 2020; Stovall et al. 2019). In this study, point clouds derived from TLS within the 12 SPRUCE plots were used to generate DEMs of each SPRUCE plot, and DEMs were subsequently classified into hummock and hollow microforms to calculate parameters (Figure 3.1).

TLS scans were made with a Riegl VZ-1000 (1550 nm laser) in the spring (April-May) of each year from 2016-2019 from four locations on the interior boardwalk of each plot. The four scan positions per plot were co-registered into a single point cloud for each plot in each year (Graham et al., 2019a). TLS point clouds were used to generate DEMs of the bog surface within the interior boardwalk of SPRUCE plots with a mean absolute error of 0.057m based on 357 validation points (details on DEM production and accuracy can be found in Graham et al., 2019b and Graham et al., 2020). DEMs were classified into hummocks and hollows using the ELM_Classification method from Graham et al. (2020). This method classifies plot DEMs into hummock and hollow based on an

elevation threshold that is determined by the distribution of elevation in the plot. DEM grid cells were classified as hollows if its elevation was less than the plot elevation fifth percentile plus 0.1m:

$$\text{Eqn 3.1. } C_{ELM}(x,y) = \begin{cases} Hu, if\ Z_{xy} \geq (Z_{p5} + Tol) \\ Ho, if\ Z_{xy} < (Z_{p5} + Tol) \end{cases}$$

where $C_{ELM}(x,y)$ is the ELM_Classification at location xy, z_{p5} is the plot-specific elevation 5th percentile, and Tol is a tolerance of 0.1m (from Graham et al., 2020). The fifth percentile represents hollow bottoms and is used instead of the plot minimum to alleviate the effect of extremely low points. A tolerance of 0.1m was used because previous studies have found that *Sphagnum* species characteristic of hollows have optimal water content for photosynthesis when the water table is at a depth of 0.1m, and that methane production decreases substantially at this water table depth (Rydin, 1985; Schipperges and Rydin, 1998; Christensen et al., 2003). Therefore, if it is assumed that the water table is typically at or near the hollow surface, then this cutoff represents an important threshold for multiple C cycle processes. After performing this classification, DEMs are transformed into spatially explicit maps of hummock and hollow microforms (Figure 3.1D). These microform maps became the basis for parameters to use in ELM_SPRUCE.

Parameter Estimation

The microtopographical parameters of microform height difference Δ_Z, microform horizontal separation H_S, and microform percent cover $Ho_{\%}$ were calculated from microform maps in each of the twelve SPRUCE plots in each of the four years of the survey (n=48). Parameter estimates from microform maps were characterized and

compared to the 'default' ELM_SPRUCE parameter values to assess how well they represent empirical estimates.

The Δ_Z and $Ho_{\%}$ parameters were straightforward to estimate from microform maps. The Δ_Z parameter was calculated by subtracting the mean elevation of cells classified as hollow from the mean elevation of cells classified as hummock (Figure 3.1E). This value represents the distance between the average hollow elevation and the average hummock elevation. Percent cover of hollows was calculated as the percent of microform map cells that were classified as hollows in SPRUCE plots.

To estimate the H_S parameter, we used the distance transform described in Felzenszwalb and Huttenlocher (2012) implemented in Open Computer Vision (OpenCV) (Bradski, 2000). The distance transform is an algorithm that takes a binary image as input and calculates the euclidean distance from each 'on' pixel (1) to the nearest 'off' pixel (0). Pixels in the microform classification map with the value 1 represent hummocks and pixels with the value 0 represent hollows, and therefore the output is a map with pixel values representing the distance to the nearest hollow (0) pixel (Figure 3.1F). Hollow pixels have a distance of zero. To calculate the H_S estimate for a SPRUCE plot, we took the mean of the distance transform from that plot after masking hollow pixels.

Model Simulations

Sensitivity Analysis

A total of 3,000 ELM_SPRUCE simulations were used to perform the SA, with values for each run having parameters Δ_Z, H_s, and $Ho_{\%}$ set with random draws from a Gaussian joint probability density function constructed using means and standard

deviations from TLS data (Figure 2). We used the UQ Toolkit (Debusschere et al., 2015) to build polynomial chaos surrogate models and perform the SA. First order, second order, and total-effect Sobol indices were calculated for each uncertain parameter with respect to each QOI. The QOIs we chose to evaluate are C pools and fluxes that are likely influenced by microtopography, and which are listed in Table 3.1. All QOIs represent average values over the 2011-2018 period.

Model Runs

Transient simulations were performed from 1850-2018 using atmospheric CO_2 concentrations and N deposition in the nearest grid cell from a gridded dataset (Oleson et al., 2013) and continuously cycling the 2011-2018 site meteorology. Elevated CO_2 and warming associated with the experimental treatments are not considered in this study. To simulate strip cuts that occurred at the S1-Bog in 1974, 99% of aboveground tree biomass was removed in this year. Model QOIs were saved for each simulation to build QOI distributions and evaluate how influential microtopographical parameterization was for each QOI under ambient conditions. In addition to the ensemble of 3,000 simulations used in the sensitivity analysis, we performed one simulation using the default parameterization and one simulation using the observed mean parameter values, our 'recommended' parameterization.

QOI Variability

The influence of microtopographical parameterization on QOIs was assessed in three ways. First, to quantify uncertainty in QOIs resulting from parameter uncertainty, we divided the QOI range from the ensemble of 3,000 ELM_SPRUCE simulations by the

QOI value simulated using observed mean parameter values (Eqn 3.2), which we termed 'relative variation'.

$$\text{Eqn 3.2. Relative Variation} = \left(\frac{Max(QOI_{Ens}) - Min(QOI_{Ens})}{\text{QOI}_{\text{Rec}}}\right) * 100$$

Where QOI_{Ens} represents the 3,000 QOI values from the ensemble of 3,000 simulations, QOI_{Rec} is the QOI output when using the observed mean parameter values. Second, to quantify the effect of the default parameterization on QOIs we calculated the 'relative difference', calculated as the difference between QOIs using the default parameters and the recommended parameters divided by the QOI value from the recommended parameterization (Eqn 3.3).

$$\text{Eqn 3.3. Relative Difference} = \left(\frac{\text{QOI}_{\text{Rec}} - \text{QOI}_{\text{Def}}}{\text{QOI}_{\text{Rec}}}\right) * 100$$

Where QOI_{Def} is the QOI output when using the default parameterization. Finally, we correlated parameter values used in the ensemble of 3,000 ELM_SPRUCE simulations with the resulting QOI outputs. Considering that all of the variability in QOI is a result of varying $\text{parameters}_{\text{Micro}}$, it was expected that there would be significant correlations between $\text{parameters}_{\text{Micro}}$ and QOI. However, the strength of these relationships buttress the results of the sensitivity analysis, and the direction (+ or -) of these correlations provide the overarching influence of each parameter on QOIs. Further, plotting these correlations facilitates identification of non-linear relationships between parameters and QOIs.

Results

Parameter Distributions

The $Ho_{\%}$ parameter was the only parameter to have its default value within the observed range (Figure 2). The mean estimate of $Ho_{\%}$ from SPRUCE plots was 34.5% which was higher than the default value (25%), although the default value was within the observed range (23.3 - 45.0%). In contrast H_s and Δ_Z parameters were well outside observed ranges. The default value for Δ_Z (0.3m) was over twice the observed mean (0.13m), and the difference between maximum observed value and the default value (0.13m) was larger than the observed range of 0.06m (0.11-0.17m). Similarly, the mean estimate of H_s (0.43m) was less than half of the default value (1.0m), and the observed range (0.35-0.63m) was lower than the difference between the maximum estimate and the default value (0.37m). All combinations of parameters exhibited significant ($p < 0.001$) correlations (Figure 2). The strongest relationship (negative) was between Δ_Z and $Ho_{\%}$, which had a coefficient of determination (R^2) of 0.50. The weakest relationship (negative) was between H_s and $Ho_{\%}$ ($R^2 = 0.25$). There was a positive relationship between H_s and Δ_Z ($R^2 = 0.45$).

Parameter Sensitivities

There was a consistent pattern of QOIs being most sensitive to Δ_Z, followed by $Ho_{\%}$ and least sensitive to H_s (Figure 3.3). NEE was the exception, which was the most sensitive to $Ho_{\%}$. Sobol main effect indices for Δ_Z ranged from 0.030-0.341 (mean = 0.232), 0.006- 0.229 (mean = 0.084) for $Ho_{\%}$, and 0.002-0.023 (mean = 0.013) for H_s. The largest single sensitivity was total carbon in vegetation (TOTVEGC) to Δ_Z (main effect = 0.341). The generally low main effect indices indicate that interactions between

$parameters_{Micro}$ were important for most QOIs (Figure 4). As with main-effects, sensitivities to interactions including Δ_Z were the largest. The sensitivity of NEE to individual parameters was much lower than NEE sensitivity to interactions.

QOI Variability

Relative variation in QOIs ranged from 4.11% (CH4_Flux) to 26.9% (NEE) with a mean of 10.9% (Figure 5). Relative differences resulting from the use of default parameter values compared to the recommended parameter values ranged from -27.6% (NPP_Sphag) to 8.4% (NEE) and had a mean of -5.4%. NEE was the only QOI in which QOI_{Def} fell within the range of QOI_{Ens}. As would be expected, all $parameters_{Micro}$ were significantly ($p < 0.001$) correlated with all QOIs (Figure 6), though the strength of the correlation was highly variable. Further, the strength of some correlations are due to the fact that parameters are correlated with each other, and parameter combinations were drawn from a joint distribution. The strongest correlation was between Δ_Z and TOTVEGC ($R^2 = 0.77$), which exhibited a positive correlation. Other strong correlations (i.e., $R^2 > 0.6$) were between Δ_Z and HR (negative; $R^2 = 0.69$), TOTVEGC and $Ho_{\%}$ ($R^2 = 0.66$), and Δ_Z and NPP_Sphag (negative; $R^2 = 0.70$).

Discussion

To our knowledge, this study is the first to provide calculations of $parameters_{Micro}$ used in land surface models and models that simulate peatland C dynamics directly from observed data. We found that the default values used for parameters Δ_Z and H_S in ELM_SPRUCE were well outside of the observed ranges, which caused $QOIs_{Def}$, with the exception of NEE_{Def}, to fall outside the range of $QOIs_{Ens}$. For both Δ_Z and H_s, the default values were just over twice the observed mean. We initially calculated H_S using

the range parameter of modeled semivariograms, which represents the distance at which elevation is no longer auto-correlated, and when fit to a sine wave (as microtopography is often conceptualized) the range parameter corresponds to the peak-to-trough distance, and therefore representative of the maximum separation. When we calculated H_S using semivariogram ranges, the mean was 1.5m (range = 0.9-2.6m). Interestingly, these estimates were much closer to the default value of H_S (1.0m) and may indicate that the reason for the high default value was because H_S was initially conceptualized as a peak-to-trough distance (sine wave) and might better represent the maximum hummock-hollow spacing, rather than the mean. In contrast, the distance transform we used enables the explicit calculation of the mean distance from each hummock cell to the nearest hollow from classification maps.

Similarly, the default Δ_Z better represents the distance from the top of the hummock to the bottom of hollows in our data, rather than the mean difference between areas classified as each microform. This is corroborated by elevation distributions from DEMs, in which the difference between the 95th and 5th quantile of elevation is on average 0.26m (range = 0.21-0.39m), and indicates that the default Δ_Z value (0.3m) represents the typical peak-to-trough relief of microtopography. Only recently have quantitative microform classification schemes been developed, and maps of microform classifications that facilitated the direct calculation of parameters in this study were not available at the time ELM_SPRUCE was created, which highlights the importance of studies mapping microforms using DEMs (e.g., Lovitt et al., 2018; Stovall et al., 2019; Graham et al., 2020).

Two of the three parameters$_{Micro}$ used in ELM_SPRUCE (Δ_Z and $Ho_{\%}$) are also used in the Peatland Carbon Simulator (PCARS) (Frolking et al., 2002). The PCARS model simulates the C balance of a peatland, with representation of processes including photosynthesis, autotrophic respiration, vegetation phenology, and aerobic and anaerobic decomposition. Therefore, the parameter$_{Micro}$ distributions and recommended (mean) values reported here could be used to parameterize the PCARS model. Further, the methodology we used for producing microform classifications from Graham et al. (2020) and the methods for estimating parameter values in this study can be used to calculate parameters$_{Micro}$, which would provide insight into inter-peatland variation in these parameters that is valuable for users of both models.

In our ensemble of 3,000 ELM_SPRUCE simulations, CH_4 flux had a negative relationship with Δ_Z and a positive relationship with $Ho_{\%}$, which is consistent with experimental studies. Previous studies collecting empirical data have demonstrated that hollows have larger CH_4 fluxes compared to hummocks (Bubier et al., 1993; Waddington and Roulet, 1996) due to the greater prevalence of anaerobic conditions, which leads to greater CH_4 production (Bubier et al., 1993). Further, larger Δ_Z values result in a larger fraction of the peat column existing in aerobic conditions that facilitate methanotrophy. Our sensitivity analyses found that CH_4 flux was most sensitive to Δ_Z and that Δ_Z had the strongest correlation with CH_4 flux, which is contrary to what would be expected based on results from Bubier et al. (1993). Bubier et al. (1993) found that the primary driver of higher CH_4 emissions from hollows was higher rates of production from methanogens, and that methanotrophy in the hummock peat column was a secondary control. This would indicate that $Ho_{\%}$ would have a larger influence on CH_4 flux than Δ_Z. The reason

for this discrepancy is unclear, but may be related to the fact that areal coverage of hummocks is about twice that of hollows.

The strong negative correlation between Δ_Z and H_R is somewhat unanticipated, as one would expect that H_R would increase as the fraction of the peat profile of hummocks in aerobic conditions increases. Field and laboratory studies have demonstrated that CO_2 efflux increases as the depth to water table increases (Moore and Knowles, 1989; Bubier et al., 2003; Sullivan et al., 2008). Therefore, it is intuitive that there would be a positive correlation between H_R and Δ_Z. The reason we did not observe this relationship is likely due to an overall reduction in NPP, shifts in C storage in vegetation, and PFT-specific shifts in NPP (Figure 7).

As Δ_Z increased, we found divergent responses in PFT-specific NPP. The PFT representing black spruce and shrubs increased while NPP in the *Sphagnum* PFT decreased. This is consistent with experimental studies that observed increased black spruce growth and decreased *Sphagnum* growth with a deeper water table (Lieffers and Rothwell, 1987; Lieffers and Macdonald, 1989; Weltzin et al., 2001; Norby et al., 2019), which occurs in the hummock column when Δ_Z is increased. Increasing NPP in black spruce and shrub PFTs explain the strong increase in the C content of vegetative biomass. Further, reductions in *Sphagnum* NPP (and overall NPP) caused modest reductions in the C content of soil organic matter, as *Sphagnum* is responsible for ~50% of peatland C inputs (Szumigalski and Bayley, 1996; Rydin and Jeglum, 2013; Griffiths et al., 2017; Hanson et al., 2020). The amalgamation of these responses to increasing Δ_Z was a slightly stronger C sink (more negative NEE) and higher total ecosystem C content (Figure 7). Increases in ecosystem C and the strength of the C sink are largely due to increases in

tree biomass that are enhanced due to tree regeneration following the strip cut. Therefore, these increases would likely be subtler for undisturbed wooded peatlands.

Summary

Data and results from this study provide $parameters_{Micro}$ distributions that are useful for multiple models which simulate peatland C dynamics, and yield insight into how these parameters influence different components of the C cycle. The relationships we observed between CH_4 flux and $parameters_{Micro}$ aligned with previous field and laboratory studies. We also observed interesting shifts in productivity between plant functional types as a result of increasing Δ_Z that were corroborated by experimental studies, and translated to shifts in the C stored in vegetative biomass and soil organic matter. The influence of any single parameter on the overall C budget (NEE) was relatively small, but there were strong interactions between $parameters_{Micro}$ that resulted in large relative variations of NEE. Constraining $parameters_{Micro}$ will reduce uncertainty in modeled NEE and help elucidate what level of warming will switch the system from C sink to C source, as indicated by results from Hanson et al. (2020). This study demonstrates the importance of how microtopography is parameterized in land surface models on both C fluxes and pools, and field based estimates of $parameters_{Micro}$ are needed to constrain these parameters to observed values. A logical extension of this work would be exploring the capability of airborne and satellite sensors to detect and characterize microtopography across larger geographic extents, which would enable the calculation of $parameters_{Micro}$ in different regions and across multiple peatland types.

Acknowledgements

This material is based upon work supported by the U.S. Department of Energy, Office of Science, Office of Biological and Environmental Research. Jake Graham was supported under a contract between Oak Ridge National Laboratory and Boise State University (#4000145196) with funding for the SPRUCE project from the U.S. Department of Energy (DOE), Office of Science, Office of Biological and Environmental Research. Oak Ridge National Laboratory is managed by UT-Battelle, LLC, for DOE under contract DE-AC05-00OR22725. Additional funding was provided by the Department of Geosciences, Boise State University.

This research used resources of the Compute and Data Environment for Science (CADES) at the Oak Ridge National Laboratory, which is supported by the Office of Science of the U.S. Department of Energy under Contract No. DE-AC05-00OR22725. Data sets pertaining to this study are in the online project archive at http://mnspruce.ornl.gov and for long-term storage in the U.S. Department of Energy's (DOE) Environmental Systems Science Data Infrastructure for a Virtual Ecosystem (ESS-DIVE; http://ess-dive.lbl.gov/)

Table 3.1. Quantities of interest (QOI) from the ELM_SPRUCE model related to the C cycle that were evaluated in the sensitivity analysis.

QOI	Description	Units
HR	Heterotrophic respiration	gC m^{-2} yr^{-1}
NPP	Net primary production	gC m^{-2} yr^{-1}
NPP_Sphag	NPP of the *Sphagnum* PFT	gC m^{-2} yr^{-1}
TOTVEGC	Total C in vegetation	gC m^{-2}
NEE	Net ecosystem exchange*	gC m^{-2} yr^{-1}
CH4_NET_FLUX	Methane flux*	mol m^{-2} yr^{-1}

* Negative values = atmosphere to land; positive = atmosphere to land

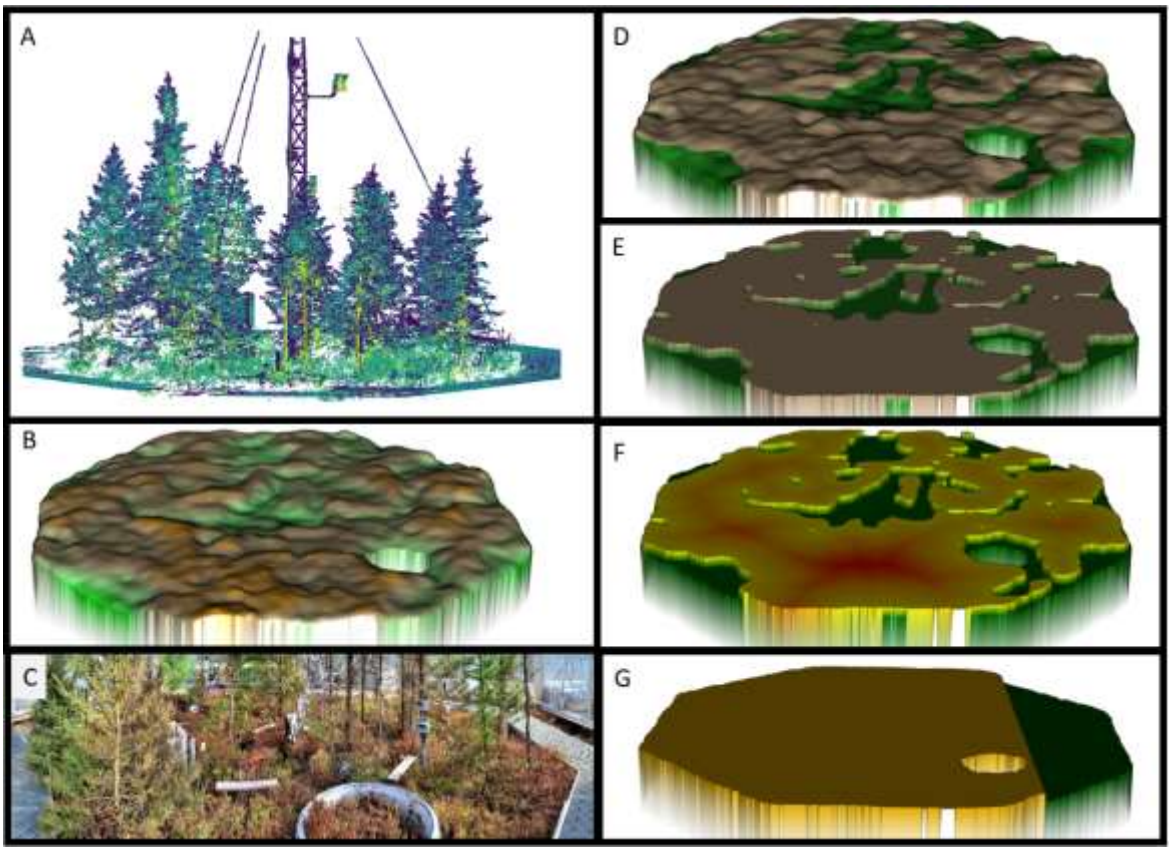

Figure 3.1. Diagram showing the workflow for creating digital elevation models (DEM) (B) from terrestrial laser scanning point clouds (A) representing the interior of a SPRUCE plot (C). The DEM was classified into hummock (tan) and hollow (green) microforms (D), from which hollow percent cover ($Ho_{\%}$) and microform height difference (Δz) were calculated. Panel E displays the microform map generalized to display hummocks with elevations represented by Δz. A map of the distance transform (F) used to calculate microform horizontal separation (H_s), with yellow representing short distances and red representing longer distances to the nearest hollow. A map of microtopography within the SPRUCE plot displayed as it is represented in ELM_SPRUCE (G), with the two colors representing hummock (gold) and hollow (green) soil columns, and the proportion of green area representing $Ho_{\%}$. The gold color of hummocks represents the average distance to the nearest hollow (from E), and Δz displayed as the difference between soil column elevations.

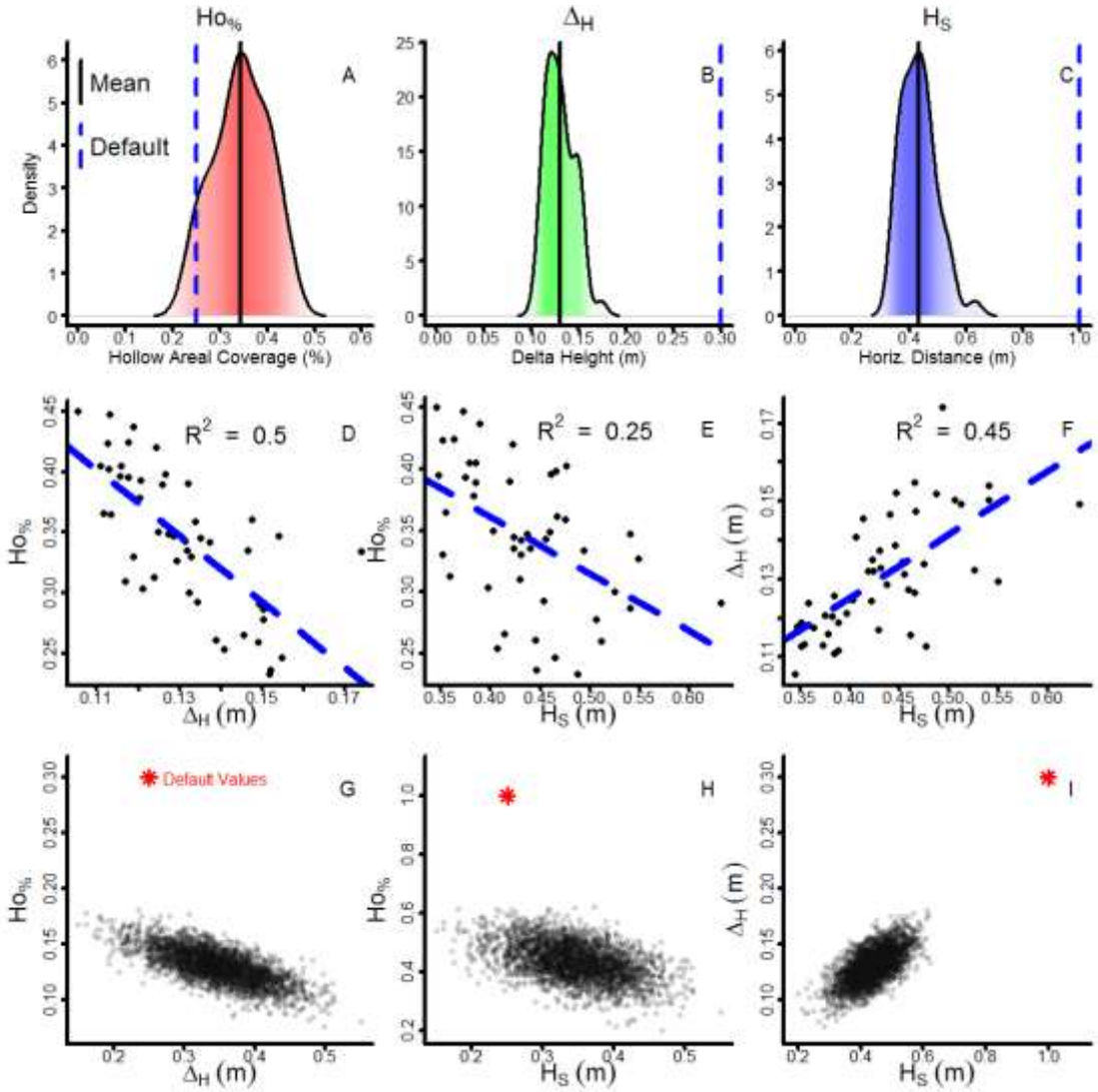

Figure 3.2. Distributions of ELM_SPRUCE microtopographical parameters estimated from SPRUCE plot DEMs, also displaying the observed means and 'default' parameter values as vertical lines (A,B,C). Plots showing the correlations between ELM_SPRUCE microtopographical parameters with lines displaying linear models (D,E,F). All correlations were significant ($p < 0.001$). Parameter samples drawn from a joint probability density function used in the ensemble of 3,000 ELM_SPRUCE simulations used for the sensitivity analysis, default parameter values are displayed with red stars (G,H,I).

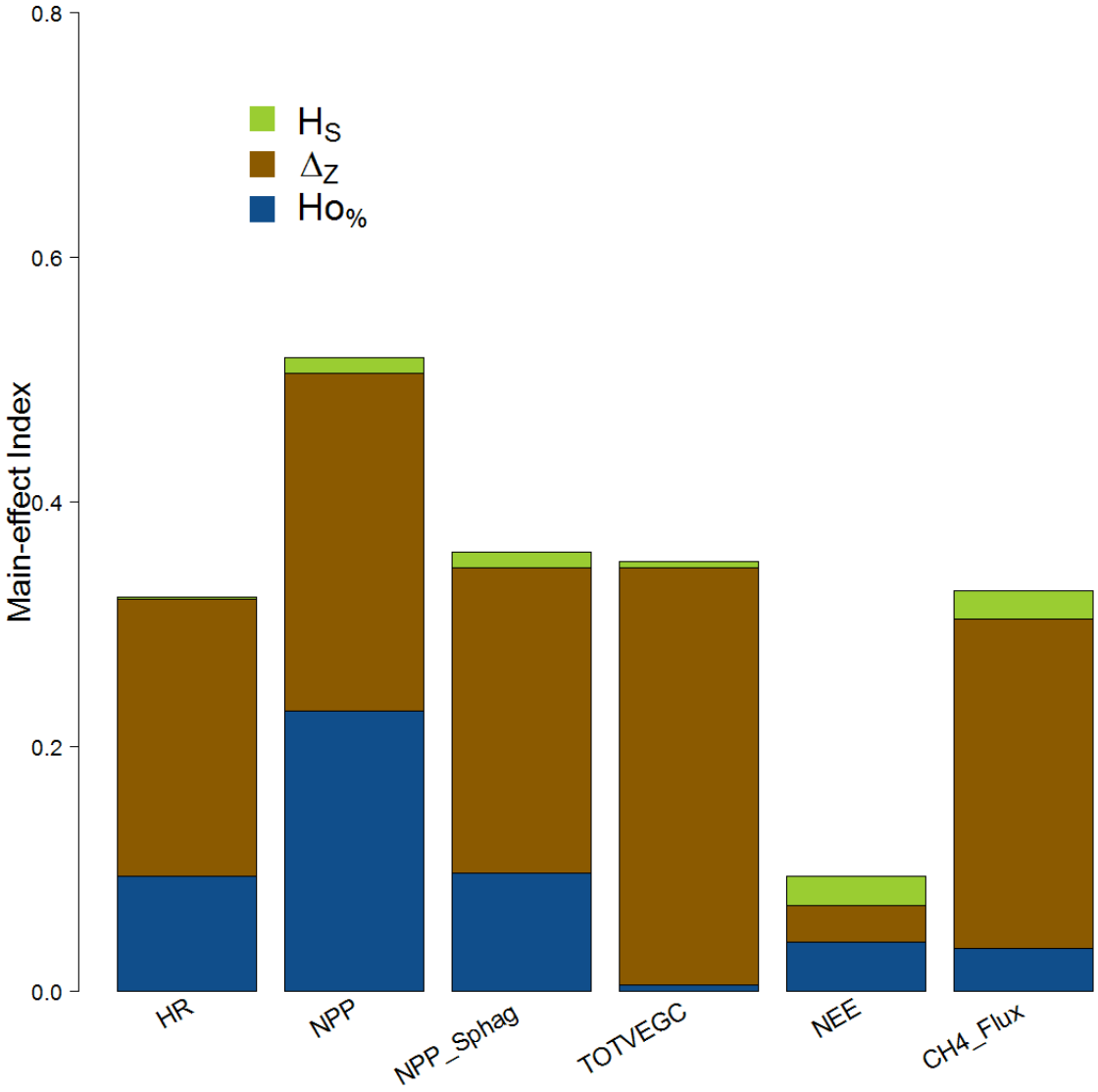

Figure 3.3. Sobol main-effect indices for quantities of interest: heterotrophic respiration (HR), net primary production (NPP), net primary production of the *Sphagnum* plant functional type (NPP_Sphag), total carbon in vegetation (TOTVEGC), net ecosystem exchange (NEE), and methane flux (CH4_Flux). Sobol sensitivity indices were calculated from an ensemble of 3,000 ELM_SPRUCE simulations using random parameter combinations drawn from a joint probability distribution.

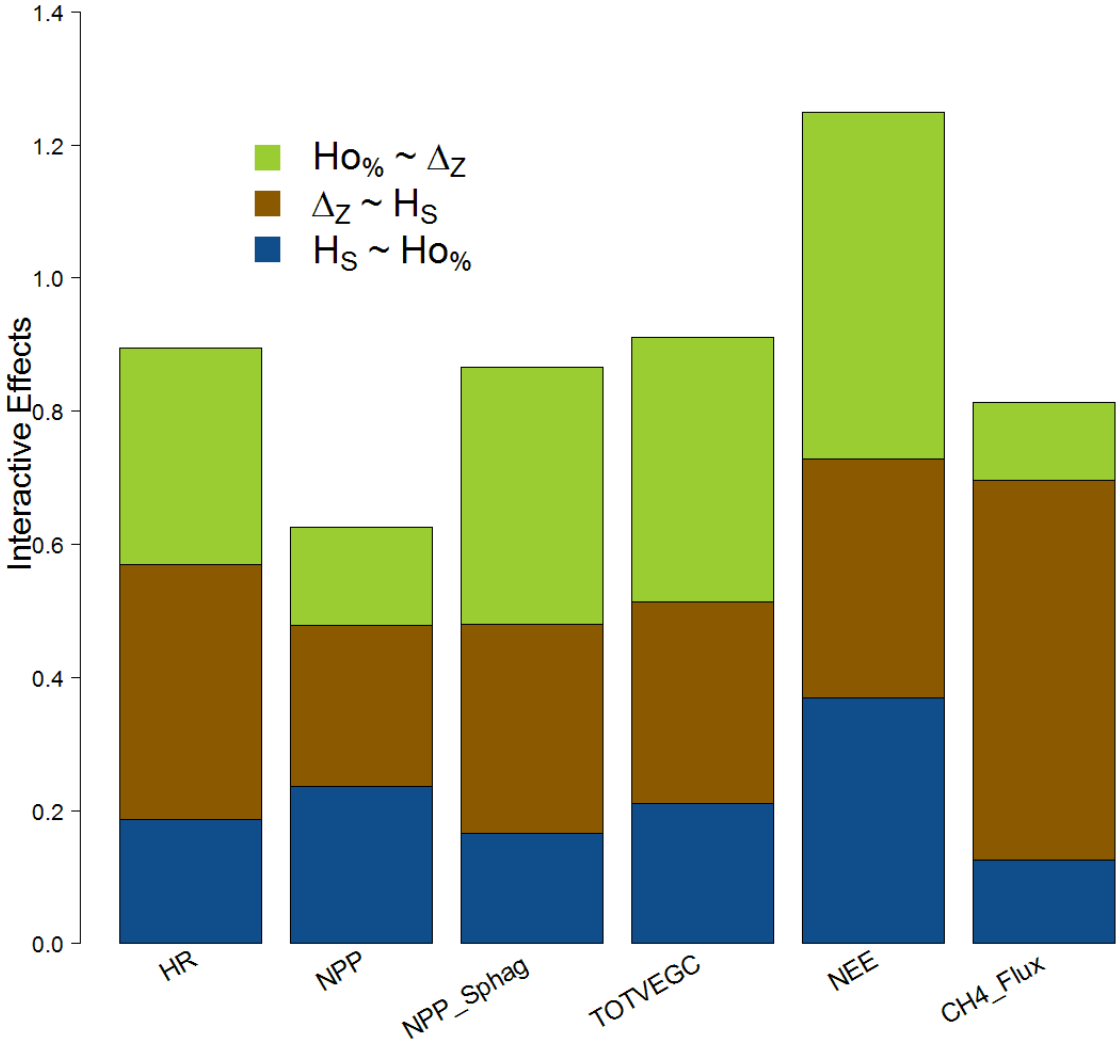

Figure 3.4. Sobol second-order indices (interactive terms) for quantities of interest: heterotrophic respiration (HR), net primary production (NPP), net primary production of the *Sphagnum* plant functional type (NPP_Sphag), total carbon in vegetation (TOTVEGC), net ecosystem exchange (NEE), and methane flux (CH4_Flux). Sobol sensitivity indices were calculated from an ensemble of 3,000 ELM_SPRUCE simulations using random parameter combinations drawn from a joint probability distribution.

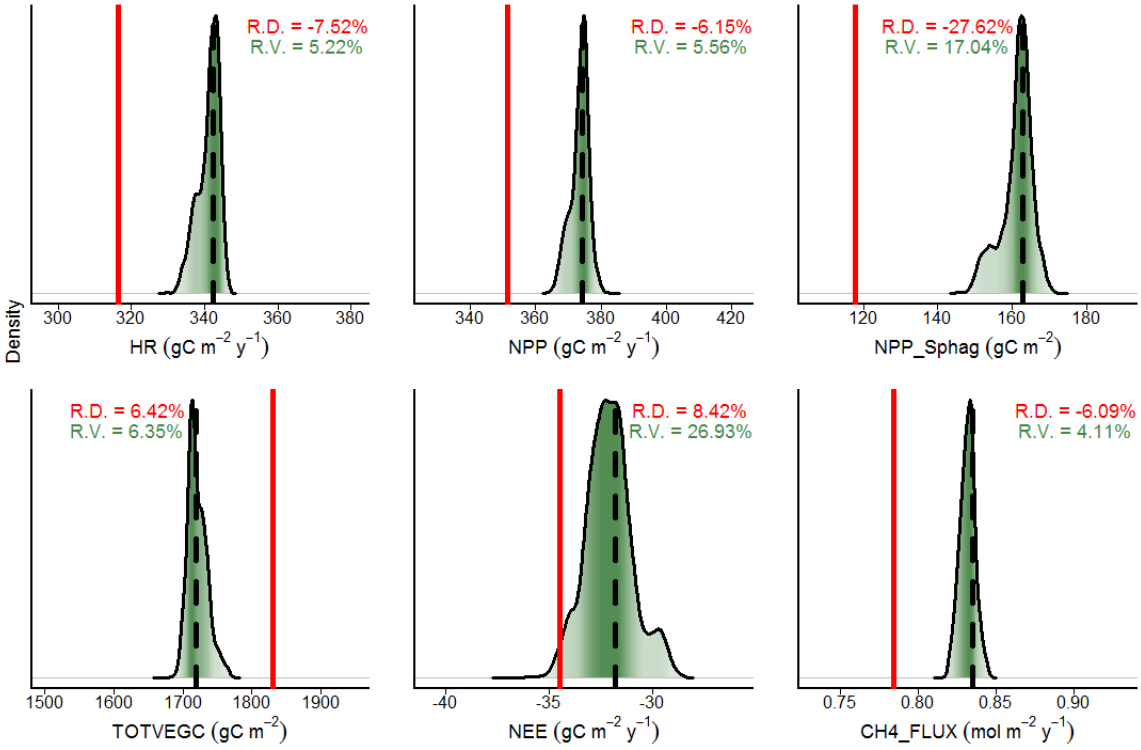

Figure 3.5. Distributions of ELM_SPRUCE carbon model outputs showing the variation in model outputs resulting from allowing microtopographical parameters to vary randomly in 3,000 simulations. Additionally, red vertical lines display the model output value when using the 'default' parameter values and dashed vertical black lines represent model outputs when using the observed mean parameter values (i.e., 'Recommended') from SPRUCE plots. R.D. is relative difference and R.V. is relative variation. Quantities of interest: heterotrophic respiration (H_R), net primary production (NPP), net primary production of the *Sphagnum* PFT (NPP_Sphag), total carbon in vegetation (TOTVEGC), net ecosystem exchange (NEE), and methane flux (CH4_Flux).

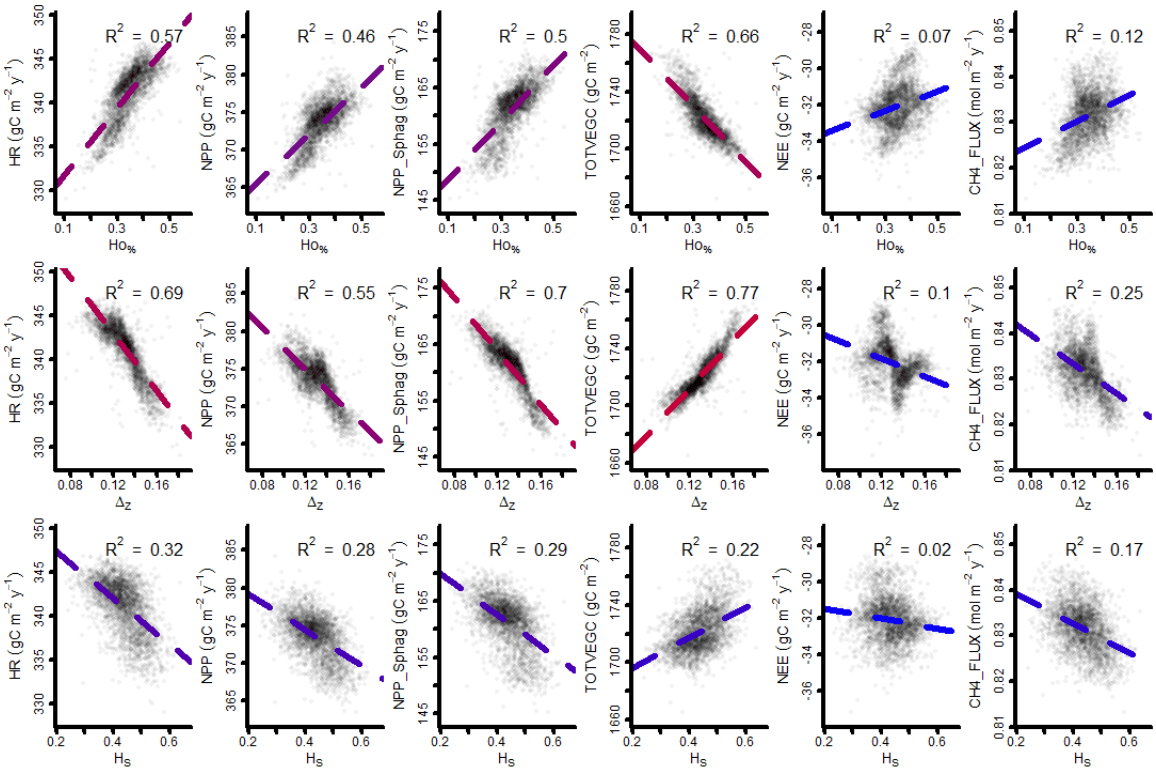

Figure 3.6. Correlations between microtopographical parameters and ELM_SPRUCE carbon related quantities of interest. All correlations were highly significant ($p < 0.001$), regression lines are colored by the coefficient of determination (R^2), with low R^2 in blue and high in red. Quantities of interest: heterotrophic respiration (HR), net primary production (NPP), net primary production of the *Sphagnum* PFT (NPP_Sphag), total carbon in vegetation (TOTVEGC), net ecosystem exchange (NEE), and methane flux (CH4_Flux).

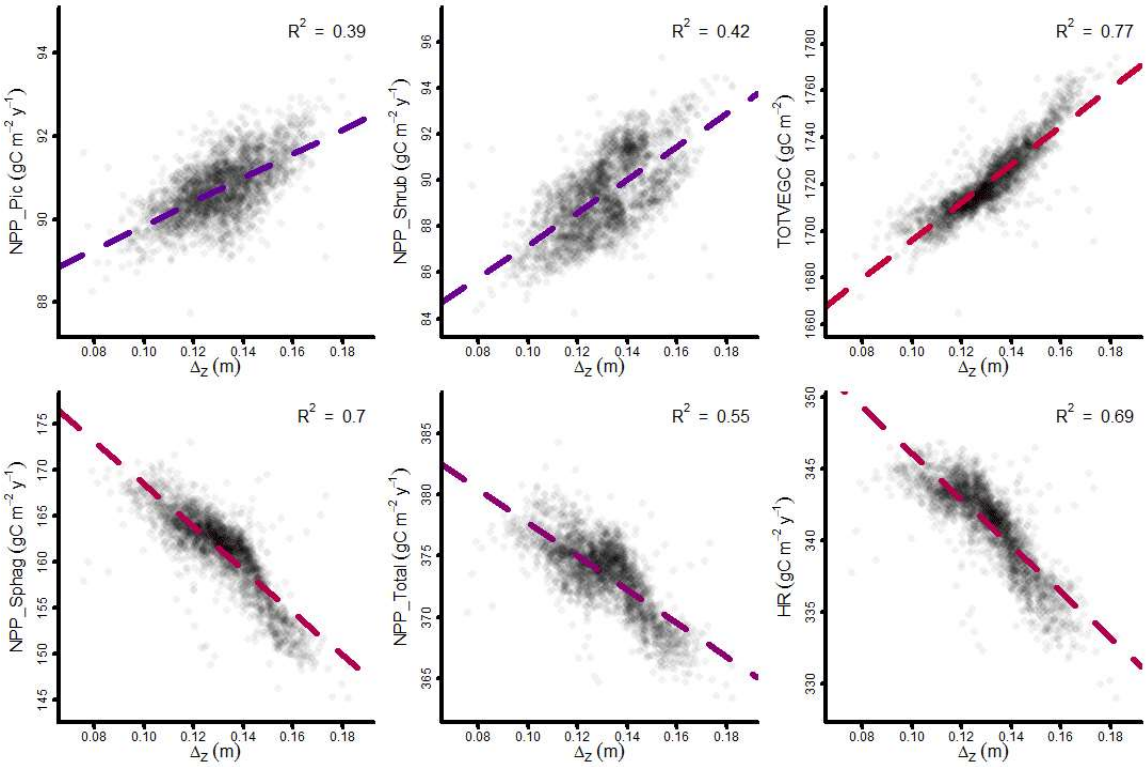

Figure 3.7. Correlations between Δz and selected ELM_SPRUCE carbon pools and fluxes, showing PFT-specific NPP responses and associated shifts in the vegetation carbon pool and heterotrophic respiration. All correlations were highly significant ($p < 0.001$), regression lines are colored by the coefficient of determination (R^2), with low R^2 in blue and high in red. Quantities of interest: net primary production (NPP), black spruce PFT net primary production (NPP_Pic), shrub PFT net primary production (NPP_Shrub), *Sphagnum* PFT net primary production (NPP_Sphag), total carbon in vegetation (TOTVEGC), net ecosystem exchange (NEE), and heterotrophic respiration (HR).

References

Bradski, G. 2000. The opencv library. Dr. Dobb's Journal of Software Tools.

Bubier, J., A. Costello, T. R. Moore, N. T. Roulet, and K. Savage. 1993. Microtopography and methane flux in boreal peatlands, northern Ontario, Canada. Canadian Journal of Botany, 71:1056-1063.

Bubier, J. L., G. Bhatia, T. R. Moore, N. T. Roulet, and P. M. Lafleur. 2003. Spatial and temporal variability in growing-season net ecosystem carbon dioxide exchange at a large peatland in Ontario, Canada. Ecosystems 6:353-367.

Cao, M., and F. I. Woodward. 1998. Net primary and ecosystem production and carbon stocks of terrestrial ecosystems and their responses to climate change. Global Change Biology 4:185-198.

Christensen, T. R., A. Ekberg, L. Strom, M. Mastepanov, N. Panikov, M. Oquist, B. H. Svensson, H. Nykanen, P. J. Martikainen, and H. Oskarsson. 2003. Factors controlling large scale variations in methane emissions from wetlands. Geophysical Research Letters 30:1414–1417.

Crestaux, T., O. L. Maitre, and J. M. Martinez. 2009. Polynomial chaos expansion for sensitivity analysis. Reliability Engineering and System Safety 94:1161-1172.

Debusschere, B., K. Sargsyan, C. Safta, and K. Chowdhary. 2015. UQ Toolkit.

Felzenszwalb, P. F., and D. P. Huttenlocher. 2012. Distance Transforms of Sampled Functions. Theory of Computing 8:415-428.

Frolking, S., N. T. Roulet, T. R. Moore, P. M. Lafleur, J. L. Bubier, and P. M. Crill. 2002. Modeling seasonal to annual carbon balance of Mer Bleue Bog, Ontario, Canada. Global Biogeochemical Cycles 16:1–21, doi:10.1029/2001GB001457

Gorham, E. 1990. Biotic impoverishment in northern peatlands. Woodwell GM, editor. The earth in transition: patterns and processes of biotic impoverishment. New York: Cambridge University Press New York. p65-98.

Graham, J. D., N. F. Glenn, and L. P. Spaete. 2019a. SPRUCE terrestrial laser scanning of experimental plots beginning in 2015. Oak Ridge National Laboratory, TES SFA, U.S. Department of Energy, Oak Ridge, Tennessee, U.S.A. https://doi.org/10.25581/spruce.067/1515552

Graham, J. D., N. F. Glenn, and L. P. Spaete. 2019b. SPRUCE microtopography of experimental plots derived from terrestrial laser scans beginning in 2016. Oak Ridge National Laboratory, TES SFA, U.S. Department of Energy, Oak Ridge, Tennessee, U.S.A. https://doi.org/10.25581/spruce.068/1515553

Graham, J. D., N. F. Glenn, L. P. Spaete, and P. J. Hanson. 2020. Characterizing Peatland Microtopography Using Gradient and Microform-Based Approaches. Ecosystems, 1-17.

Griffiths, N. A., P. J. Hanson, D. M. Ricciuto, C. M. Iverson, A. M. Jensen, A. Malhotra, K. J. McFarlane, R. J. Norby, K. Sargsyan, S. D. Sebestyen, X. Shi, A. P. Walker, E. J. Ward, J. M. Warren, and D. J. Weston. 2017. Temporal and spatial variation in peatland carbon cycling and implications for interpreting response of an ecosystem-scale warming experiment. Soil Science Society of America Journal 81:1668-1688.

Hanson, P. J., N. A. Griffiths, C. M. Iversen, R. J. Norby, S. D. Sebestyen, J. R. Phillips, J. P. Chanton, R. K. Kolka, A. Malhotra, K. C. Oleheiser, J. M. Warren, X. Shi, X. Yang, J. Mao, D. and M. Ricciuto. 2020. Rapid net carbon loss from a whole-ecosystem warmed peatland. AGU Advances doi: 10.1029/2020AV000163.

Hanson, P. J., J. S. Riggs, W. R. Nettles, J. R. Phillips, M. B. Krassovski, L. A. Hook, L. Gu, A. D. Richardson, D. M. Aubrecht, D. M. Ricciuto, J. M. Warren, and C. Barbier. 2017. Attaining whole-ecosystem warming using air and deep soil heating methods with an elevated CO_2 atmosphere. Biogeosciences 14:861–883, doi: 10.5194/bg-14-861-2017.

Lieffers, V. J., and S. E. MacDonald. 1989. Growth and foliar nutrient status of black spruce and tamarack in relation to depth of water table in some Alberta peatlands. Canadian Journal of Forest Research 20:805-809.

Lieffers, V. J., and R. L. Rothwell. 1987. Rooting of peatland black spruce and tamarack in relation to depth of water table. Canadian Journal of Botany 65:817-821.

Lovitt, J., M. M. Rahman, S. Saraswati, G. J. McDermid, M. Strack, and B. Xu. 2018. UAV remote sensing can reveal the effect of lowimpact seismic lines on surface morphology, hydrology, and methane (CH4) release in a boreal treed bog. Biogeosciences 123:1117–29.

McFarlane, K. J., P. J. Hanson, C. M. Iversen, J. R. Phillips, and D. J. Brice. 2018. Local spatial heterogeneity of Holocene carbon accumulation throughout the peat profile of an ombrotrophic Northern Minnesota bog. Radiocarbon 60:941–962.

Moore, T. R., A. De Young, J. L. Bubier, E. R. Humphreys, P. M. Lafleur, and N. T. Roulet. 2011. A multi-year record of methane flux at the Mer Bleue Bog, southern Canada. Ecosystems 14:646-567.

Moore, T. R., and R. Knowles. 1989. The influence of water table levels on methane and carbon dioxide emissions from peatland soils. Canadian Journal of Soil Sciences 69:33-38.

Morris, P. J., G. T. Swindles, P. J. Valdes, R. F. Ivanovic, L. J. Gregoire, M. W. Smith, L. Tarasov, A. M. Haywood, and K. L. Bacon. 2018. Global peatland initiation driven by regionally asynchronous warming. PNAS 115:4851-4856.

Norby, R. J., J. Childs, P. J. Hanson, and J. M. Warren. 2019. Rapid loss of an ecosystem engineer: Sphagnum decline in an experimentally warmed bog. Ecology and Evolution 9:12571-12585.

Oleson, K. W., D. M. Lawrence, G. B. Bonan, B. Drewniak, M. Huang, C. D. Koven et al. 2013. Technical description of version 4.5 of the Community Land Model (CLM). NCAR Technical Note NCAR/TN-503+STR.National Center for Atmospheric Research, Boulder, CO.

Ricciuto, D., K. Sargsyan, and P. Thornton. 2018. The impacts of parametric uncertainties on biogeochemistry in E3SM land model. Journal of Advances in Modeling Earth Systems 10.

Rydin, H. 1985. Effect of water level on desiccation of Sphagnum in relation to surrounding Sphagna. OIKOS 45:374-379.

Rydin, H., and J. K. Jeglum. 2013. The Biology of Peatlands, the Biology of Habitats Series, 2nd edn., Oxford Univ. Press, Oxford.

Scharlemann, P. W., E. V. J. Tanner, R. Hiederer, and V. Kapos. 2014. Global soil carbon: understanding and managing the largest terrestrial carbon pool. Carbon Management 5:81-91. https://doi.org/10.4155/cmt.13.77

Schipperges, B., and H. Rydin. 1998. Response of photosynthesis of *Sphagnum* species from contrasting microhabitats to tissue water content and repeated desiccation. New Phytologist 140:677-684.

Shi, X., D. M. Ricciuto, P. E. Thornton, X. Xu, F. Yuan, R. J. Norby, A. P. Walker, J. Warren, J. Mao, P. J. Hanson, L. Meng, D. Weston, and N. A. Griffiths. *In review, 202*. Modeling the hydrology and physiology of Sphagnum moss in a northern temperate bog. Biogeosciences Discussions https://doi.org/10.5194/bg-2020-90

Shi, X., P. E. Thornton, D. M. Ricciuto, P. J. Hanson, J. Mao, S. D. Sebestyen, N. A. Griffiths, and G. Bisht. 2015. Representing northern peatland microtopography and hydrology within the Community Land Model. Biogeosciences 12:6463–6477.

Slater, L., P. J. Hanson, and L. A. Hook. 2012. SPRUCE S1 Bog Peat Depth Determined by Push Probe and GPR: 2009–2010. Oak Ridge National Laboratory, TES SFA, U.S. Department of Energy, Oak Ridge, Tennessee, U.S.A. https://doi.org/10.3334/CDIAC/spruce.002.

Sobol, I. M. 1993. Sensitivity estimates for nonlinear mathematical models. Mathematical Modelling and Computational Experiments 1:407-414.

Stovall, A. E. L., J. S. Diamond, R. A. Slesak, D. L. McLaughlin, and H. Shugart. 2019. Quantifying wetland microtopography with terrestrial laser scanning. Remote Sensing of Environment 232:111271.

Sullivan, P. F., S. J. T. Arens, R. A. Chimner, and J. M. Welker. 2008. Temperature and microtopography interact to control carbon cycling in a high arctic fen. Ecosystems 11:61-76.

Szumigalski, A. R., and S. E. Bayley. 1996. Net above-ground net primary production along a bog-rich fen gradient in central Alberta, Canada. Wetlands 16:467-476.

Tian, H., C. Lu, J. Yang, K. Banger, D. N. Huntzinger, C. R. Schwalm, A. M. Michalak, R. Cook, P. Ciais, D. Hayes, M. Huang, A. Ito, A. K. Jain, H. Lei, J. Mao, S. Pan, W. M. Post, S. Peng, B. Poulter, W. Ren, D. Ricciuto, K. Schaefer, X. Shi, B. Tao, W. Wang, Y. Wei, Q. Yang. B. Zhang, and N. Zeng. 2015. Global patterns and controls of soil organic carbon dynamics as simulated by multiple terrestrial biosphere models: Current status and future directions. Global Biogeochemical Cycles 29:775-792. doi:10.1002/2014GB005021.

Waddington, J. M., and N. T. Roulet. 1996. Atmosphere-wetland carbon exchanges: Scale dependency of CO_2 and CH_4 exchange on the developmental topography of a peatland. Global Biogeochemical Cycles 10:233-245.

Walker, A. P., K. R. Carter, L. Gu, P. J. Hanson, A. Malhotra, R. J. Norby, S. D. Sebestyen, S. D. Wullschleger, and D. J. Weston. 2017. Biophysical drivers of seasonal variability in *Sphagnum* gross primary production in a northern temperate bog. Journal of Geophysical Research: Biogeosciences 122:1078-1097. doi:10.1002/2016JG003711.

Weltzin, J. F., C. Harth, S. D. Bridgham, J. Pastor, and M. Vonderharr. 2001. Production and microtopography of bog bryophytes: response to warming and water-table manipulations. Oecologia 128:557-565.

Yu, Z. 2011. Holocene carbon flux histories of the world's peatlands: global carbon-cycle implications. The Holocene 21:761-774.

Yu, Z. 2012. Northern peatland carbon stocks and dynamics: a review. Biogeosciences 9:4071-4085.

Yu, Z., D. W. Beilman, S. Frolking, G. M. MacDonald, N. T. Roulet, P. Camill, and D. J. Charman DJ. 2011. Peatlands and their role in the global carbon cycle. EOS 92:97-108

CHAPTER FOUR: *PICEA MARIANA* AND *LARIX LARICINA* GROWTH RESPONSES TO ELEVATED TEMPERATURE AND CO_2: A FOUR YEAR SYNTHESIS FROM THE SPRUCE EXPERIMENT

Abstract

Picea mariana and *Larix laricina* are widely distributed across the North American boreal region, including peatlands, and are thus significant mediators of biogeochemical, hydrological and energy exchanges with the atmosphere. Climate warming is expected to occur faster in the high latitudes, which will extend the growing season and is hypothesized to disproportionately impact tree growth in the boreal region. Peatlands store up to one third of global terrestrial carbon. Therefore, understanding how these tree species will respond to warming and atmospheric change is important for estimating the carbon balance of these northern ecosystems. The Spruce and Peatland Responses Under Changing Environments (SPRUCE) experiment uses whole-ecosystem warming up to +9°C with and without elevated CO_2 (+500 ppm) to evaluate how a peatland ecosystem responds to a range of warming and elevated CO_2 treatments. Here I report on SPRUCE *Picea* and *Larix* growth response after four years of SPRUCE treatments. I assessed the effect of SPRUCE treatments on 1) tree height, 2) canopy volume, 3) basal area, and 4) tree mass change. *Picea* mass showed a negative response to temperature initially, but the response weakened over time. Conversely, *Larix* mass showed no temperature response

initially, but developed a positive relationship over time. The divergent species-specific trends resulted in no detection of a temperature response at the community level. *Picea* height responded to eCO_2, but this did not translate to a response in mass. Results from this study suggest that *Larix* and *Picea* will have divergent responses to environment change.

Introduction

The prevalence and capacity by *Picea mariana* (Mill.) B.S.P. (black spruce) and *Larix laricina* (Du Roi) K. Koch (American larch) to sequester carbon (C) as aboveground biomass (AGB) makes changes in ABG of these species an important component of the C budget of boreal forests and peatlands in a substantial portion of North America. However, it is unclear changes in ABG in these species will be affected by increasing CO_2 concentrations and temperatures, and exacerbated by warming occurring faster (3-8 °C by 2100) in the region these species occupy (Northeast Climate Impacts Assessment, 2006). Therefore, understanding the influence of environmental change on the C pool stored in the ABG of these species is necessary to make informed predictions and simulations of future C dynamics in North America.

P. mariana is a cold tolerant species that occupies regions with long cold winters and relatively short growing seasons (Viereck and Johnston, 1990), and is the dominant cover type for large portions of the boreal zone in North America (Little, 1971; Viereck and Johnston, 1990; ACIA, 2005). Stands dominated by *P. mariana* cover approximately 55% of Alaska, the majority of Northern Canada, and parts of Southern Canada (ACIA, 2005). *P. mariana* forests store higher quantities of carbon (C) (biomass and soil C stocks of 11 - 17 kg C m^{-2} Kane and Vogel, 2009) compared to other forest types found in the

same biome (Gower et al., 1997), with above ground net primary production (ANNP) estimates of 1440 - 1660 kg C ha^{-1} yr^{-1} (Gower et al., 1997).

L. laricina is a deciduous coniferous species with a similar distribution to *P. mariana*, and is most often associated with *P. mariana* when found in mixed species stands (Johnston, 1990). Both species are frequently found in peat bogs and wetlands (Johnston, 1990; Viereck and Johnston, 1990), especially in the southern extent of their range (Johnston, 1990; Fryer, 2014). Peatlands are characterized by moist, nutrient-poor, organic peat soils where heterotrophic respiration (HR) is lower than net primary production (NPP). This imbalance results in a net ecosystem exchange (NEE) leading to slow accumulations of C at rates of 20-30 g C m^{-2} yr^{-1} (Yu et al., 2011) over the last ~ 7,000-14,000 years (Yu, 2011; Morris et al., 2018). Slow accumulation of C in peatlands results in total storage estimates of 180-621 Gt C (Gorham, 1990; Yu et al., 2010; Yu, 2012) worldwide, which represents approximately one-third of global terrestrial C (Cao and Woodward, 1998; Yu et al., 2010; Scharlemann et al., 2014). *L. laricina* and *P. mariana* are able to tolerate the nutrient-poor and poorly drained soils that are characteristic of peatlands (Fryer, 2014).

The results of experiments measuring the response of tree growth to CO_2 enrichment, like Free Air CO_2 Enrichments (FACE; Hendrey and Kimball, 1994) studies, show both positive and no response to CO_2 enrichment, depending on the study, species, and location (Hoosbeek et al., 2001; Korner et al., 2005; Norby et al., 2005; Asshoff et al., 2006; Dawes et al., 2011; Jiang et al., 2020). Differing results in CO_2 enrichment studies have been attributed to differences in physiology, phenology, and environmental drivers (Hoosbeek et al., 2001; Dawes et al., 2011). For instance, Hoosbeek et al. (2001)

found that CO_2 enrichment had no effect on vascular and nonvascular plants in peatlands, and attributed the lack of response to CO_2 enrichment to the nutrient-poor nature of peatlands. This demonstrates that plant growth may have unexpected responses to elevated temperature and CO_2 if growth is limited by other factors.

P. mariana trees are known to be temperature sensitive, with studies showing that higher temperatures can result in both increased and decreased growth and productivity in temperate forests of North America (Brooks et al., 1998; ACIA, 2005; Juday and Barber, 2005; Wilmking and Myers-Smith, 2008; Grant et al., 2009; Mamet and Kershaw, 2011; Nishimura and Laroque, 2011; Walker and Johnstone, 2014; Girardin et al., 2016). Most studies measuring the response of C storage to temperature in *P. mariana* and *L. laricina* have been conducted in controlled environments (e.g., Way and Sage, 2008a; Way and Sage, 2008b) or based on large scale assessments of tree rings that typically examine the effect of monthly temperatures rather than the effect of constant warming throughout the year or growing season (Brooks et al., 1998; Girardin et al., 2001; ACIA, 2005; Juday and Barber, 2005; Wilmking and Myers-Smith, 2008; Mamet and Kershaw, 2011; Nishimura and Laroque, 2011; Walker and Johnstone, 2014). Bronson and Gower (2010) used ecosystem warming (soil and air) to evaluate the effect warming (+5 °C) had on *P. mariana*, but ensured that plots with elevated temperatures maintained the same soil moisture as ambient plots through the use of daily irrigation. Bronson and Gower (2010) found that elevated temperatures alone had no effect on photosynthesis or aboveground respiration in *P.*. However, many studies that find negative correlations between growth and temperature attribute the decrease in growth to reductions in soil moisture resulting from warming (Brooks et al., 1998; Wilmking and Myers-Smith, 2008, Walker and

Johnstone, 2014; Girardin et al., 2015). This highlights the importance of understanding both the direct effect of warming on tree growth and indirect effects that may occur, like water limitation from drying.

The Spruce and Peatland Response Under Changing Environments experiment (SPRUCE; Hanson et al., 2017) provides a unique opportunity to study the *in-situ* response of tree growth and C assimilation to environmental change by means of whole-ecosystem warming and elevated CO_2 concentrations while experiencing natural precipitation, sunlight, and soil drying resulting from warming. The SPRUCE experiment evaluates how peatland ecosystems respond to whole-ecosystem warming and elevated CO_2 concentrations by simulating future environmental change in 10 open-top octagonal enclosures (Figure 4.1). Data and results from the SPRUCE experiment are helping to elucidate how peatland species will respond to environmental change, and aid inference into future C dynamics in the system. Initial results suggest that the site which is traditionally a C sink (Griffiths et al., 2017), but will likely switch to a C source with warming (Hanson et al., 2020). Understanding how each component of the C cycle will respond to environmental change is key to our ability to predict and simulate future C dynamics. This study investigates how *P. mariana* and *L. laricina* growth will respond to environmental change, and leverages data from the SPRUCE experiment to improve understanding of future C dynamics in systems containing these species. Here I utilize both manual measurements and terrestrial laser scanning (TLS) data to evaluate the response of *P. mariana* and *L. laricina* growth to SPRUCE treatments over the first four years of the experiment (2016-2020). In this study, I quantified and discussed the effect

of SPRUCE treatments on tree growth using the following metrics: (1) tree height, (2) canopy volume, (3) basal area (BA) at breast height (1.3m), and (4) tree mass.

Methods

Study Site

The SPRUCE experimental site is located in the Marcell Experimental Forest in Northern Minnesota, USA within the S1 bog (47◦30.476 N; 93◦27.162 W; 418 m above mean sea level), which is an 8.1 ha acidic (pore water pH ≈ 3-4) ombrotrophic peat bog with average peat depths of 2.27m and the basal age of the deepest centimeter of peat ranging from 5,100 - 11,100 cal BP (Sebestyen et al., 2011; Slater et al., 2012; Griffiths and Sebestyen, 2016; McFarlane et al., 2018). The S1 bog has a perched water table with little groundwater influence, and from 1969-2009 the mean annual air temperature was 3.4°C and mean annual precipitation was 780mm (Sebestyen et al., 2011). The peatland soil is the Greenwood series, a Typic Haplohemist (http://websoilsurvey.nrcs.usda.gov) with average peat depths to the Wisconsin glacial-age lake bed of 2 to 3 m (Parsekian et al., 2012).

The S1-Bog is dominated by *P. mariana* with contributions to the forest canopy from *L. laricina*. With respect to past land use history, the S1-Bog trees were harvested in strip cuts in 1969 and 1974 to test the effects of seeding on the natural regeneration of *P. mariana*. All re-generation following the strip cut events occurred through natural vegetative processes or seeding events (three to four successful events since 1969). After 46 years of regrowth since 1974, the tree-layer of the experimental peatland plots is still largely represented by an open canopy. All saplings greater than 1 cm diameter at 1.3 m above the *Sphagnum* surface are defined as trees for the SPRUCE study. Vegetation

within the S1-Bog is dominated by the two tree species, various ericaceous shrubs, a limited number of herbaceous species, and is supported by a bryophyte layer dominated by *Sphagnum* spp. mosses. The belowground peat profile and geochemistry are described in Tfaily et al. (2014).

SPRUCE Treatments

The study comprises 10 open-top octagonal enclosed plots (height = 7m; diameter = 12.8m; area = 114.8 m^2). The temperature treatments include deep-peat heating that uses heating elements extending ~3m into the peat (Hanson et al., 2017) combined with air warming achieved by blowing heated air 1m above the peat surface to achieve heating throughout the enclosed air space (Hanson et al., 2017). SPRUCE target differential temperature treatments are +0, +2.25, +4.5, +6.75, and +9 °C with two plots at each temperature treatment. The zero-energy-added plots (+0 treatments) provide the reference temperature for the other treatments in the regression design for this study. In addition, one plot for each temperature treatment receives elevated CO_2 (eCO_2) by injecting pure CO_2 to a target concentration of +500 ppm above ambient (Hanson et al., 2017). Deep peat heating was initiated in June 2014 and air warming started in August 2015 (Hanson et al., 2017) after growth processes were completed in 2015. Elevated CO_2 treatments began in June 2016. Data presented here cover tree growth through the first four years of both elevated temperatures and eCO_2 treatments (2016, 2017, 2018 and 2019).

Growth Measurements

Terrestrial Laser Scanning Point Cloud Measurements

Terrestrial laser scanning (TLS) point clouds were collected in SPRUCE plots during peak biomass (late summer) in each year from 2015-2019. TLS scans were

collected using a Riegl VZ-1000 terrestrial laser scanner from the interior boardwalk within SPRUCE plots. The Riegl VZ-1000 uses a 1550 nm laser to measure the distance to surrounding objects, and sends out millions of laser pulses to measure and digitally represent the physical structure surrounding the scanner (≈5-10 million points per SPRUCE plot). The resulting point clouds (Figure 4.1) can be used to measure objects (i.e., tree sizes and shapes) in the scan. TLS scans were taken from four locations in the boardwalk to achieve coverage of tree canopies from multiple angles. Scans in each plot were co-registered together in RiSCAN PRO to make a single TLS point cloud per plot, per year (Graham et al., 2019a). Point clouds were used to estimate tree height and community canopy volume in SPRUCE plots.

Tree Height -- Tree height was measured using TLS point clouds of SPRUCE plots (Figure 4.1). TLS provides measurements of physical structure with subcentimeter accuracy, and thus provides a method well suited for remote measurements of tree height and crown characteristics. The limited horizontal diameter of SPRUCE plots (~12 m wall to wall) makes the use of traditional height observations using clinometers or height poles difficult, because of the limited sight lines and a reduced range of acute angles to be interpreted, as well as uncertainty in location of the soil surface. Tree height was calculated by subtracting the elevation of the highest TLS return of the tree crown from the elevation of the bog surface below the tree, using TLS reconstructions of the bog surface (Graham et al., 2019b; Graham et al., 2020). In some SPRUCE plots dense clusters of trees make it difficult to identify the top of individual trees for determination of their height. These trees and a small number of other trees (21 of the total 143 trees) were not available for inclusion in growth assessments on individual trees.

Canopy Volume -- Canopy volume for the tree community (*Picea* and *Larix* combined) in SPRUCE plots was calculated as a voxel (volumetric pixel) volume derived from TLS point clouds. I calculated canopy volume at the community level because overlapping tree crowns make isolating crowns in TLS point clouds difficult and inconsistent between years, which would confound a species-specific analysis. Further, if there are species-specific responses community canopy volume would allow us to assess how the tree community as a whole responds to warming and eCO_2. The ability for voxel volume to predict metrics like aboveground biomass (AGB) and leaf area index (LAI) is well documented in the literature (e.g., Greaves et al., 2015; Li et al., 2015; Olsoy et al., 2014a; Olsoy et al., 2014b), and thus I use voxel volume in SPRUCE plots as an alternative independent measure of tree community AGB. Calculations of voxel volumes were achieved by first manually extracting trees and tree clusters from TLS point clouds using CloudCompare v2.8 (CloudCompare, 2017). Once trees were isolated from the rest of the point cloud (e.g., shrub understory and instrumentation), trees were voxelized by breaking point cloud domains into regular 0.05x0.05x0.05m 3-D cartesian grids along the x, y, and z axes (grid cell volume = $0.00125m^3$). Voxel volume was then calculated by enumerating the number of voxels that contained at least one TLS return (Figure 4.1).

The decision to use 0.05x0.05x0.05m voxels (0.05m voxels hereafter) was based on an iterative assessment in which voxel size was varied between 0.001-0.25m and canopy volume was calculated for seven trees from each species (n=14 total) that were destructively sampled for AGB estimates. TLS canopy voxel volumes were correlated with empirical biomass estimates to determine the optimal voxel size (Figure 4.2). The

result of this assessment was an asymptotic relationship where the coefficient of determination (R^2) increases from 0.001-0.05m and has fairly similar values from 0.025-0.25m. Therefore, I selected a voxel size of 0.05m, because it had the strongest correlation ($R^2 = 0.92$) with AGB and was better suited for change detection than larger voxel sizes.

Traditional Measurements

Basal Area -- Basal area (BA) estimates were derived from measured bole circumference at 1.3m collected annually in late February or early March, with the assumption that all stems had a circular cross section. To ensure consistency between years, a laser leveling system (Spectra LL400) was used in combination with a tripod to mark trees at 1.3m for the location of the circumference measurements (Hanson et al., 2018). Once established, the marks were replaced annually to enable re-measurements at the same locations. Circumference measurements were taken at the 1.3m marked location with steel DBH measuring tapes, taken to the nearest 0.001m.

Annual measurements of BA were combined with end-of-season TLS height measurement from the previous season (e.g., tree heights measured in September 2019 are matched with BA estimates from March 2020). I assumed no change in growth in stem circumference and tree height over this dormant period. The mid-winter period for circumference measures provided a stable period between years when access to all trees could be accomplished without damaging the bog surface. Annual growth increments represent the difference between growth assessments for each year (e.g., the growth metrics for 2017 represent the difference between February 2018 and February 2017 assessments).

Tree Mass --Tree mass change in C units was calculated from an allometric relationship derived from measurements of destructively sampled trees from both species at the S1 bog. The relationship comes from a simple linear model built using 44 destructively harvested trees (22 from each species); these data comprise the trees contained in the Hanson et al. (2012) dataset plus the 14 trees harvested and used to correlate tree mass with voxel volume. The allometric equation uses BA (at 1.3m) times tree height as the independent variable to estimate total tree dry mass, shown in equation 2.

$$\text{Equation 2: } TDM = 1{,}265 + (BA*H) * 416{,}286$$

where *TDM* is tree dry mass (g), *BA* is basal area at 1.3m (m), and *H* is tree height (m). This relationship explains 91% of the variation in tree dry mass (Figure 4.3). From tree dry mass, tree C content was calculated assuming that 48% of dry mass is C.

Statistical Analyses

Tree growth is often proportional to tree size, therefore I explored the use of relative instead of absolute growth as the metric used in regression models. To determine whether to use relative growth when assessing temperature and CO_2 treatments, I created linear models for tree growth as a function of tree size for all metrics individually. Linear models were species-specific except the voxel volume metric, in which species were combined. When these linear models had a slope parameter that was significantly different from zero, I used relative growth when assessing treatment responses. Relative growth was calculated for individual trees by dividing the increment by the initial value (e.g., mass increment from 2017-2018 is divided by the 2017 mass).

Annual growth for each metric (height, voxel volume, basal area, and mass) was calculated by subtracting the value for the current year from the previous year, and 4-year cumulative growth was calculated as the metric in the last year subtracted from the metric in the first year. I used a regression approach to evaluate the effect of warming and eCO_2 on annual and cumulative growth. The basis for the warming regression dependent variable was selected as the mean air temperature at 2 m (Hanson et al., 2016) from May to September in each year (2016, 2017, 2018 and 2019) to reflect the temperatures encompassing the full 'growing season'. CO_2 enrichment was treated as a factor in regression analyses because treatment was binary. To evaluate the effect treatments had on growth I created five linear models for each growth metric, and performed a model selection process to find the best supported model based on Akaike Information Criterion (AIC) (Akaike, 1973; Akaike, 1974, Akaike, 1981) score and model complexity. I considered models with $\Delta AIC > 2$ (ΔAIC = minimum AIC - AIC) to have substantial support compared to other models (Sakamoto et al., 1986; Burnham and Anderson, 1998), and therefore the best supported model was chosen as the most parsimonious model with a $\Delta AIC < 2$. This process was repeated for each metric by combining growth data from all years (termed annual growth), as the 4-year cumulative growth (termed cumulative growth), and for each year individually. The five candidate models comprised: 1) null - growth as a function of 1 (intercept), 2) simple CO_2 - growth as a function of CO_2, 3) simple temperature - growth as a function of temperature, 4) complex - growth as a function of temperature and CO_2, and 5) interaction - growth as a function of temperature, CO_2, and their interaction. I also made non-linear models allowing for an optimal growth temperature, however these models were not selected as the best

supported model for any metric in either species, and therefore will not be discussed. After I selected the best supported model, I characterized parameters at two significant levels ($p < 0.05$) and ($p < 0.001$) and reported the effect of treatment on growth as the slope parameters from the best supported model. All statistics and tests were produced using Program R (R Core Team, 2017).

Results

A total of 124 trees (96 *P. mariana* and 28 *L. laricina*) were used to assess tree growth response to SPRUCE treatments, with an average of 10 *P. mariana* trees per plot (range: 3 - 17 trees) and 3 *L. laricina* trees per plot (range: 1 - 5 trees). Tree growth was generally higher in *P. mariana* than *L. laricina* (Table 4.1). *Picea* BA increment was significantly correlated with initial (start of year for annual and start of first year for cumulative) *Picea* BA (annual $p < 0.001$, $R^2 = 0.18$; cumulative $p < 0.001$, $R^2 = 0.32$). Similarly, *Larix* BA increment was significantly correlated with initial BA (annual $p < 0.001$, $R^2 = 0.11$; cumulative $p = 0.027$, $R^2 = 0.17$). Tree mass increment was also significantly correlated with initial mass for both *Picea* (annual $p < 0.001$, $R^2 = 0.42$; cumulative $p < 0.001$, $R^2 = 0.53$) and *Larix* (annual $p < 0.001$, $R^2 = 0.23$; cumulative $p = 0.002$, $R^2 = 0.30$). In contrast, the relationship between height increment and initial height was non-significant for *Picea* (annual $p = 0.069$; cumulative $p = 0.295$) and *Larix* (annual $p = 0.771$; cumulative $p = 0.460$). Community canopy volume did not correlate with initial volume (annual $p = 0.818$; cumulative $p = 0.055$). Significant correlations between growth and tree size indicate that growth is proportional to size (Figure 4.4 & Figure 4.5), and therefore I assessed tree growth responses as relative growth for BA and mass increments, and as absolute growth for height increment and community volume.

Absolute Height Growth

Height increment of *Picea* was negatively influenced by both temperature and eCO_2 treatments (Table 4.2), and showed an interaction between temperature and CO_2. The best supported models for annual height increment of *Picea* was the most complex model (interaction), which includes temperature, CO_2, and a temperature-CO_2 interaction term. Temperature was highly significant ($p < 0.001$) while the CO_2 and interaction terms were significant ($p < 0.05$) for annual height. Temperature had a negative effect (-0.019m $year^{-1}$ $°C^{-1}$) on *Picea* height increment, as did eCO_2 (-0.333m year). However, the interaction term was positive (0.013m $year^{-1}$ $°C^{-1}$), which indicates that temperature was less influential on height increment when trees were grown in eCO_2 (Figure 4.6). The best supported model for cumulative *Picea* height increment was the complex model containing a term for temperature and CO_2. The temperature term was highly significant ($p < 0.001$) and had a negative effect (-0.051m C^{-1}), while the CO_2 term was not significant ($p = 0.056$) and also had a negative effect (-0.124m). For individual years, the best supported model in each year contained terms for either temperature, CO_2, or both. The best supported models for individual years were: 2016 simple temperature, 2017 simple CO_2, 2018 complex, and 2019 interaction. Details on the best supported yearly models can be found in Table 4.3 cumulative and annual height increments were not affected by temperature or eCO_2. For annual and cumulative *Larix* height increment, the best supported model was the null model, which suggests neither temperature nor CO_2 had an effect on height increment. For annual height increment, the simple model including temperature had a lower AIC than the null model but the ΔAIC was 0.47, resulting in the selection of the null model. The model with the lowest AIC for

cumulative *Larix* height increment was also the simple model including temperature, but the ΔAIC of the null model was 1.11 and therefore the null model was selected as the best supported model. In individual years the best supported models were: 2016 null, 2017 simple CO_2 (though the CO_2 term was nonsignificant), 2018 null, and 2019 simple temperature.

Relative Basal Area Growth

Picea BA increment was not influenced by temperature or eCO_2. The model of *Picea* BA increment containing only a term for CO_2 treatment had the lowest AIC, however the null model had a ΔAIC of 1.16, and was therefore chosen as the best supported model. The null model was the best supported model for cumulative *Picea* BA increment, followed by the model including only temperature (ΔAIC = 1.44) and the model including only CO_2 (ΔAIC = 2.00). The best supported yearly models of *Picea* BA increment were: 2016 simple temperature, 2017 simple CO_2, 2018 null, and 2019 null.

Annual BA increment of *Larix* was not influenced by temperature or eCO_2, but cumulative BA increment was positively influenced by temperature. The model of annual *Larix* BA increment with the lowest AIC was the simple model with a term for temperature, however the null model was selected as the best supported model because its ΔAIC was 1.57. The best supported model for cumulative BA increment was the simple model including a temperature term. This model had the lowest AIC, with the next lowest coming from the most complex model with temperature-CO_2 interaction (ΔAIC = 1.00). The effect of temperature on cumulative BA increment from this model ($p = 0.038$) was 2.708% $°C^{-1}$ (as a percentage of the starting BA). *Larix* BA increment best supported models were: 2016 null, 2017 null, 2018 null, and 2019 simple temperature.

Relative Mass Growth

Picea mass increment was negatively influenced by temperature annually, but cumulative mass increase was not influenced by temperature or eCO_2. The model with the lowest AIC for *Picea* annual mass increment was the model including terms for both temperature and CO_2 but not the interaction. However, the simple model containing only a term for temperature had a ΔAIC of (0.20) and was chosen as the best supported model, which exhibited a significant negative effect of temperature on *Picea* annual mass increment. For *Picea* cumulative mass increase, the null model had the lowest AIC followed by the simple model including temperature (ΔAIC = 1.25). The best supported yearly models for *Picea* mass increment were: 2016 simple temperature, 2017 null, 2018 null, and 2019 null.

Temperature positively influenced both *Larix* annual mass increment (Figure 4.6) and cumulative mass increment (Figure 4.7). The simple model containing a term for temperature had the lowest AIC for both annual and cumulative mass increment and was selected as the best supported model in both cases. Models containing temperature and CO_2 terms were the next best candidate model for both annual (ΔAIC = 1.69) and cumulative (ΔAIC = 2.00) mass increase. The temperature term in the best supported models were significant for annual ($p = 0.043$) and cumulative ($p = 0.016$) mass increase, exhibiting negative effects on mass increase (annual = 0.454% $year^{-1}$ $°C^{-1}$; cumulative = 2.189% $°C^{-1}$, as percentage of starting mass). For individual years, the best supported models of *Larix* mass increment were: 2016 null, 2017 null, 2018 null, and 2019 simple temperature.

Absolute Canopy Volume Growth

Neither temperature or eCO_2 had an effect on annual or cumulative community canopy volume increase (Figure 4.8). The model of annual volume increase with the lowest AIC was the null model, followed by the model including a CO_2 ($\Delta AIC = 1.80$). Similarly, the null model for cumulative volume increase had the lowest AIC, but was followed by the most complicated model which includes a temperature-CO_2 interaction term ($\Delta AIC = 1.13$). In each individual year, the best supported model for community volume increment was the null model for all years.

Discussion

Our results provide evidence that *Picea* and *Larix* growth will respond to increasing air temperatures, but the response differs in magnitude and direction. The divergent responses of *Picea* (- response) and *Larix* (+ response) growth to temperature resulted in no overall growth response to temperature in community canopy volume. The lack of tree growth response to temperature as a community in this study suggests that tree AGB may not respond to temperature because opposing species-specific responses largely offset one another. This is similar to findings from a Girardin et al. (2016), which used a robust dendrochronological analysis to measure the effect of environmental change on tree growth in Canada's boreal forest. Girardin et al. (2016) found that while there were significant trends in growth, they varied spatially and between species, with positive and negative trends compensating for each other and resulting in no overall growth stimulation over the boreal zone.

The negative growth response to warming observed in *Picea* in this study is consistent results from Jensen et al. (2019). Jensen et al. (2019) used ELM_SPRUCE, a

land surface model parameterized at the SPRUCE site, to simulate tree growth responses to SPRUCE treatments. Data from Jensen et al. (2019) suggest that there is an interaction between temperature and eCO_2 that influences *Picea* growth, in which the negative effect of temperature on NPP is reduced in the presence of eCO_2. Interestingly, I see this interactive response in *Picea* height increment, though this interaction is not detectable in our mass increment data. While our results for *Picea* generally agree with those from Jensen et al. (2019), our results for *Larix* are less consistent. Modeled *Larix* NPP from Jensen et al. (2019) decreased with warming and ambient CO_2, and exhibited small increases in NPP with eCO_2. This is contrary to our results, in which *Larix* growth was unresponsive to eCO_2 and increased with temperature.

The species-specific growth responses to temperature observed in this study are corroborated by measurements of gas exchange in *Picea* and *Larix* at the SPRUCE site (Dusenge et al., *In Review*). Our finding of a negative growth response to warming in *Picea* is supported by Dusenge et al. (*In Review*), which observed that warming led to reduced stomatal conductance, decreased intercellular CO_2 concentrations inducing stomatal limitations for carbon gain, and increased respiration in *Picea*. Additionally, warmer leaf temperatures induced slight increases in *Larix* stomatal conductance and net CO_2 assimilation rate, did not influence intercellular CO_2 concentrations, and warming resulted in a smaller increase in respiration compared to *Picea,* all of which further buttress our observation of increased *Larix* growth with warming. Based on their findings, Dusenge et al. (*In Review*) suggested that *Larix* prioritized C uptake and growth, while *Picea* prioritized water retention in response to warming and the associated increase in vapor pressure deficit, which are conclusions further supported by our results.

The connection between warmer temperatures, water limitations, and negative growth responses of *Picea* to temperature has also been described in previous studies (Wilmking and Myers-Smith, 2008; Walker and Johnstone, 2014).

Conflicting results between our study and that of Bronson and Gower (2010) are likely due to differences in the manner in which soil moisture was treated. In contrast to our study, Bronson and Gower found that ecosystem warming did not affect *P. mariana* photosynthesis or aboveground autotrophic respiration. However, Bronson and Gower (2010) controlled for soil moisture with daily irrigation, ensuring that trees growing with the elevated temperatures had the same soil moisture as trees grown with ambient temperature. In contrast, I did not add water to the system and allowed soil to dry naturally through evapotranspiration in response to temperature treatments. The combination of these results provides evidence to suggest that *Picea* growth is not reduced when temperature is raised while increasing water supply, but warming without additional water in the system results in reductions in *Picea* growth. Therefore, the ability to predict how *Picea* growth will respond to environmental changes will depend on the ability to simulate and project trends in precipitation, as well as temperature.

Other than *Picea* height increment, eCO_2 had little effect on tree growth. The eCO_2 treatments in this study did not influence annual or cumulative growth in any other metric. The only metric besides *Picea* height that eCO_2 had a significant effect on was *Picea* BA increment in 2017, in which eCO_2 had a positive effect on growth. These results are consistent with results from a peatland FACE site (Hoosbeek et al., 2001). Hoosbeek et al. (2001) found no response to elevated CO_2 in vascular and nonvascular

plants at a FACE study in peatlands, and suggested that the reason for the lack of CO_2 fertilization was the inherently low nutrient levels in peatlands.

There is evidence to suggest that both species acclimated to our experimental treatments over the four years of this study. While *Picea* height increment responded to treatments in all years, BA and mass only had significant correlations with temperature in the first year. The deterioration of the relationship between temperature and *Picea* mass increment over time can be observed in plots of individual years (Figure 4.9). Acclimation of *Picea* photosynthesis, *Picea* respiration, and *Larix* respiration to warmer growing temperatures have been observed in previous studies (Tjoelker et al., 1999; Way and Sage, 2008). Way and Sage (2008) demonstrated that the thermal optimum for net CO_2 assimilation was higher for *Picea* grown in elevated temperatures compared to those at lower growth temperatures, which may explain why the only year *Picea* mass correlated with temperature was the first year of the study. Interestingly, *Larix* response to temperature over time appeared to do the opposite of *Picea*, where all *Larix* growth metrics only correlated with temperature in the last year. Further, the relationship between *Larix* mass and temperature appears to strengthen throughout the study (Figure 4.9). However, it is difficult to assess whether both species thermally acclimated, or whether *Picea* growth responded less negatively to warming and *Larix* responded more positively to warming over time because there were more nutrients available for uptake. Increased nutrient uptake would be a result of accelerated nutrient cycling induced by warming, and is supported by leaf nitrogen concentrations increasing with warming in both *Picea* and *Larix* at SPRUCE (Dusenge et al., *In Review*).

Summary

While ANPP in both *P. mariana* and *L. laricina* responded to SPRUCE treatments, the manner in which they responded differed, with *L. laricina* showing an increase in annual ANPP as a result of elevated temperatures and *P. mariana* showing a reduction. Data from the early years of SPRUCE warming and eCO_2 provide evidence to suggest that *Picea* growth will decrease in response to environmental change, but the response to temperature may weaken over time. In contrast, our data provide evidence to suggest that *Larix* growth will increase in response to environmental change and growth may become more responsive to temperature over time. Therefore, whether systems containing *Larix* and *Picea* increase C inputs in response to environmental change will be dependent on the proportion of each species in the system (77% *Picea* & 23% *Larrix* here). This could have a meaningful effect on peatland C budgets, considering tree ANPP contributes 13% of carbon inputs to the S1 bog (Griffiths et al., 2017). Since NEE is a balance of positive and negative C fluxes, and the net C sink in peatlands is much smaller in magnitude than component fluxes, small changes in a component flux can have a relatively large effect on NEE. Our results help improve understanding of how C inputs from these species will respond to environmental change, which is important for studies that quantify boreal forest and peatland C budgets and how they will respond to future climatic conditions (e.g., Hanson et al., 2020). Further, data and conclusions from this study can be used to help inform modeling efforts that simulate how carbon dynamics will respond to future climatic conditions.

Acknowledgments

I would like to thank the following individuals for their participation in the collection of mid-winter tree growth assessments at the SPRUCE site over multiple seasons: Misha Krassovski, Kenneth A. Lowe, Zack T. Moore, W. Robert Nettles, Kyle Pearson, Jennifer Peters, Donald E. Todd and Eric J. Ward. I would also like to thank Lucas Spaete for assistance in TLS data collection design.

This material is based upon work supported by the U.S. Department of Energy, Office of Science, Office of Biological and Environmental Research. Jake Graham was supported under a contract between Oak Ridge National Laboratory and Boise State University (#4000145196) with funding for the SPRUCE project from the U.S. Department of Energy (DOE), Office of Science, Office of Biological and Environmental Research. Oak Ridge National Laboratory is managed by UT-Battelle, LLC, for DOE under contract DE-AC05-00OR22725. Additional funding was provided by the Department of Geosciences, Boise State University. Data sets pertaining to this study are in the online project archive at http://mnspruce.ornl.gov and for long-term storage in the U.S. Department of Energy's (DOE) Environmental Systems Science Data Infrastructure for a Virtual Ecosystem (ESS-DIVE; http://ess-dive.lbl.gov/)

Table 4.1. Summaries of tree sizes and growth metrics for *Picea* and *Larix* species.

Species	Growth Metric	Value			Annual Growth		
		Mean	**Min**	**Max**	**Mean**	**Min**	**Max**
Picea	Height (m)	5.09	1.59	8.37	0.17	-0.08	0.56
	Basal Area (cm^2)	27.8	2.1	70.7	1.5	-3	10.2
	Tree Mass (kg C)	3.80	0.68	12.12	0.26	-0.16	1.64
Larix	Height (m)	4.21	1.88	7.33	0.13	-0.08	1.09
	Basal Area (cm^2)	19.1	2.4	81.5	0.8	-1.6	5.7
	Tree Mass (kg C)	2.66	0.70	12.33	0.13	-0.15	1.48
Combined	Vox. Volume (m^3)	15.10	5.61	29.73	1.51	-0.65	8.84

Table 4.2. Details for the best supported models for all growth metrics for *Picea* and *Larix* for annual and cumulative increments. N = null model, T = model with temperature term, T+C is the model with temperature and CO_2 terms, and T+C+I = model with CO_2 and interaction term. BA is basal area.

	Species	Metric	Best Model	Parameter	Value	p	R^2
Annual	*Picea*	Height	T+C+I	Intercept**	0.602	0.000	
				Temp**	-0.019	0.000	
				CO2*	-0.333	0.002	
				Temp x CO2*	0.013	0.005	0.105
	Picea	BA	N	Intercept**	6.344	0.000	0.000
	Picea	Mass	T	Intercept**	13.597	0.000	
				Temp*	-0.284	0.003	0.024
	Larix	Height	N	Intercept**	0.134	0.000	0.000
	Larix	BA	N	Intercept**	6.272	0.000	0.000
	Larix	Mass	T	Intercept	-5.309	0.302	
				Temp*	0.454	0.043	0.037
	Combined	Volume	N	Intercept**	1.505	0.000	0.000
4-Year Cumulative	*Picea*	Height	T+C	Intercept**	1.878	0.000	
				Temp**	-0.051	0.000	
				CO2	-0.124	0.056	0.202
	Picea	BA	N	Intercept**	9.795	0.000	0.000
	Picea	Mass	N	Intercept**	10.240	0.000	0.000
	Larix	Height	N	Intercept**	0.535	0.000	0.000
	Larix	BA	T	Intercept	-47.934	0.106	
				Temp*	2.708	0.038	0.155
	Larix	Mass	T	Intercept	-38.654	0.059	
				Temp*	2.189	0.016	0.203
	Combined	Volume	N	Intercept*	1.044	0.009	0.000

Table 4.3. Details for the best supported models for all growth metrics for *Picea* and *Larix* in individual years. N = null model, T = model with temperature term, C = model with CO_2 term, T+C is the model with temperature and CO_2 terms, and T+C+I = model with CO_2 and interaction term. BA is basal area.

Year	Species	Metric	Best Model	Parameter	Value	p	R^2
2016	*Picea*	Height	T	Intercept**	0.534	0	
				Temp*	-0.014	0.015	0.061
2017	*Picea*	Height	C	Intercept**	0.206	0	
				CO2**	-0.083	0	0.145
2018	*Picea*	Height	T+C	Intercept**	0.605	0	
				Temp**	-0.02	0	
				CO2*	0.052	0.017	0.215
2019	*Picea*	Height	T+C+I	Intercept**	0.926	0	
				Temp**	-0.035	0	
				CO2**	-0.76	0	
				Temp x CO2**	0.033	0	0.419
2016	*Picea*	BA	T	Intercept*	17.68	0.001	
				Temp*	-0.453	0.046	0.042
2017	*Picea*	BA	C	Intercept**	3.578	0	
				CO2*	2.906	0.011	0.066
2018	*Picea*	BA	N	Intercept**	5.421	0	0
2019	*Picea*	BA	N	Intercept**	7.838	0	0
2016	*Picea*	Mass	S	Intercept**	23.578	0	
				Temp**	-0.664	0.001	0.115
2017	*Picea*	Mass	N	Intercept**	6.011	0	0
2018	*Picea*	Mass	N	Intercept**	6.347	0	0
2019	*Picea*	Mass	N	Intercept**	8.074	0	0
2016	*Larix*	Height	N	Intercept**	0.094	0.001	0
2017	*Larix*	Height	C	Intercept**	0.114	0	
				CO2	-0.067	0.12	0.09
2018	*Larix*	Height	N	Intercept**	0.113	0.001	0
2019	*Larix*	Height	T	Intercept	-0.704	0.085	
				Temp*	0.043	0.023	0.183
2016	*Larix*	BA	N	Intercept*	4.214	0.017	0
2017	*Larix*	BA	N	Intercept*	3.975	0.002	0
2018	*Larix*	BA	N	Intercept**	6.396	0	0
2019	*Larix*	BA	T	Intercept	-26.859	0.133	
				Temp*	1.693	0.039	0.154
2016	*Larix*	Mass	N	Intercept**	3.012	0.001	0
2017	*Larix*	Mass	N	Intercept**	2.999	0	0
2018	*Larix*	PctDC	N	Intercept**	4.784	0	0
2019	*Larix*	Mass	T	Intercept	-27.163	0.059	
				Temp*	1.664	0.012	0.218

2016	Combined	Growth	N	Intercept*	0.635	0.006	0
2017	Combined	Growth	N	Intercept**	3.614	0.001	0
2018	Combined	Growth	N	Intercept	0.728	0.058	0
2019	Combined	Growth	N	Intercept*	1.044	0.009	0

* Significant ($p < 0.05$); ** highly significant ($p < 0.001$)

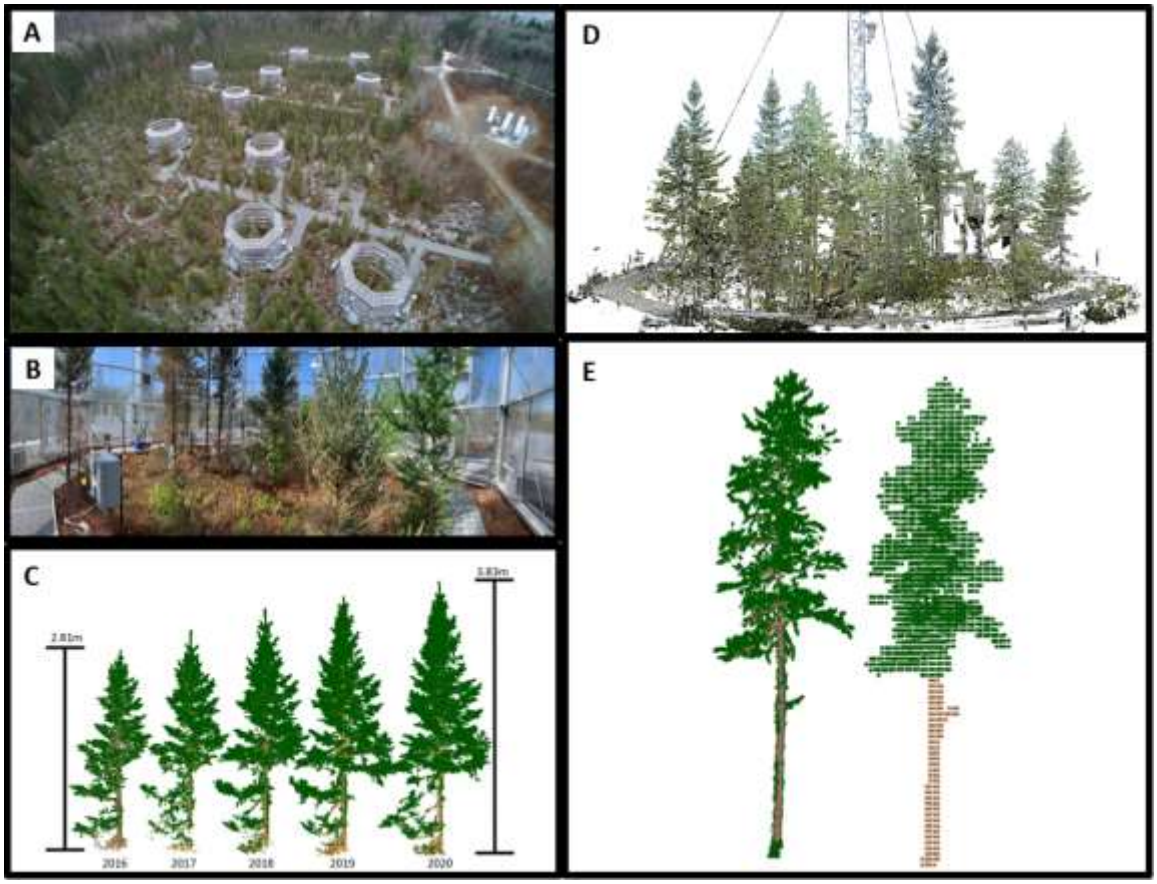

Figure 4.1. Aerial image of the 10 SPRUCE plots containing the trees in this study (A), image of the interior of a SPRUCE plot (B), point clouds of an example tree for the five measurements made for this study (C), terrestrial laser scanning point cloud of a SPRUCE plot (D), and an example of a point cloud of a tree (left) and the 0.05m voxelized version (right) of the same tree (E).

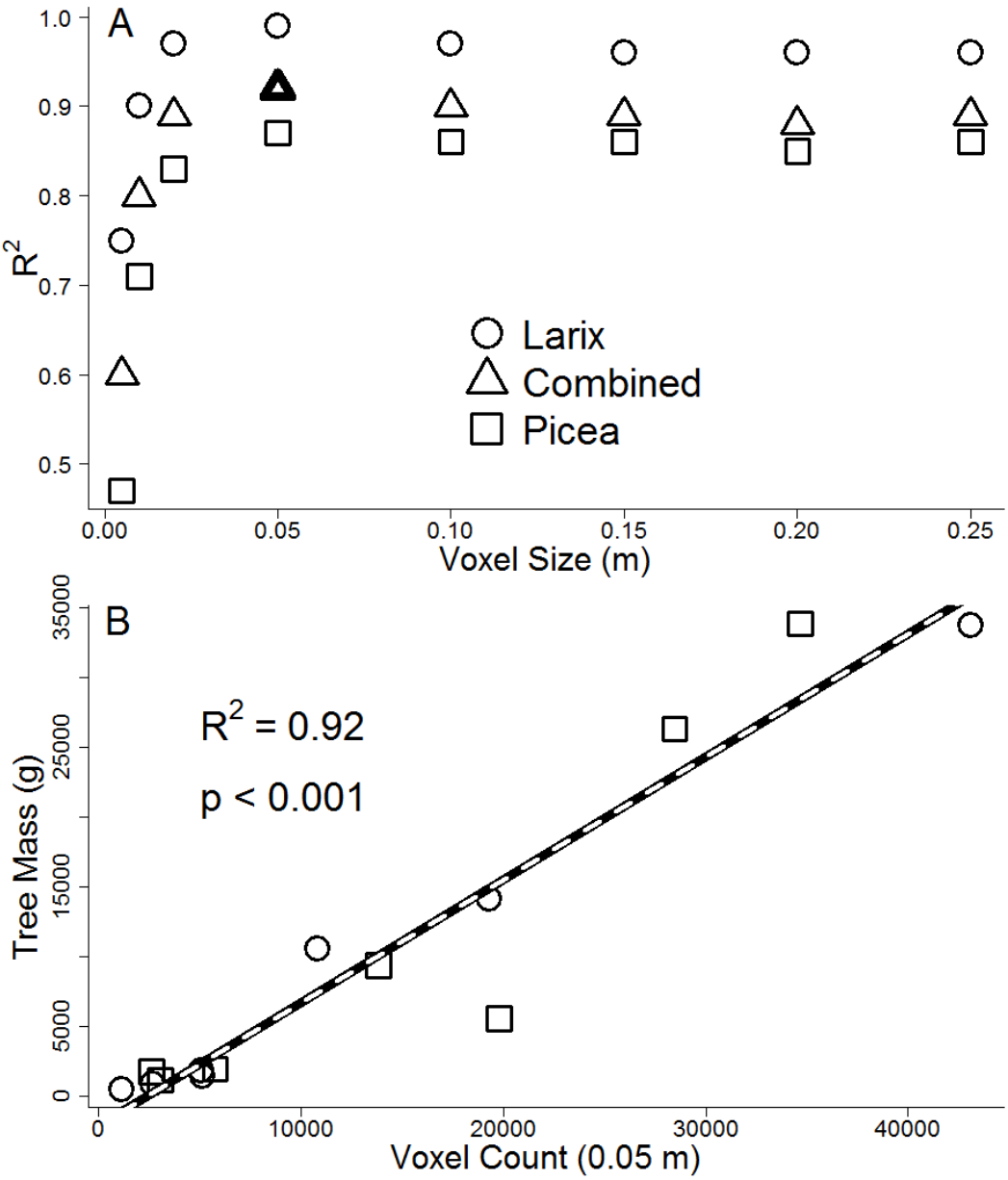

Figure 4.2. Coefficient of determination for regressions of voxel count and tree dry mass at different voxel sizes (A), and a plot of voxel volume for the chosen voxel size (0.05m voxels) correlated with tree dry mass for species combined (B). The bolded symbol in (A) reflects the relationship displayed in (B).

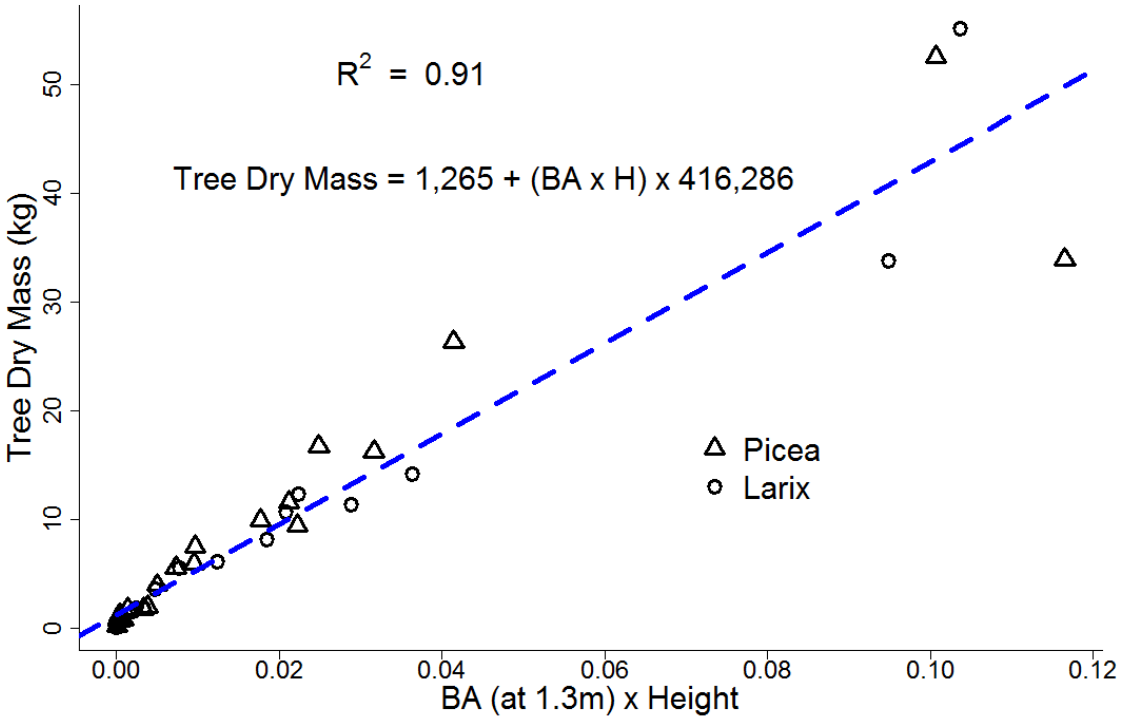

Figure 4.3. Allometric relationship used to estimate tree dry mass.

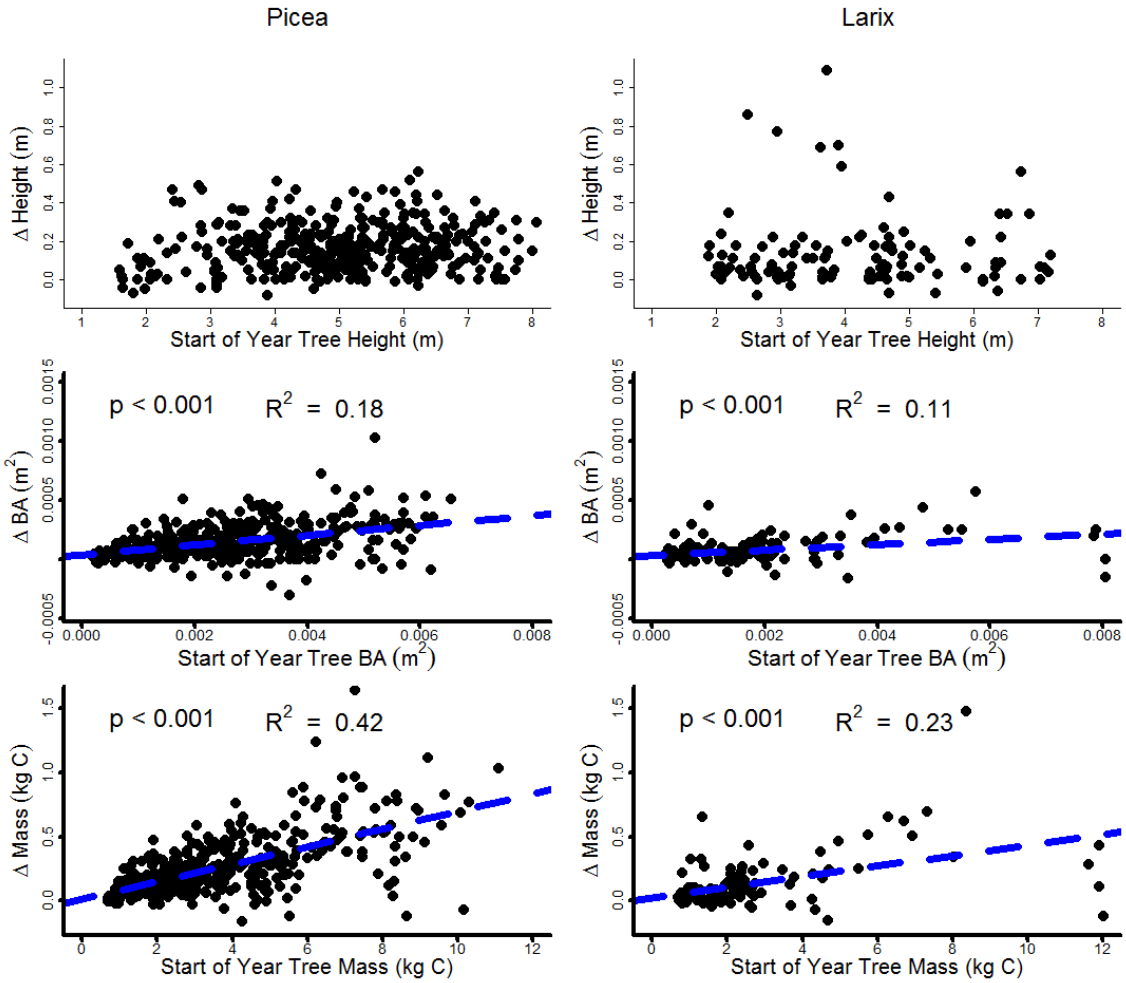

Figure 4.4. Species-specific correlations between annual growth for all years (2016, 2017, 2018, & 2019) and the tree size at the start of the year for all metrics, significant correlations were used to normalize growth metrics. Significant correlations are marked with bold axes and a dashed blue regression line, correlations with p values between 0.05 and 0.15 are marked with dotted blue lines. Plots with no regression line had p values > 0.15.

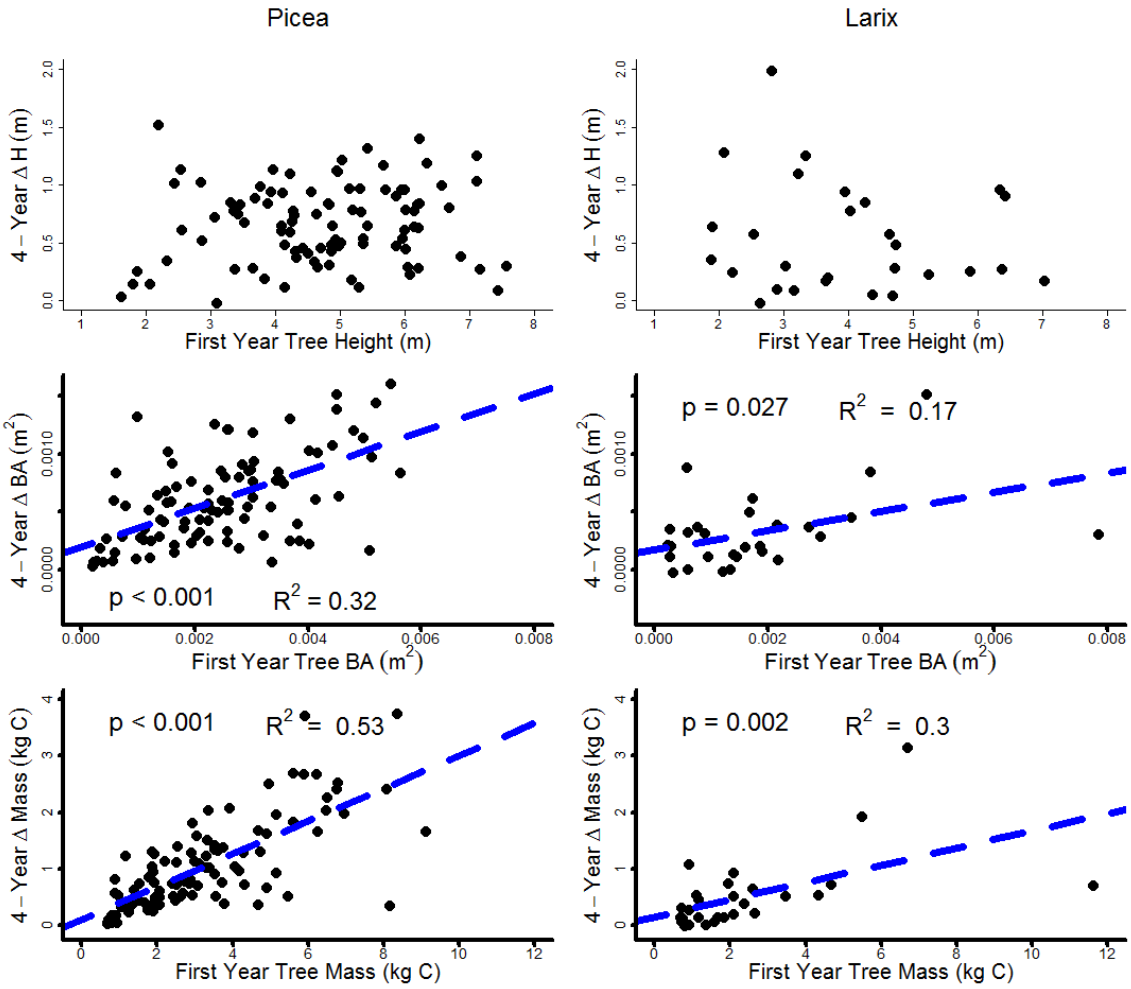

Figure 4.5. Species-specific correlations between 4-year cumulative growth from 2016 through 2020 and tree size for all metrics, significant correlations were used to normalize growth metrics. Significant correlations are marked with bold axes and a dashed blue regression line, correlations with p values between 0.05 and 0.15 are marked with dotted blue lines. Plots with no regression line had p values > 0.15.

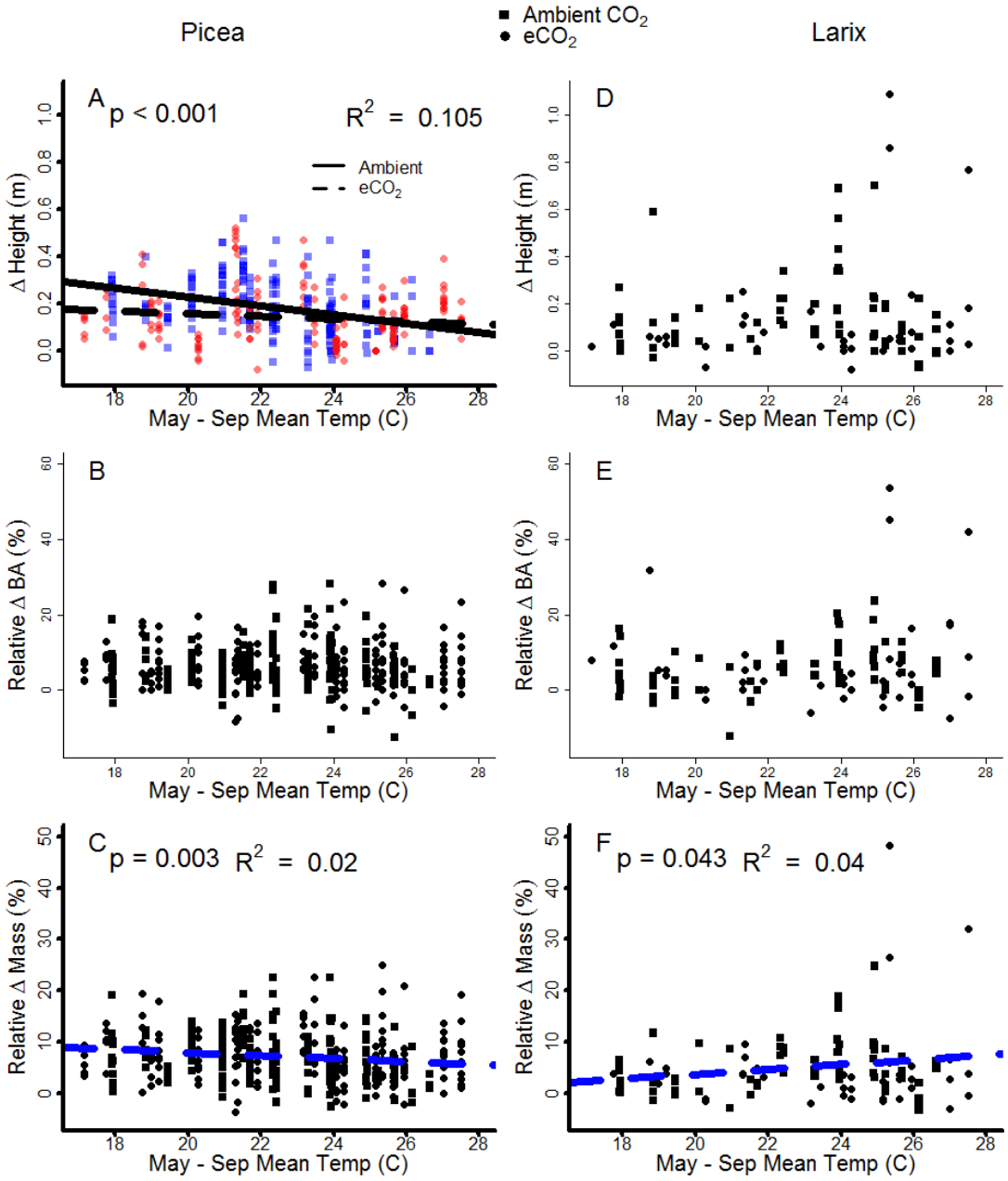

Figure 4.6. Correlations between growing season mean temperature and annual tree growth for *Picea mariana* height increase (A), basal area (B), tree mass (C), and *Larix laricina* height increase (D), basal area (E), and tree mass (F). Bolded axes on plots denote growth metrics for which the best supported model was not the null model, coloration of points marks metrics that had a CO_2 term in the best supported model, a single regression line marks metrics for which the best supported model was the simple linear model of growth as a function of temperature, and multiple regression lines indicate that the best supported model included both temperature and CO_2.

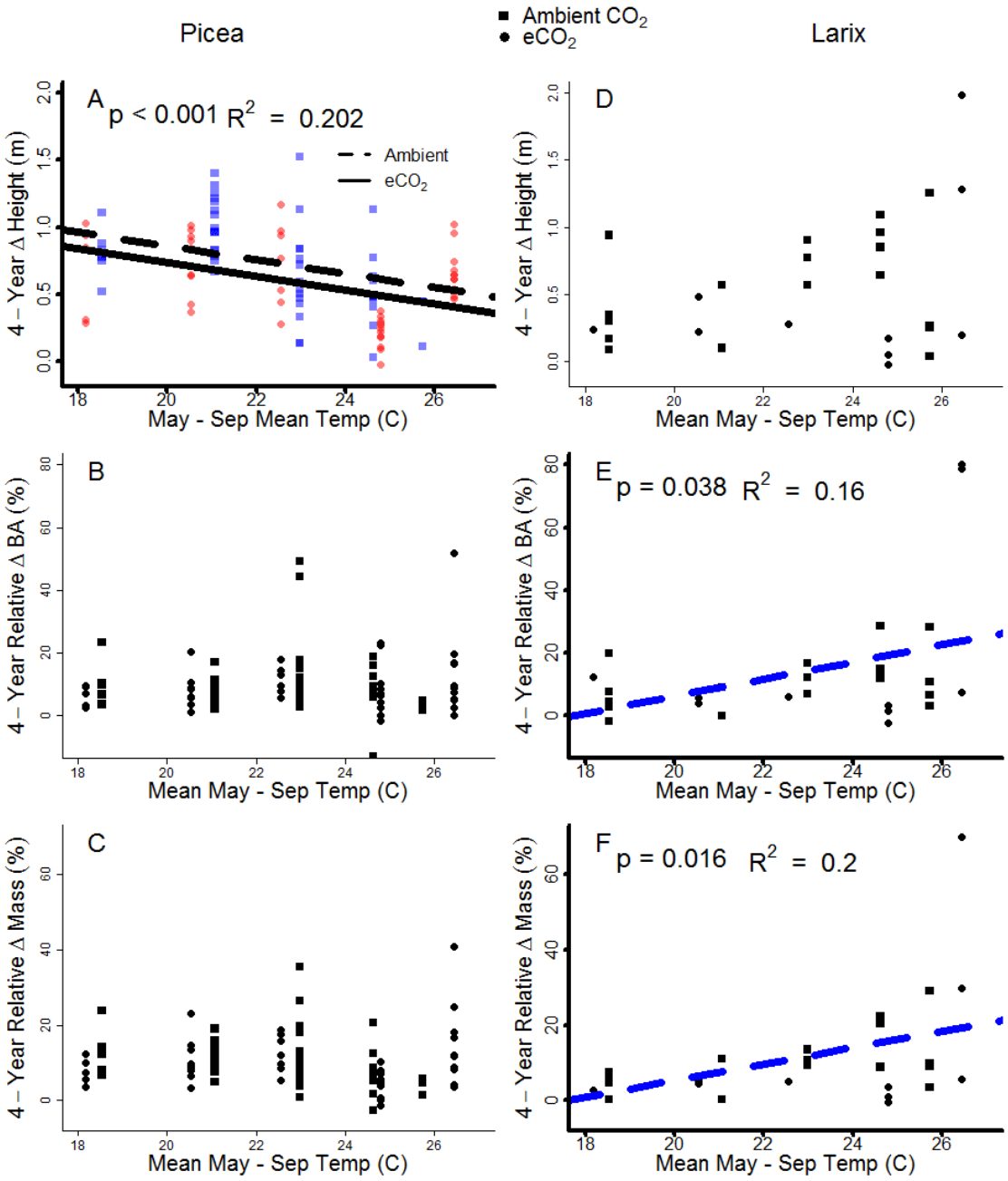

Figure 4.7. Correlations between mean growing season temperature and 4-year cumulative tree growth for *Picea mariana* change in height (A), basal area (B), tree mass (C), and *Larix laricina* change in height (D), basal area (E), and tree mass (F). Black dots represent trees grown in ambient CO_2 concentrations and red dots represent trees grown with CO_2 enrichment. Bolded axes on plots denote growth metrics for which the best supported model was not the null model, coloration of points marks metrics that had a CO_2 term in the best supported model, a single regression line marks metrics for which the best supported model was the simple linear model of growth as a function of temperature, and multiple regression lines indicate that the best supported model included both temperature and CO_2.

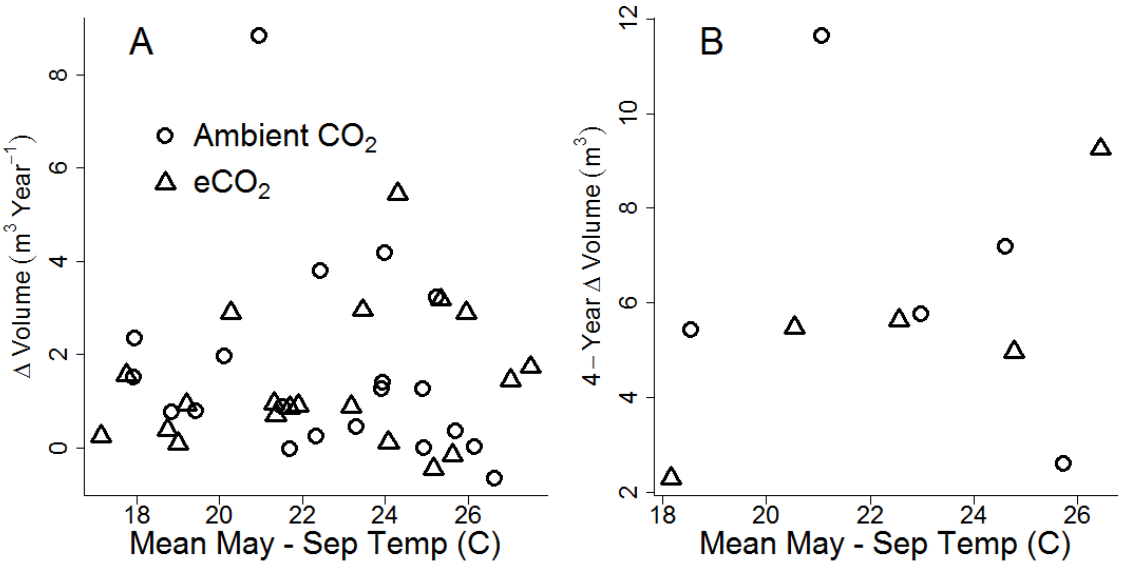

Figure 4.8. Annual voxel volume increase as a function of growing season temperature (A) and four-year cumulative voxel volume increase (B).

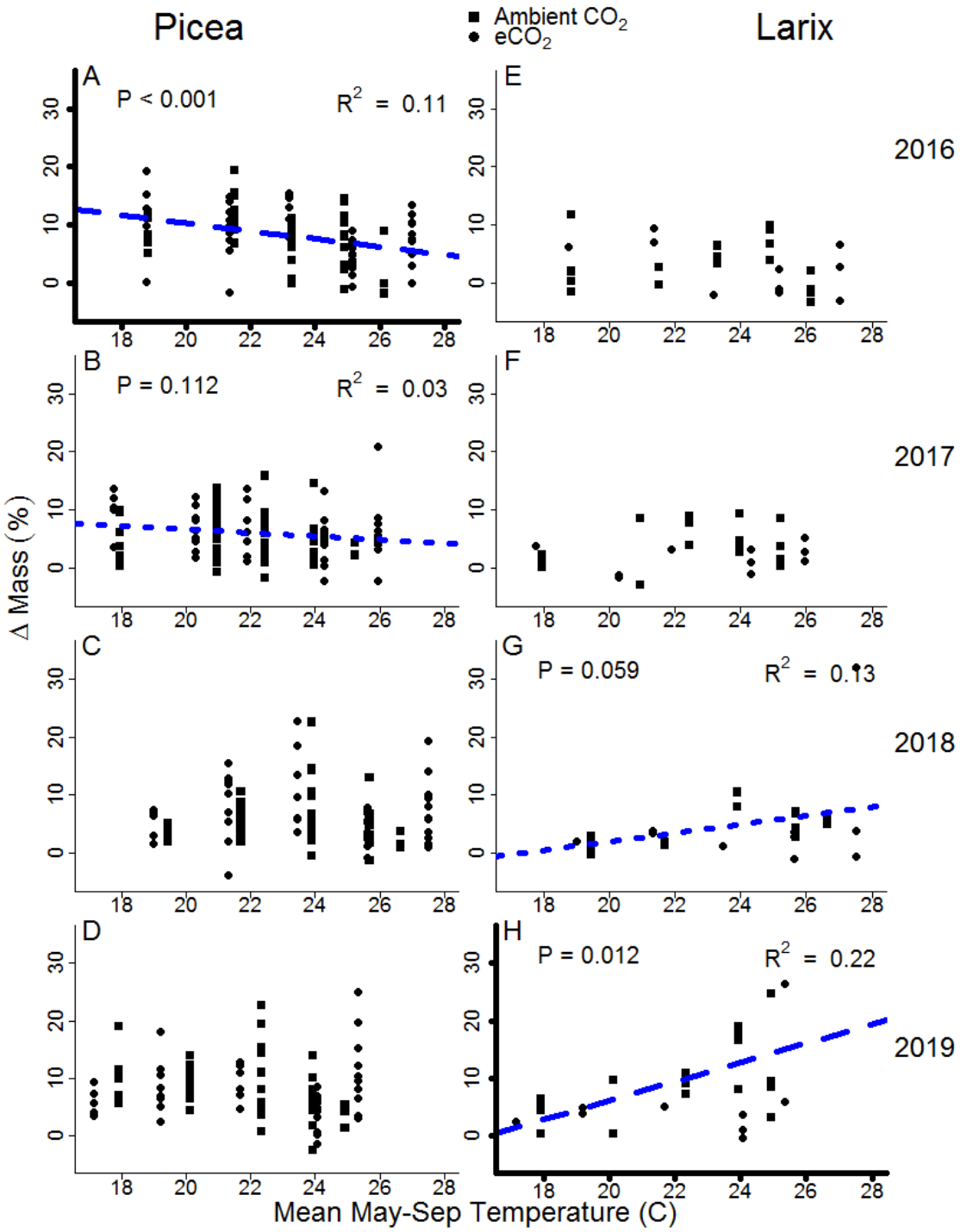

Figure 4.9. Correlations between growing season temperature and mass increment for *Picea* and *Larix* as a percentage of the tree mass at the start of each year. Significant correlations (p < 0.05) are displayed with bolded axes and dashed blue regression lines, correlations with p values between 0.05 and 0.15 have dotted blue lines showing the regression line.

References

ACIA. 2005. Forests, Land Management and Agriculture. Arctic Climate Impact Assessment. Cambridge University Press, Cambridge, UK, pp. 781–862.

Akaike, H. 1973. Information theory as an extension of the maximum likelihood principle. *In*: B. N. Petrov & F. Csaki (Eds), Proceedings of the Second International Symposium on Information Theory, pp. 267-281.

Akaike, H. 1974. A new look at the statistical model identification. IEEE Transactions on Automatic Control 19:716-723.

Akaike, H. 1981. Likelihood of a model and information criteria. Journal of Econometrics 16:3-14.

Asshoff, R., G. Zotz, and C. Korner. 2006. Growth and phenology of mature temperate forest trees in elevated CO_2. Global Change Biology 12:848-861.

Bronson, D. R., and S. T. Gower. 2010. Ecosystem warming does not affect photosynthesis or aboveground autotrophic respiration for boreal black spruce. Tree Physiology 30:441-449.

Brooks, J. R., L. B. Flanagan, and J. R. Ehleringer. 1998. Responses of boreal conifers to climate fluctuations: indications from tree-ring widths and carbon isotope analyses. Canadian Journal of Forest Research 28:524-533.

Burnham, K. P., and D. R. Anderson. 2002. Model selection and multi-model inference: a practical information-theoretic approach. Springer, New York, New York, USA.

Cao, M., and F. I. Woodward. 1998. Net primary and ecosystem production and carbon stocks of terrestrial ecosystems and their responses to climate change. Global Change Biology 4:185-198.

CloudCompare (version 2.8) [GPL software]. 2017. Retrieved from http://www.cloudcompare.org/.

Dawes, M. A., S. Hattenschwiler, P. Bebi, F. Hagedorn, I. T. Handa, C. Korner, and C. Rixen. 2011. Species-specific tree growth responses to 9 years of CO_2 enrichment at the alpine treeline. Journal of Ecology 99:383-394.

Dusenge, M. E., E. J. Ward, J. M. Warren, J. R. Stinziano, S. D. Wullschleger, P. J. Hanson, and D. A. Way. *In Review*. Warming induces divergent leaf C and water dynamics in co-occuring boreal trees. Global Change Biology.

Fryer, J. L. 2014. Picea mariana. In: Fire Effects Information System, [Online]. U.S. Department of Agriculture, Forest Service, Rocky Mountain Research Station, Fire Sciences Laboratory. Available: https://www.fs.fed.us /database/feis/plants/tree/picmar/all.html

Girardin, M. P., O. Bouriaud, E. H. Hogg, W. Kurz, N. E. Zimmermann, J. M. Metsaranta, R. de Jong, D. C. Frank, J. Esper, U. Buntgen, X. J. Guo, and J. Bhatti. 2016. No growth stimulation of Canada's boreal forest under half-century of combined warming and CO_2 fertilization. PNAS 113: E8406-E8414.

Girardin, M. P., E. H. Hogg, P. Y. Bernier, W. A. Kurz, X. J. Guo, and G. Cyr. 2015. Negative impacts of high temperatures on growth of black spruce forests intensify with the anticipated climate warming. Global Change Biology 22:627–643.

Girardin, M. P., J. Tardif, and Y. Bergeron. 2001. Radial growth analysis of *Larix laricina* from the Lake Duparquet area, Quebec, in relation to climate and larch sawfly outbreaks. Ecoscience 8:127-138.

Gorham, E. 1990. Biotic impoverishment in northern peatlands. Woodwell, G. M., editor. The earth in transition: patterns and processes of biotic impoverishment. New York: Cambridge University Press New York. p65-98.

Gower, S. T., J. G. Vogel, J. M. Norman, C. J. Kucharik, S. J. Steele, and T. K. Stow. 1997. Carbon distribution and aboveground net primary production in aspen, jack pine, and black spruce stands in Saskatchewan and Manitoba, Canada. Journal of Geophysical Research 102:29029-29041.

Graham, J. D., N. F. Glenn, and L. P. Spaete. 2019a. SPRUCE terrestrial laser scanning of experimental plots beginning in 2015. Oak Ridge National Laboratory, TES SFA, U.S. Department of Energy, Oak Ridge, Tennessee, U.S.A. https://doi.org/10.25581/spruce.067/1515552

Graham, J. D., N. F. Glenn, and L. P. Spaete. 2019b. SPRUCE microtopography of experimental plots derived from terrestrial laser scans beginning in 2016. Oak Ridge National Laboratory, TES SFA, U.S. Department of Energy, Oak Ridge, Tennessee, U.S.A. https://doi.org/10.25581/spruce.068/1515553.

Grant, R. F., H. A. Margolis, A. G. Barr, T. A. Black, A. L. Dunn, P. Y. Bernier, and O. Bergeron. 2009. Changes in net ecosystem productivity of boreal black spruce stands in response to changes in temperature at diurnal and seasonal time scales. Tree Physiology 29:1-17.

Greaves, H. E., L. A. Vierling, J. U. H. Eitel, N. T. Boelman, T. S. Magney, C. M. Prager, and K. L. Griffin. 2015. Estimating aboveground biomass and leaf area of low-stature Arctic shrubs with terrestrial LiDAR. Remote Sensing of Environment 164:26-35.

Griffiths, N. A., P. J. Hanson, D. M. Ricciuto, C. M. Iverson, A. M. Jensen, A. Malhotra, K. J. McFarlane, R. J. Norby, K. Sargsyan, S. D. Sebestyen, X. Shi, A. P. Walker, E. J. Ward, J. M. Warren, and D. J. Weston. 2017. Temporal and spatial variation in peatland carbon cycling and implications for interpreting response of an ecosystem-scale warming experiment. Soil Science Society of America Journal 81:1668-1688.

Griffiths, N. A., and S. D. Sebestyen. 2016. Dynamic vertical profiles of peat porewater chemistry in a Northern peatland. Wetlands 36:1119–1130.

Hanson, P. J., D. Brice, C. T. Garten, L. A. Hook, J. Phillips, and D. E. Todd. 2012. SPRUCE S1 Bog Vegetation Allometric and Biomass Data: 2010-2011. Oak Ridge National Laboratory, TES SFA, U.S. Department of Energy, Oak Ridge, Tennessee, U.S.A. https://doi.org/10.3334/CDIAC/spruce.004

Hanson, P. J., N. A. Griffiths, C. M. Iversen, R. J. Norby, S. D. Sebestyen, J. R. Phillips, J. P. Chanton, R. K. Kolka, A. Malhotra, K. C. Oleheiser, J. M. Warren, X. Shi, X. Yang, J. Mao, and D. M. Ricciuto. 2020. Rapid net carbon loss from a whole-ecosystem warmed peatland. AGU Advances.

Hanson, P. J., J. R. Phillips, S. D. Wullschleger, W. R. Nettles, J. M. Warren, E. J. Ward, and J. D. Graham. 2018. SPRUCE Tree Growth Assessments of Picea and Larix in S1-Bog Plots and SPRUCE Experimental Plots beginning in 2011. Oak Ridge National Laboratory, TES SFA, U.S. Department of Energy, Oak Ridge, Tennessee, U.S.A. https://doi.org/10.25581/spruce.051/1433836

Hanson, P. J., J. S. Riggs, W. R. Nettles, M. B. Krassovski, L. A. Hook. 2016. SPRUCE Whole Ecosystems Warming (WEW) Environmental Data Beginning August 2015. Carbon Dioxide Information Analysis Center, Oak Ridge National Laboratory, U.S. Department of Energy, Oak Ridge, Tennessee, U.S.A. http://dx.doi.org/10.3334/CDIAC/spruce.032

Hanson, P. J., J. S. Riggs, W. R. Nettles, J. R. Phillips, M. B. Krassovski, L. A. Hook, L. Gu, A. D. Richardson, D. M. Aubrecht, D. M. Ricciuto, J. M. Warren, and C. Barbier. 2017. Attaining whole-ecosystem warming using air and deep soil heating methods with an elevated CO_2 atmosphere. Biogeosciences 14:861–883, doi: 10.5194/bg-14-861-2017

Hendrey, G. R., and B. A. Kimball. 1994. The FACE program. Agricultural and Forest Meteorology 70:3-14.

Hoosbeek, M. R., N. van Breemen, F. Berendse, P. Grosvernier, H. Vasander, and B. Wallen. 2001. Limited effect of increased atmospheric CO_2 concentration on ombrotrophic bog vegetation. New Phytologist 150:459-463.

Jensen, A. M, J. M. Warren, A. W. King, D. M. Ricciuto, P. J. Hanson, and S. D. Wullschleger. 2019. Simulated projections of boreal forest peatland ecosystem productivity are sensitive to observed seasonality in leaf physiology. Tree Physiology 39:556-572.

Jiang, M., et al. 2020. The fate of carbon in a mature forest under carbon dioxide enrichment. Nature 480:227-231.

Johnston, W. F. 1990. *Larixlaricina* (Du Roi) K. Koch. In *Silvics of North America. Vol. 1. Conifers, Agricultural Handbook 654* (eds Burns RM, Honkala BH), pp. 141-151. USDA Forest Service.

Juday, G. P. and V. A. Barber. 2005. Alaska Tree Ring Data: Long-Term Ecological Research. Bonanza Creek LTER Database, Fairbanks, Alaska. BNZD: 214. http://www.lter.uaf.edu/

Kane, E. S., and J. G. Vogel. 2009. Patterns of total ecosystem carbon storage with changes in soil temperature in boreal black spruce forests. Ecosystems 12:322-335.

Korner, C., R. Asshoff, O. Bignucolo, S. Hattenschwiler, S. G. Keel, S. Pelaez-Riedl, S. Pepin, R. T. W. Siegwolf, G. Zotz. 2005. Carbon flux and growth in mature deciduous forest trees exposed to elevated CO_2. Science 309:1360-1362.

Li, A., N. F. Glenn, P. J. Olsoy, J. J. Mitchell, and R. Shrestha. 2015. Aboveground biomass estimates of sagebrush using terrestrial and airborne LiDAR data in a dryland ecosystem. Agricultural and Forest Meteorology 213:138-147.

Little, E. L. Jr. 1971. Atlas of United States trees. Volume 1. Conifers and important hardwoods. Misc. Publ. 1146. Washington, DC: U.S. Department of Agriculture, Forest Service. 320 p.

Mamet, S. D., and G. P. Kershaw. 2011. Radial-growth response of forest-tundra trees to climate in the western Hudson Bay lowlands. Arctic 64:446-458.

McFarlane K. J., P. J. Hanson, C. M. Iversen, J. R. Phillips, and D. J. Brice. 2018. Local spatial heterogeneity of Holocene carbon accumulation throughout the peat profile of an ombrotrophic Northern Minnesota bog. Radiocarbon 60:941–962.

Morris, P. J., G. T. Swindles, P. J. Valdes, R. F. Ivanovic, L. J. Gregoire, M. W. Smith, L. Tarasov, A. M. Haywood, and K. L. Bacon. 2018. Global peatland initiation driven by regionally asynchronous warming. PNAS 115:4851-4856.

Nishimura, P. H., and C. P. Laroque. 2011. Observed continentality in radial growth-climate relationships in a twelve site network in western Labrador, Canada. Dendrochronologia 29:17-23.

Norby, R. J., E. H. DeLucia, B. Gielen, C. Calfapietra, C. P. Giardina, J. S. King, J. Ledford, H. R. McCarthy, D. J. P Moore, R. Ceulemans, P. D. Angelis, A. C. Finzi, D. F. Karnosky, M. E. Kubiske, M. Lukac, K. S. Pregitzer, G. E. Scarascia-

Mugnozza, W. H. Schlesinger, and R. Oren. 2005. Forest response to elevated CO_2 is conserved across a broad range of productivity. PNAS 102:18052-18056.

Northeast Climate Impacts Assessment. 2006. Climate Change in the US Northeast. UCS Publications, Cambridge, MA.

Olsoy, P. J., N. F. Glenn, and P. E. Clark. 2014a. Estimating sagebrush biomass using terrestrial laser scanning. Rangeland Ecology and Management 67:224-228.

Olsoy, P. J., N. F. Glenn, P. E. Clark, and D. R. Derryberry. 2014b. Aboveground total and green biomass of dryland shrub derived from terrestrial laser scanning. ISPRS Journal of Photogrammetry and Remote Sensing 88:166-173.

Parsekian, A. D., L. Slater, D. Ntarlagiannis, J. Nolan, S. D. Sebesteyen, R. K. Kolka, and P. J. Hanson. Uncertainty in peat volume and soil carbon estimated using ground-penetrating radar and probing. Soil Science Society of America Journal 76:1911-1918.

R Core Team. 2017. R: a language and environment for statistical computing. R Foundation for Statistical Computing, Vienna, Austria. https://www.R-project.org/.

Sakamoto, Y., M. Ishiguro, and G. Kitagawa. 1986. Akaike information criterion statistics. D. Reidel Publishing, Hingham, Massachusetts, USA.

Scharlemann, P. W., E. V. J. Tanner, R. Hiederer, and V. Kapos. 2014. Global soil carbon: understanding and managing the largest terrestrial carbon pool. Carbon Management 5:81-91. https://doi.org/10.4155/cmt.13.77

Sebestyen, S. D., C. Dorrance, D. M. Olson, E. S. Verry, R. K. Kolka, A. E. Elling, and R. Kyllander. 2011. Longterm monitoring sites and trends at the Marcell Experimental Forest. In: Kolka, R. K., S. D. Sebestyen, E. S. Verry, K. N. Brooks, Eds. Peatland biogeochemistry and watershed hydrology at the Marcell experimental forest. Boca Raton (FL): CRC Press. p 15-72.

Slater, L., P. J. Hanson, and L. A. Hook. 2012. SPRUCE S1 Bog Peat Depth Determined by Push Probe and GPR: 2009–2010. Oak Ridge National Laboratory, TES SFA,

U.S. Department of Energy, Oak Ridge, Tennessee, U.S.A. https://doi.org/10.3334/CDIAC/spruce.002.

Tfaily, M. M., W. T. Cooper, J. E .Kostka, P. R. Chanton, C. W. Schadt, P. J. Hanson, C. M. Iverson and J. P. Chanton. 2014. Organic matter transformation in the peat column at Marcell Experimental Forest: humification and vertical stratification. Journal of Geophysical Research: Biogeosciences, 119: 661-675.

Tjoelker, M. G., J. Oleksyn, and P. Reich. 1999. Acclimation of respiration to temperature and CO_2 in seedlings of boreal tree species in relation to plant size and relative growth rate. Global Change Biology 49:679-691.

Viereck, L. A. 1983. The effects of fire in black spruce ecosystems of Alaska and northern Canada. In: Wein, Ross W.; MacLean, David A., eds. The role of fire in northern circumpolar ecosystems. New York: John Wiley and Sons: 201-220.

Viereck, L. A., and W. F. Johnston. 1990. *Picea mariana* (Mill.) B.S.P. In: *Silvics of North America. Vol. 1. Conifers, Agricultural Handbook 654* (eds Burns RM, Honkala BH), pp. 227–237. USDA Forest Service.

Walker, X., and J. F. Johnstone. 2014. Widespread negative correlations between black spruce growth and temperatures across topographic moisture gradients in the boreal forest. Environmental Research Letters 9:064016

Way, D. A., and R. F. Sage. 2008a. Elevated growth temperatures reduce the carbon gain of black spruce [*Picea mariana* (Mill.) B.S.P.]. Global Change Biology 14:624-636.

Way, D. A., and R. F. Sage. 2008b. Thermal acclimation of photosynthesis in black spruce [*Picea Mariana* (Mill.) B.S.P.]. Plant, Cell and Environment. 31:1250-1262.

Wilmking, M., and I. Myers-Smith. 2008. Changing climate sensitivity of black spruce (*Picea mariana* Mill.) in a peatland-forest landscape in Interior Alaska. Dendrochronologia 25:167-175.

Yu, Z. 2011. Holocene carbon flux histories of the world's peatlands: global carbon-cycle implications. The Holocene 21:761-774.

Yu, Z. 2012. Northern peatland carbon stocks and dynamics: a review. Biogeosciences 9:4071-4085.

Yu, Z., D. W. Beilman, S. Frolking, G. M. MacDonald, N. T. Roulet, P. Camill, and D. J. Charman DJ. 2011. Peatlands and their role in the global carbon cycle. EOS 92:97-108

CHAPTER FIVE: CONCLUSIONS

This dissertation explored how TLS data can be used to help improve simulations and understanding of the C cycle in peatlands. This was achieved by using TLS data to improve how peatland microtopography is measured and represented in a land surface model and measuring tree growth responses to simulated environmental change. In chapter two, I filled a gap in the scientific literature by providing standardized methods for quantifying microtopography that were used in the modeling work presented in chapter three. In addition the standardized methods I present will aid future studies wishing to take measurements along elevation or depth to water table gradients (e.g., Bubier et al., 1993; Tuitilla et al., 2004). Such studies can use the elevation distributions reported in chapter two to scale these measurements to larger extents. Alternatively, said studies could derive elevation distributions at their study site using the methodology I developed using TLS point clouds, or apply the workflow to point clouds generated from unmanned aircraft systems (UAS) lidar or structure from motion (SfM) (e.g. Lucieer et al., 2014; Lovitt et al., 2018). Further, studies that wish to stratify microtopography and sample microforms (e.g., Bubier et al., 1993; Norby et al., 2019) can use, and modify, our Functional_Classification or Scaling_Classification to choose sampling locations. This would provide consistency between sites and studies and improve inter-study comparisons by explicitly defining what constitutes hummock or hollow sampling

locations. Whether investigators treat microtopography as a continuous variable (elevation) or generalize to stratified classes (microforms), quantifying the microtopography at their site will facilitate selecting sampling sites based on quantitative data, rather than the heuristic selection of sites by the investigator. This chapter has been published in *Ecosystems* (Graham et al., 2020). Additionally, data from this chapter was used in Jan et al. (2018) and available through the public dataset Graham et al. (2019b).

The notion that peatland studies can be improved using the methodologies developed in chapter two is instantiated in chapter three. The third chapter of this dissertation used the ELM_Classification developed in chapter two to calculate ELM_SPRUCE microtopographical parameter values from empirical data, values which had previously been set heuristically. This analysis revealed that two of the three heuristically determined parameter values were larger and well outside the range of values calculated from empirical data. This demonstrates the importance of high-resolution microtopographical data that has only recently become available, and highlights the potential inaccuracies that can occur in the absence of such data. Our investigation quantified the influence of microtopographical parameters on the C cycle in ELM_SPRUCE, and found that uncertainty in microtopographical parameters resulted in relatively large uncertainty in NEE (range = 35% of the mean). Constraining microtopographical parameters and using representative values from empirical data will reduce uncertainty in simulated NEE and yield insight into model structural fidelity. Furthermore, as peatland systems shift from C sinks to C sources with ecosystem warming (Hanson et al., 2020), reducing uncertainty in simulated NEE and component

fluxes will help elucidate what degree of warming will tip these systems from sink to source. This chapter is under peer review for publication.

The fourth chapter quantified how two tree species (*Picea mariana* & *Larix laricina*) commonly found in peatlands and widely distributed across the North American boreal zone responded to simulated environmental change. This was achieved by measuring tree growth through the first four years of the SPRUCE experiment with a combination of traditional and TLS derived growth metrics. I found that *P. mariana* and *L. laricina* had divergent and dynamic responses to elevated temperatures, in which *P. mariana* had a negative growth response in the initial year which deteriorated in subsequent years. Conversely, *L. laricina* had no growth response to temperature in the first two years of the study, but in the final year of this study, *L. laricina* exhibited a significant positive correlation with temperature, which was the strongest growth response I observed. I found minimal effect of eCO_2 on tree growth, which is consistent with previous studies measuring the growth response of peatland vegetation to eCO_2 (Hoosbeek et al., 2001). While eCO_2 was determined to influence the height of *P. mariana*, this did not translate to an effect on tree mass. Conclusions drawn from this study can be used to make inferences into how *P. mariana* and *L. laricina* will respond to environmental change across their range and the effect this will have on the C budget of northern peatlands and boreal forests. Further, these results can be compared to modeling efforts that evaluate how *P. mariana* and *L. laricina* will respond to environmental change (e.g., Jensen et al., 2019) to investigate discrepancies between simulated and observed growth responses, and improve future simulations. This study is under peer-review for publication, and data from this chapter was used in Malhotra et al. (2020). The

TLS point clouds used in this study can be found in the public dataset (Graham et al., 2019a).

Overall, this dissertation advances peatland research and directly supports the efforts of the robust warming and eCO_2 experiment SPRUCE, and developed novel approaches for processing TLS point clouds to characterize microtopography. Through this dissertation, I improved how a key component of peatland ecosystems that drives multiple biogeochemical processes is measured and represented in models. Further, I add to the body of literature which evaluates how tree growth will respond to environmental change with empirical results from in-situ manipulations of temperature and eCO_2. More broadly, data and conclusions from this dissertation help improve peatland studies evaluating biogeochemical cycles and their response to environmental change.

Below is a list of publications and dataset that were either directly or indirectly a result of material in this dissertation:

Publications:

Jan, A., E. T. Coon, **J. D. Graham**, and S. L. Painter. 2018. A subgrid approach for modeling microtopography effects on overland flow. Water Resources Research 54:6153-6167.

Graham, J. D., Glenn, N. F., Spaete, L. P., & Hanson, P. J. (2020). Characterizing Peatland Microtopography Using Gradient and Microform-Based Approaches. Ecosystems, 1-17.

Kaushik, A., **J. D. Graham**, K. Dorheim, R. Kramer, J. Wang, and B. Byrne. 2020. The future of the carbon cycle in a changing climate. Eos 101.

Malhotra, A., D. Brice, J. Childs, **J. D. Graham**, E. A. Hobbie, H. Vander Stel, S. C. Feron, P. J. Hanson, and C. M. Iversen. 2020. Peatland warming strongly increases fine-root growth. PNAS *In Press.*

Datasets:

Graham, J. D., N. F. Glenn, L. P. Spaete. 2019a. SPRUCE terrestrial laser scanning of experimental plots beginning in 2015. Oak Ridge National Laboratory, TES SFA, U.S.

Department of Energy, Oak Ridge, Tennessee, U.S.A. https://doi.org/10.25581/spruce.067/1515552

Graham, J. D., N. F. Glenn, L. P. Spaete. 2019b. SPRUCE microtopography of experimental plots derived from terrestrial laser scans beginning in 2016. Oak Ridge National Laboratory, TES SFA, U.S. Department of Energy, Oak Ridge, Tennessee, U.S.A. https://doi.org/10.25581/spruce.067/1515553

References

Bubier J, Cotello A, Moore TR, Roulet NT, Savage K. 1993. Microtopography and methane flux in boreal peatlands, northern Ontario Canada. Canadian Journal of Botany 71:1056-1063.

Graham, J. D., N. F. Glenn, and L. P. Spaete. 2019a. SPRUCE terrestrial laser scanning of experimental plots beginning in 2015. Oak Ridge National Laboratory, TES SFA, U.S. Department of Energy, Oak Ridge, Tennessee, U.S.A. https://doi.org/10.25581/spruce.067/1515552

Graham, J. D., N. F. Glenn, and L. P. Spaete. 2019b. SPRUCE microtopography of experimental plots derived from terrestrial laser scans beginning in 2016. Oak Ridge National Laboratory, TES SFA, U.S. Department of Energy, Oak Ridge, Tennessee, U.S.A. https://doi.org/10.25581/spruce.068/1515553.

Graham, J. D., Glenn, N. F., Spaete, L. P., & Hanson, P. J. (2020). Characterizing Peatland Microtopography Using Gradient and Microform-Based Approaches. Ecosystems, 1-17.

Hanson PJ, Griffiths NA, Iversen CM, Norby RJ, Sebestyen SD, Phillips JR, Chanton JP, Kolka RK, Malhotra A, Oleheiser KC, Warren JM, Shi X, Yang X, Mao J, Ricciuto DM (2020) Rapid net carbon loss from a whole-ecosystem warmed peatland. AGU Advances.

Hoosbeek, M. R., N. van Breemen, F. Berendse, P. Grosvernier, H. Vasander, and B. Wallen. 2001. Limited effect of increased atmospheric CO_2 concentration on ombrotrophic bog vegetation. New Phytologist 150:459-463.

Jan, A., E. T. Coon, J. D. Graham, and S. L. Painter. 2018. A subgrid approach for modeling microtopography effects on overland flow. Water Resources Research 54:6153-6167.

Jensen, A. M, J. M. Warren, A. W. King, D. M. Ricciuto, P. J. Hanson, and S. D. Wullschleger. 2019. Simulated projections of boreal forest peatland ecosystem productivity are sensitive to observed seasonality in leaf physiology. Tree Physiology 39:556-572.

Lovitt, J., M. M. Rahman, S. Saraswati, G. J. McDermid, M. Strack, and B. Xu. 2018. UAV remote sensing can reveal the effect of low-impact seismic lines on surface morphology, hydrology, and methane (CH4) release in a boreal treed bog. Biogeosciences 123:1117-1129.

Lucieer, A., D. Turner, D. H. King, S. A. Robinson. 2014. Using an unmanned aerial vehicle (UAV) to capture microtopography of Antartic moss beds. International Journal of Applied Earth Observation and Geoinformation 27:53-72

Malhotra, A., D. Brice, J. Childs, J. D. Graham, E. A. Hobbie, H. Vander Stel, S. C. Feron, P. J. Hanson, and C. M. Iversen. 2020. Peatland warming strongly increases fine-root growth. PNAS In Press.

Norby, R. J., J. Childs, P. J. Hanson, and J. M. Warren. 2019. Rapid loss of an ecosystem engineer: Sphagnum decline in an experimentally warmed bog. Ecology and Evolution 9:12571-12585.

Tuittila, E. S., H. Vasander, and J. Laine. 2004. Sensitivity of C sequestration in reintroduced Sphagnum to water-level variation in a cutaway peatland. Restoration Ecology 12:483-493.

APPENDIX A

Chapter Two Supplemental Material

DEM Accuracy Assessment: Methods

Validation Data

During the spring of 2017 ground truth elevation data were collected in each plot by placing dowels in plot prior to TLS scanning. The top ~0.025 m of dowels were wrapped in highly reflective tape, which allowed for easy extraction from the point cloud. Dowels were marked 0.5 m from the top and inserted to the mark, ensuring the top of the reflective tape was a known 0.5 m from the bog surface. Thirty ground truth points per plot were placed in a transect-like fashion along ladders inside plots that allow access to the interior of the plot without disturbing the surface. Three of the total 360 reference points could not be reliably extracted from point clouds, and thus 357 reference points were used for the accuracy assessment.

Surface Accuracy

The location of the bog surface at reference points was compared with the digital elevation model (DEM) to evaluate the accuracy of the surface reconstruction. This was achieved by extracting points from the DEM that were the closest (XY plane, typically < 0.01 m) to reference points, and calculating the vertical distance between the extracted surface points and their respective reference points. If the surface reconstruction was perfect, the distance between all reference points and their associated DEM elevation would be exactly 0.5 m. Therefore, the difference between the calculated distance and 0.5 represents the error of the DEM at reference points.

I explored potential sources of DEM error by deriving metrics from TLS point clouds, DEM, and reference point elevations and correlating them with surface reconstruction errors. If metrics derived from point clouds or DEM explain a portion of

the variation in errors, statistical models could be used to improve the accuracy of the reconstructed model because these metrics can be calculated for every cell in the DEM. Conversely, metrics derived from reference points cannot be used to improve DEM accuracy (because they can only be generated at reference locations), but can elucidate possible sources of error and what type of locations are typically associated with positive or negative errors.

The TLS point cloud metric used was voxel (volumetric pixel) volume in a 1.0 m radius from reference points. This was performed by voxelizing the SPRUCE plot point cloud using 0.01 m voxels and calculating the number of occupied voxels that were within 1.0 m (xy plane) of reference points. Voxel volume correlates well with vegetation metrics including biomass and leaf area index (Olsoy et al., 2014; Greaves et al., 2015; Olsoy et al., 2016), and was therefore chosen as a proxy for the amount of material (vegetation or instrumentation) in close proximity to reference points that could cause laser occlusion.

I used two metrics derived from the DEM; the first metric was the normalized elevation of the DEM at the reference location, and the second was the distance to the boardwalk in SPRUCE plots where TLS scans were taken. DEM elevations were normalized by subtracting the plot mean elevation because the S1 bog has a raised dome, and the average elevation is not uniform. I used DEM elevation to explore whether there was a systematic error associated with the DEM (e.g., if higher elevations had large positive errors). I used distance to SPRUCE boardwalks because our scanner does not collect data in a 30° cone below the scanner (near the boardwalk) and scanner orientation

is less optimal at locations near the boardwalk, so these locations are not as well sampled as areas near the middle of plots.

The metric derived from reference points that I used was the normalized true elevation of the bog surface. This metric is similar to the DEM elevation, and was normalized using the same method as DEM elevations. However, normalized true elevation differs in the fact that this information is only available at reference points, not at all locations of the DEM. Therefore, this metric cannot be used to improve surface reconstructions through statistical relationship, but may provide insight into systematic errors.

Results

Surface Reconstruction

DEMs had a mean absolute error (MAE) of 0.057 m, with 84% of errors having magnitudes less than 0.1 m and 2% having errors with magnitudes larger than 0.2 m (Sup. Figure 1). DEM errors ranged from -0.128 - 0.292 m with positive errors (DEM elevation higher than actual bog surface) occurring more frequently (n = 218) than negative errors (n = 139). Further, the magnitude of positive errors (mean = 0.070 m) were also higher than negative errors (mean = 0.036 m; W = 21,027, $p < 0.001$), resulting in a bias (mean error) of 0.029 m.

Errors in DEMs were not correlated with elevations from DEMs ($p = 0.81$; $R^2 < 0.001$), but were negatively correlated with reference point elevations ($p < 0.001$; $R^2 = 0.49$), which had the strongest correlation of any metric (Sup. Figure 2). Distance to the boardwalk was also negatively correlated with errors ($p < 0.001$; $R^2 = 0.08$) and explained 8% of the variation in errors.

Contrary to expectations, voxel volume was not correlated with DEM errors (p = 0.07; R^2 = 0.006). However, I still suggest vegetation cover resulting in laser occlusion was a major source of error. I chose to use a voxel volume (0.01 m voxels) in a 1.0 m radius with the idea that this voxel volume would be a proxy for the amount of laser occlusion caused by material in close proximity, however this may not effectively capture the relationship between laser occlusion and DEM errors.

Discussion

Surface Accuracy

The produced DEMs were sufficiently accurate for calculating roughness metrics, in addition to classifying peatland microforms. Errors in DEMs from this study (0.057 m MAE) were smaller than the 0.14 - 0.42 m MAE from Lovitt et al. (2017). Lovitt et al. (2017) reported that accuracy was dependent on vegetation cover and surface complexity, with vegetation cover being a main source of error. Although it was not supported by our voxel volume metric, I also believe laser occlusion caused by surrounding vegetation (and instrumentation in SPRUCE plots) was a major source of error in our TLS derived DEM.

The study site in Lovitt et al. (2017) was very similar to our site, and therefore our data provide evidence to suggest the accuracy of DEM of peatland microtopography are higher for TLS than UAS SfM. The higher accuracy of TLS comes at the cost of either limited spatial coverage or time and labor intensive field campaigns, however, UAS lidar may provide a method with accuracy similar to TLS along with the ability to cover larger spatial extents. Although, studies comparing the three methods are needed to elucidate the efficacy of UAS lidar for characterizing peatland microtopography.

Our voxel volume metric may not have represented the relationship between vegetation cover, laser occlusion, and DEM errors for several reasons. First, in areas where accuracy is affected by laser occlusion, the laser occlusion may occur further away from the location than 1.0 m. In such cases, the voxel volume in the 1.0 m radius would be reduced because the laser was occluded before reaching the target material. It is also possible that a voxel volume at a different scale (larger/smaller radii, constraining z component in which voxel volume was calculated, larger/smaller voxels, etc.) would correlate with errors, which would indicate the 1.0 m radius and 0.01 m voxels were not the appropriate scale for the relationship. However, a cursory exploration of this explanation did not support this notion.

Errors in our DEM were correlated with reference point elevations (true elevation of the bog surface) but not with the elevation of the DEM (Sup. Figure 2), which implies the presence of systematic errors in the DEM. Specifically, areas above the plot mean elevation were associated with negative errors, indicating the reconstructed elevation was lower than the true elevation. Inversely, locations below the plot mean exhibited both more frequent positive errors and positive errors with larger magnitudes than areas near or above the mean elevation, which suggests the DEM was higher in areas with low elevations. Systematic errors of this nature likely result from higher occlusion of laser pulses at the bottom of depressions.

Scaling_Classification Continued

Methods

Matrices representing elevation from the DSM were utilized to calculate slope and concavity from image convolutions with the Open Source Computer Vision Library

(OpenCV; Bradski, 2000). Areas outside the boardwalk and inside the large flux collars were imputed with the plot elevation midpoint, so there were no missing values for convolutions. The Sobel operator (Shrivakshan and Chandrasekar, 2012) was used to calculate elevation gradient (slope; Graham et al., 2019b).

The Laplacian of Gaussian (LoG) is a convolution kernel that combines a Laplacian and a Gaussian kernel into a single convolution kernel, and is an approximation of the second spatial derivative (concavity) (Gunn, 1999). The LoG approximates concavity at a scale defined by the standard deviation (σ) of the Gaussian, and thus is a tool that can be used to identify mound-like or depression-like areas at the scale I expect to observe microforms. I convolved matrices representing microtopographic elevations with a LoG kernel to produce approximations of the second order spatial derivative at each point (Graham et al., 2019). The window size of LoG kernels was four times σ. I used a σ of 0.2 m because it smoothed high frequency undulations in elevation that occur on smaller spatial scales than I expect the hummock-hollow complex to occur. This was based on field observations and visual inspection of maps after convolutions.

Weighting Function Parameterization

Sigmoidal weighting functions were used to reduce the effect of outliers and enable the manipulation of how each value is weighted relative to where it falls in the distribution of that variable, and relative to other variables. Sigmoid weighting functions use four parameters and are defined as:

$$\text{Eqn A.1 } F(x) = \frac{L}{1 + e^{-k*(x_0 - x)}} + T$$

where F(x) is the weighted value, L defines the range of possible weights and whether the relationship is inverted (i.e., whether L is positive or negative), x_0 is the x midpoint, k defines the steepness of the weighting curve, and T is the translation of F(x). These parameters allowed us to dictate how much each variable influences the microform classification by modifying the range of possible weights (L and T), and how quickly weighting approaches the horizontal asymptotes (k) as it moves further from x_0.

Parameterizations of weighting functions (Table A.1) were determined by iteratively modifying parameters based on visualizations of weighting functions superimposed on variable distributions (Figure 2.5) and inspection of the resulting values of the Hollow Index displayed in 3D (similar to Figure 2.1B&C). The elevation weighting function is parameterized in a manner that dictates whether the Hollow Index at areas will be suppressed (weight < 1.0) or amplified (weight > 1.0). The curve of the elevation weighting function (k) is parameterized based on the plot standard deviation (σ), so that values between the 5th and 95th percentiles are weighted relatively linearly, and weights assigned outside that range experience a progressively increasing diminishing return further toward extremes (Figure 2.5E).

The LoG weighting function is parameterized such that locations with a positive LoG (i.e., concave up, depressions) receive values > 1.0 and negative LoG are weighed < 1.0 (Figure 2.5F). This parameterization results in the Hollow Index at concave up locations being amplified, and concave down locations being suppressed. The slope of the weighting function (k) is dictated by the plot σ, similar to the elevation weighting function.

The fixed range for possible values of slope (i.e., 0 - 90°) precludes the ability of extreme values to dominate the Hollow Index. Therefore, a static value was used for the parameter *k* defining the slope and degree of diminishing return weights received (Sup. Table 1). The parameterization of the slope weighting function results in areas with slopes > 45° receiving a weight < 1.0, resulting in the Hollow Index being suppressed. Conversely, locations with slopes < 45° receive a weight > 1.0 and the Hollow Index is amplified (Figure 2.5G).

Using this set of parameters and a Hollow Index classification threshold of 2.2, the Scaling_Classification can be defined at any location using equations A.2-A.6:

$$\text{Eqn A.2. } C_S(x,y) = \begin{cases} Hu, if \;\; HI(x,y) \leq 2.2 \\ Ho, if \;\; HI(x,y) > 2.2 \end{cases}$$

where $C_S(x,y)$ is the Scaling_Classification at location *xy* and HI(*x*,*y*) is the Hollow Index at location *xy*, defined by:

$$\text{Eqn A.3. } HI(x,y) = W_E(x,y) * W_C(x,y) * W_S(x,y)$$

in which $W_E(x,y)$ is the elevation weighted value, $W_C(x,y)$ is the concavity weighted value, and $W_S(x,y)$ is the slope weighted value at location xy. Weighting functions are defined as:

$$\text{Eqn A.4. } W_E(x,y) = \frac{-2}{1+ e^{-\left(\frac{1}{\sigma_z}\right)*(\mu_z - z_{xy})}} + 2$$

where σ_z is the plot-specific standard deviation in elevation from DEM and μ_z is the plot-specific mean elevation,

$$\text{Eqn A.5. } W_C(x,y) = \frac{2}{1+ e^{-\left(\frac{1}{\sigma_{\nabla^2}}\right)*(0-\nabla^2 xy)}} + 0$$

where $\sigma_{\nabla 2}$ is the plot-specific standard deviation in concavity and ∇^2_{xy} is the concavity at location *xy*, and

$$\text{Eqn A.6. } W_S(x,y) = \frac{-1}{1+ e^{-0.04*(45-S_{xy})}} + 1.5$$

where S_{xy} is the slope (in degrees) at location *xy*.

Considering that the Scaling_Classification identifies locations that I have high confidence as hollows in the field, it is assumed that any area not classified as hollow is a hummock. This assumption will influence scaling results. If one were to use this classification scheme to scale field measurements, it would be wise to provide a similar estimate for areas that are highly likely to be classified as hummock. One way to achieve this would be to invert (i.e., change the sign of *L*) the elevation and LoG weighting functions in the Hollow Index and adjust weighting parameters accordingly. This would create a "Hummock Index", thresholded in the same manner as the Hollow Index. The combination of these two indices provide estimates of areas that represent each microform, and the remaining areas could be treated as uncertainty in the classification, or intermediate microforms (e.g., lawns) functioning along the hummock-hollow continuum. In this study, weighting functions for elevation and concavity were based on distributions of each variable in SPRUCE plots, future studies would need to define a spatial scale constituting a 'plot' that will define these parameters.

Table A.1. Parameter values used in sigmoid weighting functions for calculating the Hollow Index. σ = standard deviation.

Parameter	Metric		
	Elevation (m)	Concavity ($m\ m^{-2}$)	Slope (°)
L	-2	2	-1
k	1 / Plot σ	1 / Plot σ	0.04
x0	Mean	0	45
t	2	0	1.5

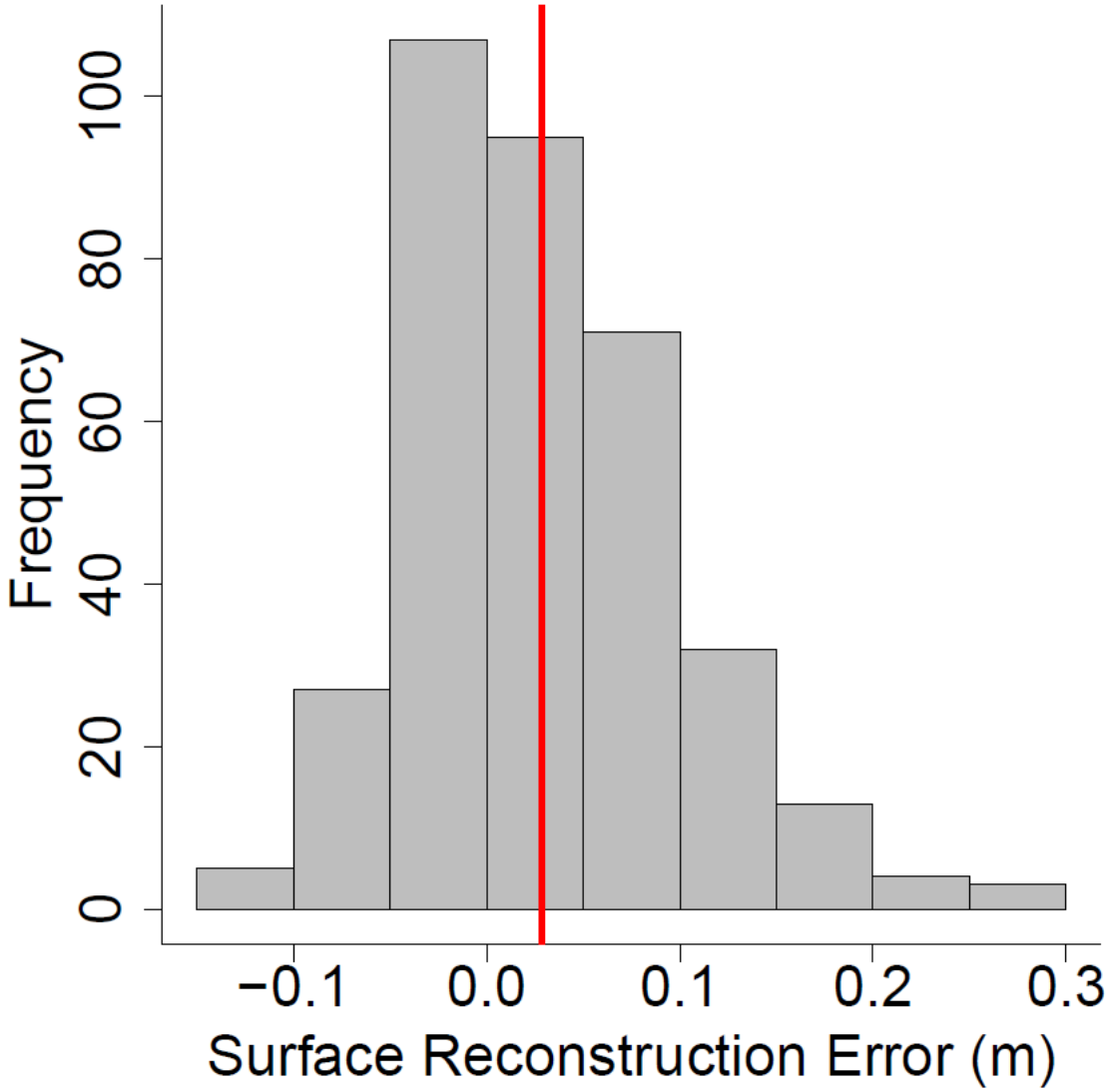

Figure A.1. Histogram of errors from 357 reference points in reconstructed surfaces with mean error displayed with a vertical red line.

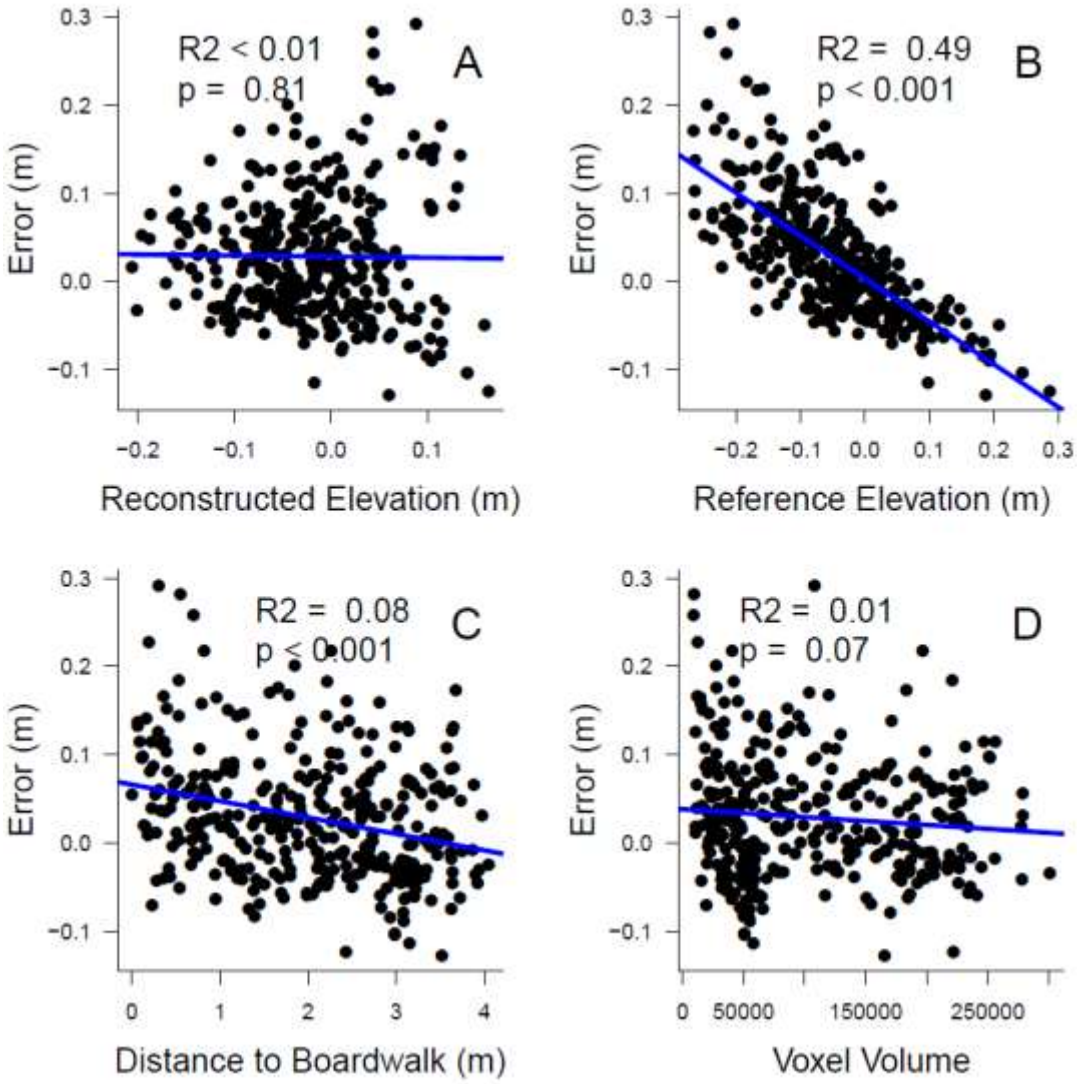

Figure A.2. Correlations of errors with elevations from the reconstructed surface (A), elevation of the bog at reference points (B), distance to the boardwalk (C), and voxel volume in a 1.0 m radius (D).

References

Bradski, G. 2000. The OpenCV Library. Dr. Dobb's Journal of Software Tools.

Graham, J. D., N. F. Glenn, and L. P. Spaete. 2019. SPRUCE microtopography of experimental plots derived from terrestrial laser scans beginning in 2016. Oak Ridge National Laboratory, TES SFA, U.S. Department of Energy, Oak Ridge, Tennessee, U.S.A. https://doi.org/10.25581/spruce.068/1515553

Greaves, H. E., L. A. Vierling, J. U. H. Eitel, N. T. Boelman, T. S. Magney, C. M. Prager, and K. L. Griffin. 2015. Estimating aboveground biomass and leaf area of low-stature Arctic shrubs with terrestrial LiDAR. Remote Sensing of Environment 164:26-35.

Gunn, S. R. 1999. On the discrete representation of the Laplacian of Gaussian. Pattern Recognition 32:1463-1472.

Lovitt, J., M. M. Rahman, and G. J. McDermid. 2017. Assessing the value of UAV photogrammetry for characterizing terrain in complex peatlands. Remote Sensing 9:715.

Olsoy, P. J., N. F. Glenn, P. E. Clark, and D. R. Derryberry. 2014. Aboveground total and green biomass of dryland shrub derived from terrestrial laser scanning. ISPRS Journal of Photogrammetry and Remote Sensing 88:166-173.

Olsoy, P. J., J. J. Mitchell, D. F. Levia, P. E. Clark, and N. F. Glenn. 2016. Estimation of big sagebrush leaf area index with terrestrial laser scanning. Ecological indicators, 61, 815-821.

Shrivakshan, G. T., and C. Chandrasekar. 2012. A comparison of various edge detection techniques for image processing. International Journal of Computer Science 9:269-276.

APPENDIX B

The scripts and software created in association with this dissertation can be found in the GitHub repository:

https://github.com/JakeGraham/GRAHAM_DISSERTATION.git